Research in Antenna Technology

John Schindler
ARCON CORP

04/06/2015
Final Report

Air Force Research Laboratory
AF Office Of Scientific Research (AFOSR)/ RTB
Arlington, Virginia 22203
Air Force Materiel Command

REPORT DOCUMENTATION PAGE		*Form Approved* *OMB No. 0704-0188*

Public reporting burden for this collection of information is estimated to average 1 hour per response, including the time for reviewing instructions, searching existing data sources, gathering and maintaining the data needed, and completing and reviewing this collection of information. Send comments regarding this burden estimate or any other aspect of this collection of information, including suggestions for reducing this burden to Department of Defense, Washington Headquarters Services, Directorate for Information Operations and Reports (0704-0188), 1215 Jefferson Davis Highway, Suite 1204, Arlington, VA 22202-4302. Respondents should be aware that notwithstanding any other provision of law, no person shall be subject to any penalty for failing to comply with a collection of information if it does not display a currently valid OMB control number. **PLEASE DO NOT RETURN YOUR FORM TO THE ABOVE ADDRESS.**

1. REPORT DATE *(DD-MM-YYYY)* 05-31-2015	2. REPORT TYPE Final Report	3. DATES COVERED *(From - To)* 04-01-2012 – 03-31-2015
4. TITLE AND SUBTITLE Research in Antenna technology, Radar Technology and Electromagnetic Scattering Phenomena		5a. CONTRACT NUMBER N/A
		5b. GRANT NUMBER FA9550-12-1-0105
		5c. PROGRAM ELEMENT NUMBER
6. AUTHOR(S) J. K. Schindler, A. D. Yaghjian, R. J. Mailloux, H. Steyskal, T. B. Hansen, R. A. Shore		5d. PROJECT NUMBER
		5e. TASK NUMBER
		5f. WORK UNIT NUMBER
7. PERFORMING ORGANIZATION NAME(S) AND ADDRESS(ES) ARCON Corporation 260 Bear Hill Rd., Ste. 200 Waltham, MA 02451-1080		8. PERFORMING ORGANIZATION REPORT AFOSR FR-01
9. SPONSORING / MONITORING AGENCY NAME(S) AND ADDRESS(ES) Air Force Office of Scientific Research 875 N. Randolph St., Room 3113 Arlington, VA 22203		10. SPONSOR/MONITOR'S ACRONYM(S) AFRL/AFOSR/RSE
		11. SPONSOR/MONITOR'S REPORT NUMBER(S)

12. DISTRIBUTION / AVAILABILITY STATEMENT
Distribution Unlimited

13. SUPPLEMENTARY NOTES

14. ABSTRACT
This document, the Final Performance Report for AFOSR Grant No. FA9550-12-1-0105, describes the research efforts of a group of six researchers in the fields of electromagnetics, radar and antenna technology. Research was conducted during this reporting period in the following technical areas: (1) compressive sensing as applied to the processing of signals from sparse receive arrays; (2) performance of the sparse fast Fourier transform for processing of coprime thinned phased arrays; (3) a general anisotropic representation for spatially and temporally dispersive media that separates electric and magnetic polarization effects; (4) plane-wave expansions with directional spectra; (5) Gaussian-beam scattering-matrix theory; (6) array realization of complex-source beams; (7) metamaterial theory, including the fundamental homogenization theory of metamaterials and scattering from multilayered spheres; (8) quantization lobe suppression for arrays of subarrays; (9) asymmetric phased array elements; and (10) current modes for efficient numerical phased array design

15. SUBJECT TERMS
compressive sensing; sparse receive arrays; fast Fourier transform ; coprime thinned phased arrays; spatially and temporally dispersive media; plane-wave expansions; Gaussian-beam scattering-matrix; complex-source beams ; metamaterial theory; quantization lobe suppression; asymmetric phased array elements; numerical phased array design

16. SECURITY CLASSIFICATION OF:			17. LIMITATION OF ABSTRACT	18. NUMBER OF PAGES	19a. NAME OF RESPONSIBLE PERSON Dr. Arje Nachman
a. REPORT UNCLASSIFIED	b. ABSTRACT UNCLASSIFIED	c. THIS PAGE UNCLASSIFIED	SAR	142	19b. TELEPHONE NUMBER *(include area code)* 703-696-8427

Standard Form 298 (Rev. 8-98)
Prescribed by ANSI Std. Z39.18

Table of Contents

Table of Contents (continued)

List of Figures

1. Introduction

ARCON Corporation is pleased to submit this Final Performance Report for Grant No. FA9550-12-1-0105 to the Air Force Office of Scientific Research (AFOSR). This report covers the performance period 1 April 2012 – 31 March 2015 and describes the research efforts of the members of the "Boston 6", a group of well-known, highly regarded researchers in the fields of electromagnetics, radar and antenna technology. The following areas of research were conducted during this reporting period : (1) compressive sensing as applied to the processing of signals from sparse receive arrays [Schindler[†]]; (2) performance of the sparse fast Fourier transform for processing of coprime thinned phased arrays [Schindler]; (3) a general anisotropic representation for spatially and temporally dispersive media that separates electric and magnetic polarization effects [Yaghjian]; (4) plane-wave expansions with directional spectra [Hansen]; (5) Gaussian-beam scattering-matrix theory [Hansen]; (6) array realization of complex-source beams [Hansen]; (7) metamaterial theory, including the fundamental homogenization theory of metamaterials and scattering from multilayered spheres [Shore]; (8) quantization lobe suppression for arrays of subarrays [Mailloux]; (9) Asymmetric Phased Array Elements [Steyskal]; and (10) Current Modes for Efficient Numerical Phased Array Design [Steyskal].

Sections 2, 4 and 5 are each followed by appendices containing technical papers some of which have been accepted for publication in technical journals. These papers, written under the sponsorship of this grant, have not been published as of the writing of this report.

During this reporting period, the Boston 6 have collectively produced over 33 publications, including papers in peer-reviewed publications, 13 invited papers/presentations and one book chapter.

[†author]

2. Performance of Airborne Random and Periodically Thinned Phased Array Antennas for Detecting and Estimating the Properties of Sparse Radiating Sources

John K. Schindler

2.1 Introduction

Research focused on the performance of airborne random and periodically thinned phased array antennas for detecting and estimating the properties of sparse radiating sources. Applications that motivated this research are:

- Accurately locating ground based sources for use with airborne, passive, bistatic radar, and

- Detecting and locating radiating sources for ESM applications to provide situational awareness and enable dynamic spectrum sharing for enhanced radar and communication systems.

Each of these applications requires measuring the properties of sparse radiating sources. Within the field of view of the phased array antenna, sparse sources consist of only a few, isolated sources that appear as uniform plane waves at the array from a few, discrete angles of arrival.

This intrinsic sparse source environment motivates the research application of recent advances in sparse time signal processing to sparse space signal processing or beamforming. The sparse time processing techniques are compressive sensing (CS) and sparse fast Fourier transform (sFFT) processing. The applications require high angular resolution beamforming to accurately locate sources in angle. High resolution beamforming naturally implies large airborne array apertures which are difficult to achieve on airborne platforms and which involve hardware with large beamforming data processing rates. The sparse signal processing approaches promise to assuage these difficulties by using only subsets of the full array element data, allowing for randomly placed subarrays which ease array placement on aircraft and thinned arrays which reduce beamforming data processing rates.

2.2 Compressive Sensing for Processing Signals from Sparse or Highly, Randomly Thinned Receive Arrays

In the first research topic we studied the usefulness of compressive sensing for processing signals from sparse or highly, randomly thinned receive arrays [1,2]. Compressive sensing consists of a theory and related algorithms for solving under determined linear equations with the assumption that solutions have only a few non-zero or dominant values and the remaining values are zero or small. Randomly thinned arrays are a natural application of CS when (a) there are only a few array observations with each expressed as a linear combination of the received plane wave signal amplitudes and (b) there are a large number of possible angles of arrival of signals but only a few signals are actually present. Our approach employed linear beamforming of the sparse array signals to create data for compressive sensing that are a linear combination of the plane wave signal amplitudes. A beamforming matrix serves to create coefficients in this linear combination that are nearly orthonormal, a requirement for successful application of CS. We evaluated CS for the problem of a five element sparse array located on a 90° sector of a

circular arc with large radius of curvature. Elements of the sparse array are themselves digitally beamformed phased arrays with main beams steered to a common direction.

We found that compressive sensing works well for large signal to noise, reliably indicating the direction of arrival of a plane wave within the beamwidth of the phased array element and potentially reliable resolution of two equal intensity plane waves within one tenth of the beamwidth of the sparse array. False plane wave indications occur with significant probability when the signal to noise is small. However, an n or more of m detection algorithm with m statistically independent noise samples reduces significantly the probability of false indication.

Application of this approach to the high resolution location of ground based sources for passive bistatic radar requires consideration of potential multipath spreading of the ground based source. Multipath spread sources can result from ground bistatic scattering from the ground based source. In further research, we considered CS processing for the case when signals have a spatial, angle of arrival distribution due to the multipath scattering of the primary source signal. This multipath case violates the CS assumption that only a few signal sources are present in the solution space and we investigated the detectability of a source signal when such multipath spread signals are present.

We found that it is unlikely that compressive sensing can distinguish primary signal radiation from its multipath components when the signal power is small in comparison with multipath power in the signal direction. A 4 out of 4 detection algorithm tends to suppress signal and multipath declarations when independent samples of the multipath are observed and the signal power is small. However, when the signal power is large compared to the multipath power in the signal direction, reliable declaration of the signal direction becomes possible, especially when 1 or more signal detections in 4 independent multipath trials are allowed. The simulation model used here is capable of determining the average properties of the angular error in signal direction when the multipath contributions are present. These angular errors contribute to target location errors in passive bistatic radar.

2.3 Performance of the Sparse Fast Fourier Transform for Processing of Coprime Thinned Phased Arrays

In a second research topic, we studied the performance of the sparse fast Fourier transform (sFFT) for processing of coprime thinned phased arrays [3]. The second application area noted above involves detecting and locating radiating sources for ESM applications and requires large, wideband phased arrays. At higher carrier frequencies, digital beamforming and frequency signal sorting processing rates with these arrays exceed current hardware capabilities. The application of multi-dimensional sFFT processing could potentially resolve these limitations by exploiting the ESM signal environment that is intrinsically sparse in space and frequency.

In our research, we analyzed the performance of coprime thinned linear arrays. A linear array is formed where the number of elements with half wavelength spacing in the array is given by the product of three relatively prime integers. Three thinned arrays are formed by thinning with each

of the prime integers. Multiple beams are formed with each of the thinned arrays by employing the discrete Fourier Transform (DFT) of the thinned array element complex voltages. Plane wave excitations of the arrays register in one or more of the DFT output samples. The thinned arrays result in ambiguities in the angles of arrival of a plane wave due to grating lobes in the array patterns. The plane wave angle of arrival can be determined uniquely by solution to Diophantine equations characteristic of thinned array pairs. Comparison of DFT outputs in two coprime arrays results in a unique angle of arrival for a single plane wave excitation, assuming that the plane wave arrives from physically realizable angles of arrival. For each pair of coprime thinned arrays, a hash table can be formed relating DFT output sample pairs to a unique angle of arrival.

We illustrated this process of plane wave signal detection and angle of arrival designation with a sample problem. Complications that occur when multiple plane waves excite the arrays were considered. One complication results from the requirement to correctly associate multiple DFT output samples between the thinned arrays. In addition, multiple plane waves can register in a single DFT output sample. These complications can be resolved by employing solution realizability conditions of the Diophantine equations. In some cases, resolution of the complications requires further observations of selected DFT output samples from a third thinned array. We illustrate these processes using the sample problem.

Two measures of performance of the coprime thinned arrays are provided. First, we considered improvements in the DFT beamforming processing rates assuming use of the conventional Fast Fourier Transform (FFT) with thinned array pairs. The thinned array processing rates required for plane wave detection and angle of arrival designation are compared to FFT beamforming with the complete, non-thinned array. Processing rates with the thinned arrays were 15% - 26% of the rates required for the fully filled array, depending on the thinned array pairs used. These efficiencies were computed assuming zero padding of the thinned array samples to employ the FFT algorithm in the beamforming. This comparison of beamforming processing rates is important for consideration of sFFT processing for practical ESM array applications.

Second, we considered the impact of receiver noise on the performance of the plane wave signal detection and angle designation. We assumed receiver noise added to each of the thinned array signal voltages and employed conventional detection processing at each of the DFT output samples. We provided the probability of plane wave detection and designation, and the probability of missed plane wave detection and designation as a function of element signal to noise ratio. We considered thinned array pairings and probability of false alarm as parameters in these results. We also give the probability of false plane wave detection and designation due to receiver noise as a function of the probability of false alarm at each DFT output sample.

2.4 References

[1] Schindler, J. K., "Compressive Sensing for Sparse Arrays," Proceedings of the 2013 IEEE International Symposium on Phased Array Systems and Technology, October 2013, pp 240 - 245.

[2] Schindler, J.K., "Compressive Sensing for Detection of Multipath Spread Sources with Sparse Arrays.", Appendix 2.5.1.

[3] Schindler, J.K., "Detection, Angle of Arrival, and Digital Beamforming Performance of Coprime Thinned Linear Arrays", Appendix 2.5.2.

2.5 Appendices

Appendix 2.5.1

Compressive Sensing for Detection of Multipath Spread Sources with Sparse Arrays

John K. Schindler

Introduction

We investigate compressive sensing (CS) as an approach to processing signals from a sparse, receive array with the objective of assessing CS capabilities for enhanced accuracy estimates of the angle of arrival of multipath spread, received plane wave signals. Compressive sensing is an approach for solving a set of under determined linear equations with the assumption that solutions have only a few non-zero or dominant values when the remaining values are zero or small. Specialized algorithms for the solution to the under determined equations are structured to emphasize the few dominant values of the solution [1]. The processing of signals from sparse, receive arrays is a natural application of CS when (a) there are only a few elements in the array providing only a few observations expressed as a linear combination of the received plane wave signal amplitudes and (b) there are a large number of possible angles of arrival of signals but only a few signals are actually present. The application to sparse arrays is important since the larger aperture of the sparse array provides superior angular resolution and better estimates of the angle of arrival of received plane wave signals. The generally poor sidelobe structure of the highly thinned arrays may be compensated by the application of compressive sensing. Here we extend a previous study [2] which examined signal detection and resolution of CS applied to a sparse array as a function of received signal to noise. In this paper, we consider the case when signals have a spatial, angle of arrival distribution due to multipath scattering of the source signal. This multipath case violates the CS assumption of only a few signal sources present in the solution space and we investigate the detectability of a source signal when such multipath spread signals are present. Multipath spread sources can result from a ground based primary communication source and bistatic scattering from terrain or building reflectors near the source. Within the radar community, target scattering is sometimes characterized by a single dominant scattering center along with a collection of small scattering surfaces on the target at differing viewing angles from the dominant scattering center.

Formulation

For purposes of this analysis, we consider a collection of N_a planar, receive apertures located randomly and tangent to a large curved surface as shown in Figure 1. While the receive apertures are randomly located, it is assumed that their positions are surveyed and are accurately known after positioning. Each of the receive apertures is a digitally beamformed array with the ability to scan the main beam of the array pattern over a large angular sector within the field of view of the array. Each of the digitally beamformed arrays is assumed to be scanned to a common direction. The system is linear so that the received signal at each aperture is a linear combination of the signal amplitudes from each of the external plane wave excitations. As indicated in Figure 1, there are N_s possible angles of arrival of plane waves. We can write the signals at the outputs of the receive apertures as

$$\mathbf{e_a} = \mathbf{\Gamma} \, \mathbf{s},$$

where the N_s x 1 vector, $\mathbf{s}$, represents the plane wave complex amplitudes from each angle of arrival, $s_n, n = 1, 2, \ldots, N_s$, the N_a x 1 vector, $\mathbf{e_a}$, represents the complex valued receive signals at the aperture

6
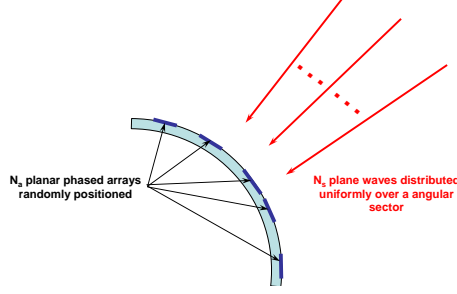
Figure 1: N_a planar phased arrays located randomly on a circular arc excited by a spectrum of N_s plane waves distributed uniformly in an angular sector.

outputs, and the N_a x N_s sensor matrix, $\mathbf{\Gamma}$, with elements $\gamma_{i,m}$, represents the response at receive aperture i due to plane wave m. Here

$$\gamma_{i,m} = p_i(\theta_m - \theta_i)e^{jkr_i(\theta_m)},$$

where p_i is the complex valued pattern of the ith aperture for a plane wave arriving at angle θ_m when the aperture is located at an angle θ_i and r_i is the distance from a common origin to the ith aperture phase center along a path from the mth plane wave excitation. In this expression, $k = 2\pi/\lambda$ where λ is the wavelength of the monochromatic plane wave excitation.

An objective of this work is to design a beamforming matrix, $\mathbf{B}$, to estimate the complex amplitudes of the incident plane waves, $\hat{\mathbf{s}}$, as a linear combination of the N_a receive signals. That is, we require the N_s x N_a matrix $\mathbf{B}$ so that

$$\hat{\mathbf{s}} = \mathbf{B}\,\mathbf{\Gamma}\,\mathbf{s} = \mathbf{D}\,\mathbf{s} = \sum_{n=1}^{N_s} \mathbf{d_n}s_n, \tag{1}$$

where the N_s x 1 vectors, $\mathbf{d_n}$, are the columns of the matrix $\mathbf{D} = \mathbf{B}\,\mathbf{\Gamma}$. Compressive sensing requires that these vectors be as nearly orthogonal as possible, given, in our case, the constraints implicit in the sensor matrix, $\mathbf{\Gamma}$. This orthogonality requirement demands that $\mathbf{D^H D} \cong \mathbf{I}$, or as nearly diagonal as possible. Here $\mathbf{D^H}$ denotes the Hermitian or conjugate transpose of $\mathbf{D}$. Abolghasemi et. al. [3] describe an iterative, numerical approach for developing the matrix $\mathbf{D}$.

The beamforming matrix can be found from the solution to

$$\tilde{\mathbf{D}} = \mathbf{B}\,\mathbf{\Gamma}, \tag{2}$$

with $\tilde{\mathbf{D}}$ denoting the matrix with near orthogonal column vectors $\tilde{\mathbf{d_n}}$. Our previous work [2] studied an approach for developing the beamforming matrix and the resultant near orthogonality of these column vectors.

Analysis

For the sparse array configuration shown in Figure 1, we assume that $N_a = 5$ sparse array elements are located at random but known positions on one quarter of a circular arc of radius $\rho = 500\lambda$, where λ is the wavelength of the received signal. Each element array is itself a fully filled phased array which is 32λ in size and located in the common plane of the arriving signals. We use the terminology "element array" to

denote that each "element" of the sparse array is itself a phased array. The element arrays occupy approximately 20% of the available surface length. Each element array is digitally beamformed with a maximum gain pattern. The main beam of each element array is pointed in the common angular direction assumed for the received plane wave if that direction is within the field of view of the element array.

For purposes of this analysis, the source exciting the sparse array consists of an angular spectrum of monochromatic, multipath plane waves and a stronger, primary monochromatic plane wave within the angular region occupied by the multipath spectrum. Physically, this source can result from a ground based primary communication source and bistatic scattering from ground based or building reflectors near the source. Within the radar community, target scattering is sometimes characterized by a single dominant scattering center along with a collection of small scattering surfaces on the target at differing viewing angles from the dominant scattering center.

We use a quantitative characterization of the distribution of power with angle of arrival of signals from a ground based communication source with ground multipath scattering adapted from Khan [6]. Bistatic scattering from locations confined to an elliptical region near the primary source contribute to an angular spectrum of multipath signals as illustrated in Figure 2. The total received power at an angle relative to the primary source is found by non-coherently integrating the power bistatic scattered along a diverging ray tube centered at the relative angle. The relative bistatic scattering power from a unit area is considered to be constant throughout the elliptical scattering region. In general, the multipath scattered power is distributed in both angle of arrival and time delay of arrival. However, since we are considering only mono-chromatic (or narrowband) signals, the distribution in time delay is unimportant and the power integration is taken over the total radial region contained in the multipath ellipse.
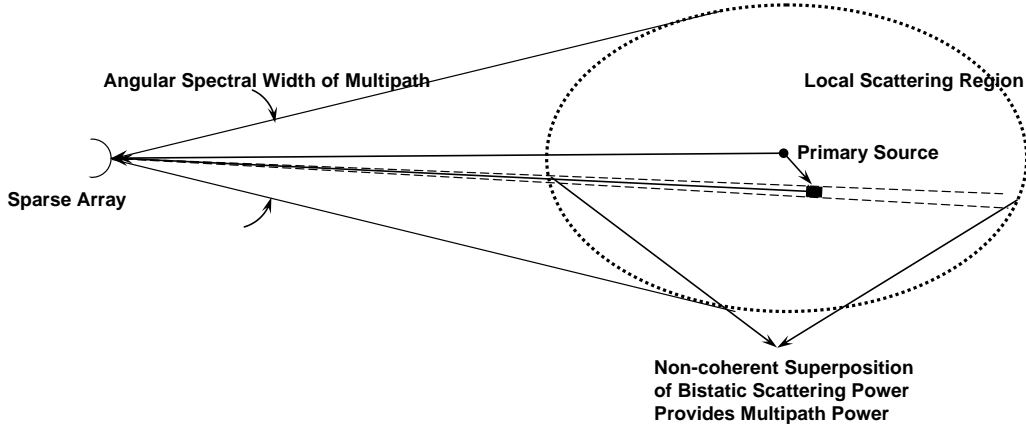
Figure 2: Bistatic scattering model to provide the angular power spectral density of multipath interference from a ground based primary source after Khan [6].

Compressive Sensing Algorithm

In order to assess the usefulness of CS for sparse array signal detection and estimation, we have implemented a CS algorithm proposed by Çetin [4] and used by Varshney [5] for synthetic aperture

8

processing. In general, compressive sensing requires that we minimize with respect to $\mathbf{s}$

$$\min_{\mathbf{s}} J(\mathbf{s}) = \left\| \mathbf{r} - \tilde{\mathbf{D}}\mathbf{s} \right\|_2^2 + \alpha \sum_{n=1}^{N_s} |s_n|^p, \tag{3}$$

when $p < 1$ and $\|x\|_2^2 \equiv \sum_{n=1}^{N_s} |x_n|^2$. The regularization term, $\alpha \sum_{n=1}^{N_s} |s_n|^p$, serves to reward large elements and penalize small elements of the solution in the minimization process. In our case, $\mathbf{r} = \mathbf{B}\,\mathbf{\Gamma_e}\,(\mathbf{s_o} + \mathbf{m}) + \mathbf{Bn}$ where $\mathbf{s_o}$ denotes the true signal vector to be detected and $\mathbf{m}$ is the N_s x 1 vector of complex, Gaussian random variants with variance given by the power determined from the multipath model described above, and thus giving the angular spread multipath signal. Complex voltage samples in each angle of arrival sample are statistically independent. Also, $\mathbf{\Gamma_e}$ represents the actual sensor matrix in contrast to the sensor matrix model used to determine the beamforming matrix, and $\mathbf{n}$ represents the N_a x 1 vector of complex, additive receiver noise at each element array output. Each entry of $\mathbf{n}$ is an independent, complex Gaussian random variant.

A contribution of Çetin is to introduce a small constant, $\varepsilon > 0$ into the regularization term in (3) to give

$$\min_{s} J_\varepsilon(\mathbf{s}) = \left\| \mathbf{r} - \tilde{\mathbf{D}}\mathbf{s} \right\|_2^2 + \alpha \sum_{n=1}^{N_s} (|s_n|^2 + \varepsilon)^{\frac{p}{2}}. \tag{4}$$

Unlike the objective function in Equation (3), this objective function is differentiable and thus supports iterative, numerical minimization with quasi-Newton approaches using complex data. The iterative solution is [4, pp 73 - 76]

$$\mathbf{s}^{n+1} = \mathbf{s}^n - \gamma \mathbf{H}(\mathbf{s}^n)^{-1} \nabla_s J_\varepsilon(\mathbf{s}^n), \tag{5}$$

where γ denotes the iterative step size between estimates of the signal vector, $\mathbf{s}^{n+1}$, at stage $n+1$ and the signal vector $\mathbf{s}^n$ at stage n. Here

$$\mathbf{H}(\mathbf{s}) = 2\tilde{\mathbf{D}}^H\tilde{\mathbf{D}} + p\alpha\mathbf{\Lambda}(\mathbf{s}),$$

and

$$\mathbf{\Lambda}(\mathbf{s}) = \text{diag}\left\{ (|s_n|^2 + \varepsilon)^{\frac{p}{2}-1} \right\},$$

giving for the gradient

$$\nabla_s J_\varepsilon(\mathbf{s}) = \mathbf{H}(\mathbf{s})\mathbf{s} - 2\tilde{\mathbf{D}}^H\mathbf{r}. \tag{6}$$

Substituting this expression for the gradient into Equation (5) gives the iterative solution

$$\mathbf{H}(\mathbf{s}^n)\mathbf{s}^{n+1} = (1 - \gamma)\mathbf{H}(\mathbf{s}^n)\mathbf{s}^n + 2\gamma\tilde{\mathbf{D}}^H\mathbf{r}, \tag{7}$$

which can be solved at each iteration for $\mathbf{s}^{n+1}$. Iterations continue until incremental changes in the solution vector are small.

Performance

The Çetin-Varshney iterative approach has been applied to the sparse array and signal with multipath model described above to determine CS performance as a function of the ratio of signal to multipath power (SMR). We investigated the probability of correct plane wave indication and the probability of false signal direction indications as a function of SMR using simulation. We provided 100 simulation trials, each with independently selected positions of the five planar arrays with the assumption that the first and last element arrays are located 90° apart. The signal vector is of dimension $N_s = 80$ with the angular separation between potential signal sources assumed to be 0.1 of the broadside, maximum gain beamwidth of the element array.

In our previous work we found that an n of m detection approach was useful to minimize false signal detections due to receiver noise. Here a signal was declared present in a given direction if the CS algorithm yielded an output which exceeded a threshold n or more times in m trials with independent observations of receiver noise on each trial. For our simulations in this work, $m = 4$ independent trials occurred in each of the 100 simulation trials. For each of the 100 array configurations, $m = 4$ independent samples of the multipath signal were generated as described above. Justification for the independent multipath samples follows from either (1) assumed motion of the sparse array with respect to the signal source or (2) assumed internal motion of elements of the multipath environment about the signal source. Receiver noise power is assumed to be negligible in comparison with the signal and multipath power at the array receiver output.

Figure 3 shows the results of this simulation. The red curves represent the probability that a desired single plane wave at an angle of 45° is declared and the blue curve represent the probability that a false signal declaration occurs due to the multipath signal. The abscissa gives the signal to multipath power ratio (SMR) where the multipath power is due to the contribution of the multipath in the same direction as the desired signal. The left column gives results for the case when detections occur in 1 or more of the 4 multipath samples and the right column gives results when detections occur on all 4 samples. We provide results for three values of the angular width of the multipath (MW) in comparison with the $3\,dB$ beamwidth of the element array. The angular width of the multipath is given by the null to null width as illustrated in Figure 2. The element array beamwidth is associated with the broadside beamwidth given by $BW_{3dB} = 0.886\lambda/D$ with $D = 32\lambda$. In Figure 3, the first row gives results for $MW/BW_{3dB} = 1$, the second row for $MW/BW_{3dB} = 2$, and the third row for $MW/BW_{3dB} = 5$. The bands denote 0.95 confidence intervals for the smoothed simulation samples. The SMR values can be corrected to give the signal power relative to the multipath power in the $3\,dB$ beamwidth and the total multipath power using the correction values in Table 1. The simulation results indicate that for small signal to multipath power
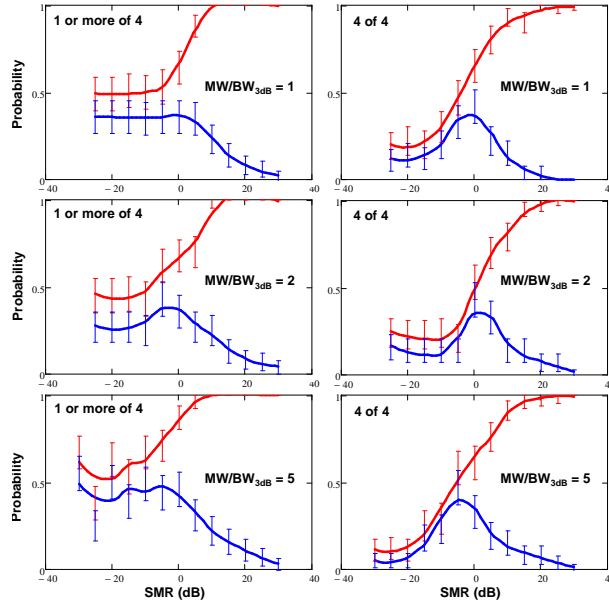
Figure 3: Smoothed simulation results for the probability of source signal declaration (red) and multipath declaration (blue) as a function of signal to multipath power (SMR). The left column gives results for 1 or more detections in 4 trials and the right column gives results for 4 detections on 4 trials. Three values of the multipath angular width (MW) in comparison to the broadside, $3\,dB$ beamwidth of the element array (MW/BW_{3dB}) are given. Bars denote 0.95 confidence intervals for the simulation results.

($SMR < 0\,dB$), there is little difference between the probability of declaring a primary source signal and its multipath component. That is, for the case of 1 or more detections in 4 trials, there is an approximate

MW/BW_{3dB}	$Power\,in\,BW_{3dB}$	$Total\,Power$
1	$8.8\,dB$	$8.8\,dB$
2	$11.4\,dB$	$11.9\,dB$
5	$14.2\,dB$	$15.9\,dB$

Table 1: SMR correction for multipath power in $3\,dB$ beamwidth and total multipath power

probability of one half of declaring either the source signal or its multipath component and there is little evidence to indicate which is actually present. For the more restrictive case of 4 of 4 detections, the probability of declaring both the signal and multipath components is much smaller, again assuming statistically independent observations of the multipath component. The qualitative similarity of the dependence on signal to multipath power between the signal and multipath declarations (blue and red curves) for $SMR < 0\,dB$ seems to be further evidence that declarations can be either signal or multipath, with nearly equal probability.

To more easily compare performance for large signal to multipath power ($SMR > 0\,dB$), we examine the probability of signal declaration versus the probability of multipath declaration shown in Figure 4. It is clear that for any probability of multipath declaration, the probability of signal declaration is greater for the 1 or more of 4 detection algorithm. Thus, while the 4 of 4 algorithm is superior for suppressing false declarations for small SMR, it degrades correct signal declaration for large SMR.
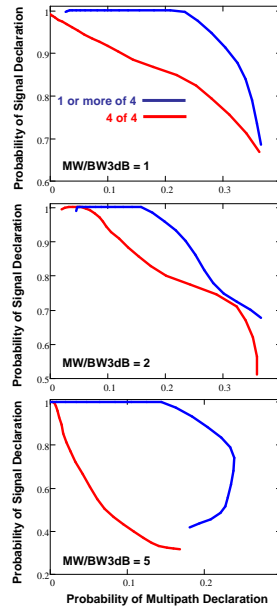
Figure 4: Probability of signal declaration vs probability of multipath declaration for $SMR > 0\,dB$ for $MW/BW_{3dB} = 1$, 2 and 5. The blue curve is for the 1 or more of 4 declaration algorithm and the red curve is for the 4 or 4 algorithm.

Conclusions

We investigated compressive sensing for processing signals from sparse or highly thinned receive arrays.

Sparse arrays are a natural application of CS when (a) there are only a few array observations expressed as a linear combination of the received plane wave signal amplitudes and (b) there are a large number of possible angles of arrival of signals but only a few signals are actually present. In this paper, we considered the case when signals have a spatial, angle of arrival distribution due to multipath scattering of a primary source signal. This multipath case violates the CS assumption of only a few signal sources present in the solution space and we investigate the detectability of a source signal when such multipath spread signals are present. Multipath spread sources can result from ground bistatic scattering from a ground based communication source. Radar target scattering is sometimes characterized by a single dominant scattering center along with a collection of small scattering surfaces on the target at differing viewing angles from the dominant scattering center.

We evaluated CS with simulation for the problem of a five element sparse array located on a 90° sector of a circular arc with large radius of curvature when compared to the wavelength of the incident radiation. Each element of the sparse array is itself a digitally beamformed phased array with its beam steered to a common direction. Signals from the beamformed arrays are linearly combined by the beamforming matrix to provide data for the compressive sensing algorithm. The algorithm used here was proposed and evaluated by Çetin [4] and Varshney [5].

As might be expected, we found that it is unlikely that compressive sensing can distinguish primary signal radiation from its multipath components when the signal power is small in comparison with multipath power in the signal direction. A 4 out of 4 detection algorithm tends to suppress signal and multipath declarations when independent samples of the multipath are observed and the signal power is small. However, when the signal power is large compared to the multipath power in the signal direction, reliable declaration of the signal direction becomes possible, especially when 1 or more signal detections in 4 independent multipath trials are allowed. The simulation model used here is capable of determining the average properties of the angular error in signal direction when the multipath contributions are present.

References

[1] A comprehensive source of references to papers on compressive sensing theory, algorithms and applications is the Rice University web site "dsp.rice.edu/cs".

[2] Schindler, J. K., "Compressive Sensing for Sparse Arrays," Proceedings of the 2013 IEEE International Symposium on Phased Array Systems and Technology, October 2013, pp 240 - 245.

[3] Abolghasemi, Vahid et. al., "On Optimization of the Measurement Matrix for Compressive Sensing," 18th European Signal Processing Conference, August, 2010, pp 427 - 431.

[4] Çetin, M., "Feature-Enhanced Synthetic Aperture Radar Imaging," PhD Dissertation, Boston University, 2001.

[5] Varshney, K. R., "Joint Anisotropy Characterization And Image Formation In Wide-Angle Synthetic Aperture Radar," Masters Thesis, Massachusetts Institute of Technology, June 2006.

[6] Khan, Norr Muhammad, "Modeling and Characterization of Multipath Fading Channels in Cellular Mobile Communication Systems," PhD Dissertation submitted to the School of Electrical Engineering and Telecommunications, The University of New South Wales, March 2006.

Appendix 2.5.2

Detection, Angle of Arrival, and Digital Beamforming Performance of Coprime Thinned Linear Arrays

John K.
Schindler

Introduction

Ultra-wideband phased array antennas capable of wide angle scan are a key element of future Defense strategies for providing the warfighter with situational awareness, capable weapons and C4ISR systems using the electromagnetic spectrum. These arrays can provide receive capabilities for enhanced electronic support measures (ESM) for situational awareness while providing a common aperture for highly capable active communications and radar systems. In addition, these arrays are a key element of future Defense strategies for dynamic spectrum sharing to provide communications and radar with enhanced performance and low probability of intercept.

However, phased arrays with ultra-wideband performance and wide angle scan present a significant technological challenge. The current art of phased array radiating elements capable of operation over a 45:1 frequency band does not exist. Extremely wideband, reconfigurable array electronics and analog beamforming approaches are only now being studied and developed. The art of high speed and accurate conversion of analog signals to digital format improves continually, offering the potential for digital beamformed arrays. However, potential digital beamforming processing rates for ultra-wideband, wide angle arrays at higher rf frequencies exceed current capabilities.

In this work we study an approach to reduce digital beamforming processing rates by the use of thinned array architectures. In ESM applications, discrete signal sources are likely to be sparsely spaced in observation angle and frequency. This is unlike active radar applications where the scattering from ground clutter may be widely spread in observation angle and other sources of interference such as jammers may appear at unknown angles. The assumption of sparse signal sources in the ESM environment raises the question of whether the use of highly thinned arrays is an appropriate choice for reducing digital beamforming rates in this application. Further, signals that are sparsely distributed in frequency may facilitate the use of reduced sampling rates or time thinned processing. This will further enhance the potential of digital processing in ESM applications.

We consider the use of thinned, linear phased arrays in a sparse signal environment using recent results for the sparse Fast Fourier Transform (sFFT) to evaluate possible reductions in digital beamforming computational rates. The sparse FFT is the result of increasingly intense research and practical implementation over the last decade focused on improving the processing efficiencies of the Fast Fourier Transform (FFT) with the assumption of a sparse signal environment in the Fourier domain [1,2]. In the discrete Fourier transform domain of a sparse signal, only a small number of the discrete frequency samples are occupied while the remaining samples are zero or relatively small due to noise. The sparse FFT uses only a data subset or thinned data stream making it ideal for application to the spatially thinned array problem.

This work builds on recent, practical applications of the sFFT [3]. These applications include reduced receiver power by faster synchronization of GPS receivers with a satellite's signal [4], implementation of the sFFT in a field programmable gate array [5], and application of sFFT to spectrum sensing and sharing radio receivers [6,7]. The majority of investigations relate to the application of Fourier analysis of sparse time signals. However, the application of the sFFT to the analysis of sparse spatial signal environments as observed with spatially thinned phased array antenna elements appears to be fertile area for practical application [8].

In this work we analyze the performance of coprime thinned arrays. A linear array is formed where the number of elements with half wavelength spacing in the array is given by the product of three relatively prime integers. Three thinned arrays are formed by thinning with each of the prime integers. Multiple beams are formed with each of the thinned arrays by employing the discrete Fourier Transform (DFT) of the thinned array element complex voltages. Plane wave excitations of the arrays register in one or more of the DFT output samples. The thinned arrays result in ambiguities in the angles of arrival of a plane wave due to grating lobes in the array patterns. The multiple, possible angles of arrival can be determined by solution to Diophantine equations characteristic of each thinned array. Comparison of the multiple, possible angles of arrival in two coprime arrays results in a unique angle of arrival for a single plane wave excitation, assuming that the plane wave arrives from physically realizable angles of arrival. For each pair of coprime thinned arrays, a hash table can be formed relating DFT output sample pairs to a unique angle of arrival.

We illustrate this process of plane wave signal detection and angle of arrival designation with a sample problem. Complications that occur when multiple plane waves excite the arrays are considered. The complications result from the requirement to correctly associate multiple DFT output samples between the thinned arrays. In addition, multiple plane waves can register in a single DFT output sample, a situation called a collision. In some cases, the complications may resolved by observing selected DFT output samples from a third thinned array. We illustrate these processes using the sample problem.

Two measures of performance of the coprime thinned arrays are provided. First, we consider improvements in the DFT beamforming processing rates assuming use of the conventional Fast Fourier Transform (FFT) with thinned array pairs. The thinned array processing rates required for plane wave detection and angle of arrival designation are compared to FFT beamforming with the complete, non-thinned array. This comparison of beamforming processing rates is important for consideration of sFFT processing for practical ESM array applications. Second, we consider the impact of receiver noise on the performance of the plane wave signal detection and angle designation. We assume receiver noise added to each of the thinned array signal voltages and employ conventional detection processing at each of the DFT output samples. We provide the probability of plane wave detection and designation, and the probability of missed plane wave detection and designation as a function of element signal to noise ratio. We consider thinned array pairings and probability of false alarm as a parameter in these results. We also give the probability of false plane wave detection and designation due to receiver noise as a function of the probability of false alarm at each DFT output sample.

Conclusions and recommendations for further study are provided.

Formulation

We consider a linear array of receive elements with inter-element spacing $d = \lambda/2$. The number of elements in the array, N_{el}, is restricted to be the product of three, coprime integers, q_i, $i = 1, 2, 3$. These coprime

14

integers have no common factors except 1. Then the number of linear array elements is given by

$$N_{el} = q_1 q_2 q_3.$$

Three periodically thinned subarrays will be considered here. The number of elements in the ith array is given by N_{el}/q_i and the thinned array is formed by processing every q_i^{th} element for $i = 1, 2, 3$. Throughout this work, we will develop as an example an array with $q_1 = 5$, $q_2 = 7$ and $q_3 = 11$ giving $N_{el} = 5 \times 7 \times 11 = 385$. Figure 1 illustrates this linear array example and the thinned arrays associated with the array. Of course, the thinned array with inter-element spacing greater than $\lambda/2$ produces a
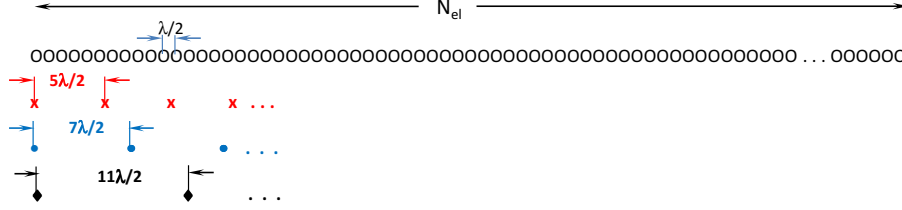
Figure 1: Linear array with three thinned arrays based on coprime thinning.

radiation pattern with grating lobes resulting in ambiguities in the direction of arrival of incident plane waves. Figure 2 shows the maximum gain response of the complete array to plane wave excitations at -45°, -5°, and 30°. In comparison, Figure 3 shows the thinned array with $q = q_3 = 11$ corresponding to analog processing of every 11th array element. The ambiguities in direction of arrival due to array grating lobes is evident. Each plane wave direction, given by fiducial markers on the abscissa, results in a multiplicity of other possible plane wave directions. The usefulness of multiple, coprime thinned arrays is
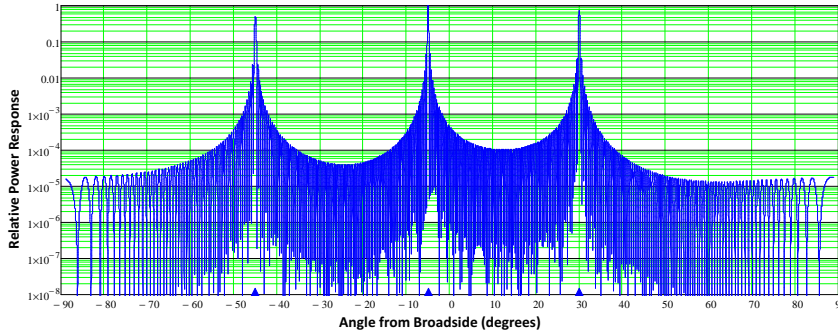
Figure 2: The maximum gain response of the complete array to plane wave excitations at -45°, -5°,and 30°.

illustrated in Figure 4. Here the response to a plane wave excitation at -45° is shown for the three coprime thinned arrays with $q = q_1 = 5$ (red), $q = q_2 = 7$ (blue) and $q = q_3 = 11$ (black). Note that the beam peaks of the ambiguous array patterns coincide only at the correct plane wave direction, -45°, as indicated by the marker on the abscissa. Thus simultaneous signal detection on all three thinned arrays must correspond to a plane wave at -45°, resolving the intrinsic ambiguity in each individual thinned array patterns.

Ambiguity resolution with multiple plane wave excitations may not be so clear, however. Figure 5 illustrates the response of thinned arrays with $q = q_2 = 7$ (blue) and $q = q_3 = 11$ (black) with three plane wave excitations from -15°, 30°, and 45°. Note that the beam peaks occur simultaneously at these angles
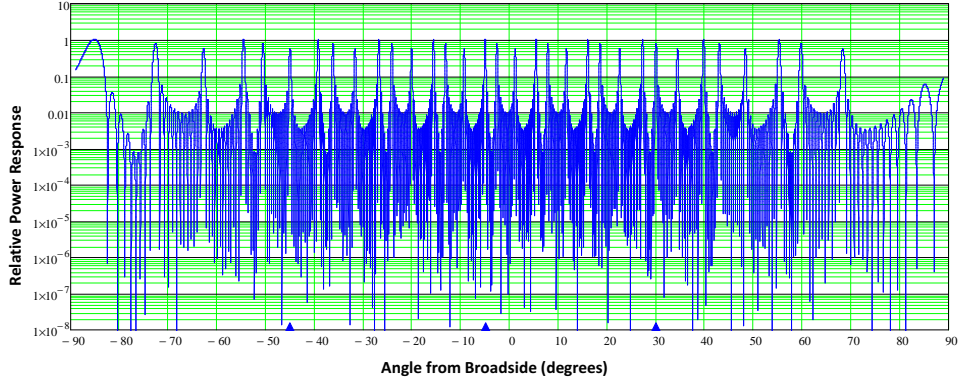
Figure 3: The maximum gain response of thinned array with $q = q_3 = 11$ corresponding to analog processing of every 11th array element; plane wave excitation directions shown by markers on abscissa.
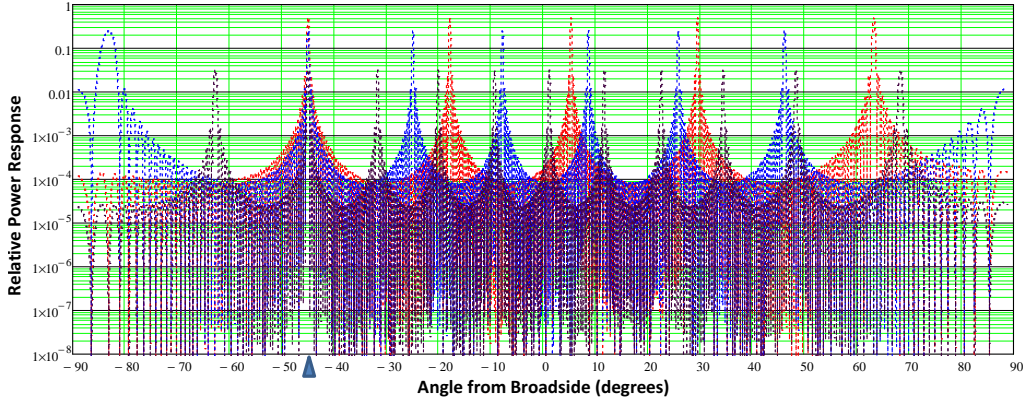
Figure 4: The maximum gain response to a plane wave excitation at -45° is shown for the three coprime thinned arrays with $q = q_1 = 5$ (red), $q = q_2 = 7$ (blue) and $q = q_3 = 11$ (black).
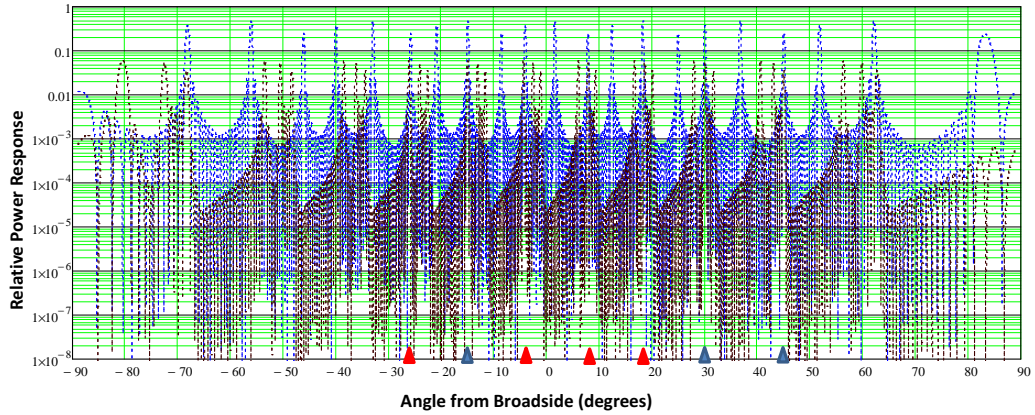
Figure 5: The maximum gain response of thinned arrays with $q = q_2 = 7$ (blue) and $q = q_3 = 11$ (black) with three plane wave excitations from -15°, 30°, and 45°.

16

of excitation, as indicated by the blue fiducial markers on the abscissa. However, near simultaneous beam peaks occur at other angles, as indicated by the red markers. Clearly falsely indicated angles of arrival may occur at other excitation angles depending on the beamwidth of the thinned arrays and the relative signal strength of the plane wave excitations.

In the following, we will examine the performance of coprime thinned arrays with digital beamforming using the discrete Fourier transform (DFT) or its computationally efficient and functionally equivalent fast Fourier transform (FFT). First we develop the approach for determining plane wave angles of arrival in terms of signal detections in one or more of the DFT samples representing the plane wave response to multiple thinned array patterns pointed in spatially orthogonal directions. Difficulties develop when multiple plane waves excite the thinned arrays, resulting in the potential that two or more waves introduce detections in the same DFT sample. An approach to resolving this difficulty is proposed and discussed. Finally, two performance measures of this algorithm for angle of arrival determination are evaluated. First the computational efficiency resulting from beamforming with multiple coprime thinned arrays is presented when compared to the beamforming processing rates associated with the fully filled array. Second, the statistical performance of signal detection and correct angle of arrival determination is studied when receiver noise is present in each of the array element signals processed by the DFT beamforming.

Angle of Arrival with DFT Processing of Thinned Arrays

Figure 6 illustrates the uniform linear array and a set of uniformly thinned arrays as defined in Figure 1 along with a uniform plane wave exciting the arrays from an angle θ measured with respect to array broadside. Then the signal voltage at each element of the fully filled array is given by

$$E_n = cos(\theta)e^{jkndsin(\theta)}, \ n = 1, 2, \ldots, N_{el},$$

where the wave number $k = 2\pi/\lambda$, λ = the wavelength of the monochromatic plane wave excitation and $d = \lambda/2$ is the inter-element spacing. The factor $cos(\theta)$ accounts for the assumed element pattern of each array element. Similarly, the signal at each element of a thinned array with thinning factor q is given by

$$E_n(q) = cos(\theta)e^{jkqndsin(\theta)}, \ n = 1, 2, \ldots, N_{el}/q.$$

Clearly, $E_n = E_n(1)$ corresponding to the fully filled array.

We assume that digital beamforming of the array element voltages consists of the discrete Fourier transform of the voltages. The DFT is chosen because of its computationally efficient implementation in terms of the fast Fourier transform. Each value of the transform represents the beam response to the one or more plane wave excitations of the array. The DFT response of a thinned array with thinning factor q to a single plane wave is given by

$$R_p(q) = \sum_{n=1}^{N_{el}/q} e^{-j\frac{2\pi np}{N_{el}/q}} cos(\theta)e^{jkqndsin(\theta)}, \ p = 1, 2, ..., N_{el}/q.$$

The response will be maximum when p satisfies

$$-\frac{2\pi p}{N_{el}/q} + kqdsin(\theta) = 2\pi m, \ m = 0, \pm 1, \pm 2, \ldots . \tag{1}$$

The multiple possible angles of arrival attributed to the exciting plane wave is then given by

$$\theta_m = asin(\frac{\lambda}{d}(\frac{m}{q} + \frac{p_{max}}{N_{el}})), \tag{2}$$

17
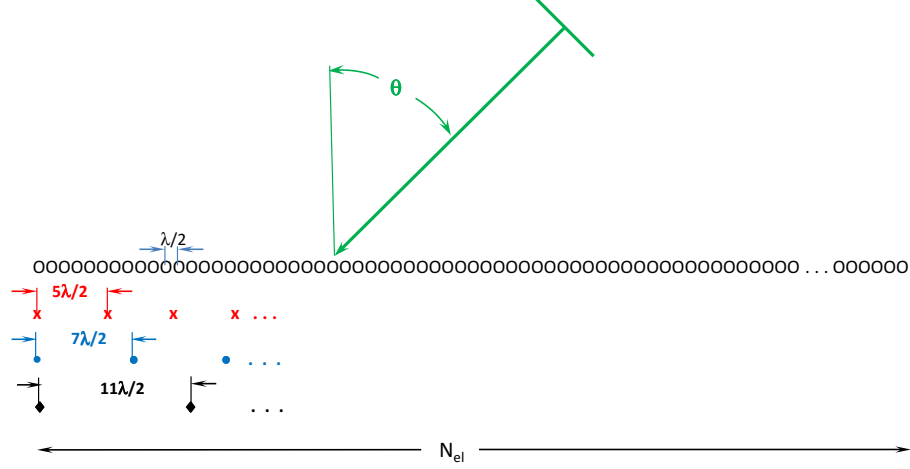
Figure 6: A uniform linear array and a set of uniformly thinned arrays as defined in Figure 1 along with a uniform plane wave exciting the arrays from an angle θ.

where p_{max} denotes the DFT sample which is maximum due to the plane wave excitation. The ambiguity in angle of arrival is given by the multiple values of m in this expression.

Resolving the angle of arrival ambiguity reduces to determining the proper value of m in Equation (2). First, we note that there are bounds on values of m. Since

$$-1 \le sin(\theta) \le 1,$$

we find that the maximum value of m is given by

$$\frac{\lambda}{d}\left(\frac{m_{max}}{q} + \frac{p_{max}}{N_{el}}\right) = 1,$$

or

$$m_{max} = q\left(\frac{d}{\lambda} - \frac{p_{max}}{N_{el}}\right). \tag{3}$$

In similar manner, the minimum value of m is given by

$$m_{min} = q\left(-\frac{d}{\lambda} - \frac{p_{max}}{N_{el}}\right). \tag{4}$$

As observed in the previous section in our discussion of Figure 4, in order to determine the value of m that determines the correct angle of arrival, we need to employ a second array with another thinning parameter, q. From Equation (1) we find

$$\frac{d}{\lambda}sin(\theta) = \frac{m_a}{q_a} + \frac{p_{max_a}}{N_{el}},$$

where the subscript a denotes parameters and measurements with respect to thinned array a. In like manner, for a second thinned array

$$\frac{d}{\lambda}sin(\theta) = \frac{m_b}{q_b} + \frac{p_{max_b}}{N_{el}},$$

so that the integer values of m_a and m_b must be solutions to the linear Diophantine equation

$$\frac{m_a}{q_a} + \frac{p_{max_a}}{N_{el}} = \frac{m_b}{q_b} + \frac{p_{max_b}}{N_{el}},$$

18

or

$$m_a q_b - m_b q_a = \frac{p_{max_b} - p_{max_a}}{q_c}, \tag{5}$$

where we have assumed that $N_{el} = q_a q_b q_c$.

Equation (5) has integer solutions of the form

$$m_a = m_{ao} modulo(q_a) = m_{ao} + n_a q_a, \ n_a = 0, \pm 1, \pm 2, \ldots, \tag{6}$$

$$m_b = m_{bo} modulo(q_b) = m_{bo} + n_b q_b \ n_b = 0, \pm 1, \pm 2, \ldots, \tag{7}$$

with m_{ao} and m_{bo} being integers. In addition, these solutions exist only when the right hand side of Equation (5) is an integer; that is

$$\frac{p_{max_b} - p_{max_a}}{q_c} = \text{integer value.} \tag{8}$$

Solutions from Equations (6) and (7) consistent with the limits given in Equations (3) and (4) under the condition that Equation (8) is valid define the angle of arrival of the plane wave that excites both thinned arrays.

To illustrate this solution technique, we consider the thinned array responses due to one plane wave excitation. Here a plane wave at $\theta = 45^o$ excites two thinned arrays with $q_1 = 5$ (red response) and $q_2 = 7$ (blue response). Figure 7 shows the magnitude of the DFT response to the two thinned arrays so that $p_{max_1} = 59$ and $p_{max_2} = 26$. With $q_3 = 11$, we find that

$$\frac{p_{max_2} - p_{max_1}}{q_3} = \frac{26 - 59}{11} = -3,$$

allowing for solutions to the Diophantine equation (Equations (5) and (8))

$$7m_1 - 5m_2 = -3.$$

It follows that

$$m_1 = \frac{-3 + 5m_2}{7} = \frac{-3 + 5m_{2o} + 7n_2}{7} = \frac{-3 + 5m_{2o}}{7} + n_2.$$

Then in order for m_1 to be integer, we require that

$$-3 + 5m_{2o} = 7r, \ r = 0, \pm 1, \pm 2, \ldots.$$

It follows that $m_{2o} = 2 modulo(7) = \ldots - 12, -5, 2, 9, \ldots$. However, from Equations (3) and (4) we have

$$m_{2_{max}} = 7(\frac{1}{2} - \frac{26}{385}) = 3.027$$

and

$$m_{2_{min}} = 7(-\frac{1}{2} - \frac{26}{385}) = -3.973.$$

With these bounds, we find that $m_2 = m_{2o} = 2$ and then using Equation (2) we find that the angle of arrival of the plane wave to be $\theta = 44.95^o$. This angle corresponds to the pointing direction of the beam peak for $p_{max_2} = 26$ where the beam response to the plane wave at 45° is the strongest. Estimates of the plane wave angle of arrival will be accurate to one-half of the 3dB beamwidth of the array of dimension $N_{el} \frac{d}{\lambda} cos(\theta)$.

19

This solution technique can be used to provide a hash table mapping all pairs of thinned array DFT values to a beam pointing direction. Figure 8 illustrates a portion of such a hash table which includes the results of the example given above. Figure 9 shows the same hash table reordered by beam pointing direction illustrating the fact that each of the $N_{el} = 385$ beam positions is related to a unique combination of p_1 and p_2 values. In this regard, note that the maximum gain beamwidth at a 45° scan is based on the projected aperture in this direction and given by

$$\frac{\lambda}{dN_{el}cos(45^o)} = 0.421^o.$$

This beamwidth is consistent with contiguous beam pointing directions at 45° from Figure 9 given by $44.95^o - 44.531^o = 0.419^o$ and $45.372^o - 44.95^o = 0.422^o$.
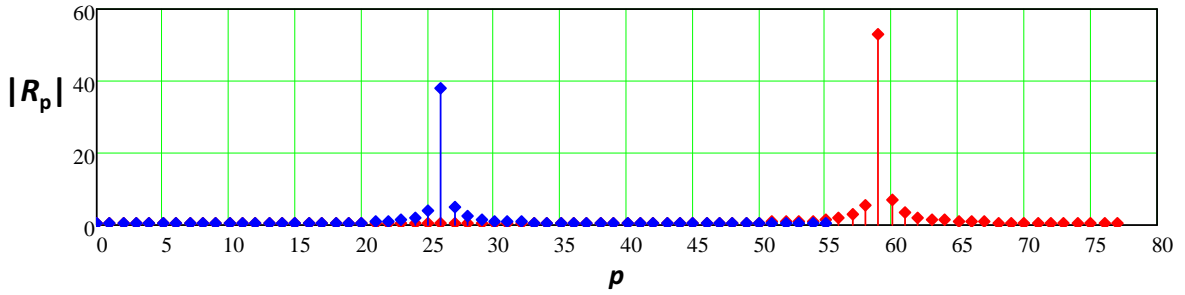
Figure 7: The magnitude of the DFT response to the two thinned arrays with $q_1 = 5$ (red) and $q_2 = 7$ (blue) and a plane wave excitation at $\theta = 45^o$.

p_1	p_2	$(p_2-p_1)/p_3$	m_{1o}	m_{1max}	m_{1min}	m_1	θ (deg)
58	3	-5	10	1.747	-3.253	0	17.536
58	14	-4	8	1.747	-3.253	-2	-29.914
58	25	-3	6	1.747	-3.253	1	44.531
58	36	-2	9	1.747	-3.253	-1	-5.664
58	47	-1	7	1.747	-3.253	-3	-63.988
59	4	-5	10	1.734	-3.266	0	17.848
59	15	-4	8	1.734	-3.266	-2	-29.571
59	26	-3	6	1.734	-3.266	1	44.95
59	37	-2	9	1.734	-3.266	-1	-5.365
59	48	-1	7	1.734	-3.266	-3	-63.317
60	5	-5	10	1.721	-3.279	0	18.161
60	16	-4	8	1.721	-3.279	-2	-29.23
60	27	-3	6	1.721	-3.279	1	45.372
60	38	-2	9	1.721	-3.279	-1	-5.066
60	49	-1	7	1.721	-3.279	-3	-62.662
61	6	-5	10	1.708	-3.292	0	...

Figure 8: Hash table for the data shown in Figure 7.

51	18	-3	6	1.838	-3.162	1	41.677
52	19	-3	6	1.825	-3.175	1	42.077
53	20	-3	6	1.812	-3.188	1	42.479
54	21	-3	6	1.799	-3.201	1	42.884
55	22	-3	6	1.786	-3.214	1	43.292
56	23	-3	6	1.773	-3.227	1	43.702
57	24	-3	6	1.76	-3.24	1	44.115
58	25	-3	6	1.747	-3.253	1	44.531
59	26	-3	6	1.734	-3.266	1	44.95
60	27	-3	6	1.721	-3.279	1	45.372
61	28	-3	6	1.708	-3.292	1	45.798
62	29	-3	6	1.695	-3.305	1	46.226
63	30	-3	6	1.682	-3.318	1	46.658
64	31	-3	6	1.669	-3.331	1	47.094
65	32	-3	6	1.656	-3.344	1	47.533
66	33	-3	6	1.643	-3.357	1	...

Figure 9: Hash table for the data shown in Figure 7 reordered by angle of arrival.

The hash tables indicate that for a single plane wave incident, a unique relationship exists between each pair of DFT samples from the thinned arrays and a beam pointing direction. However, as we shall see in the following, when multiple plane waves are incident the possibility of direction ambiguity can occur in specific cases and detections in the third thinned array are necessary to resolve these residual ambiguities.

Complications Associated with Multiple, Plane Wave Excitations

The process of determining angles of arrival of multiple plane waves is more complicated than that illustrated in the previous section. There are two complications addressed in this section. First, we must properly associate multiple DFT detections between two thinned arrays to correctly determine the angle of arrival of plane wave excitations. Second, we must address the situation when multiple plane waves excite the same DFT sample in one of the thinned arrays, a case we call DFT collisions. Further complications associated with the case when received array samples are corrupted with additive receiver noise will be addressed in the next section of this report.

Multiple Plane Wave Excitations

When more than one plane wave excites the thinned array, the DFT beamformer samples exhibit multiple detections. We are then faced with the problem of correctly associating DFT detections to create valid pairs to determine plane wave angles of arrival. This situation is illustrated in Figure 10 where plane waves at 45° and -15° excite arrays with thinning parameters $q = q_1 = 5$ (red) and $q = q_2 = 7$ (blue). We must determine which pairs of red and blue detections correctly determine the plane wave directions of arrival. This problem is resolved by remembering from Equation 8 that $\frac{p_2 - p_1}{q_3}$ must be integer to solve the Diophantine equations that determine angle of arrival. Table 1 shows a matrix of these values for the DFT samples in Figure 10. We refer this matrix as the δp matrix. It is clear that we must associate $p_2 = 26$ with $p_1 = 59$ giving an angle of arrival of 44.95^o as we saw in the last section and associate $p_2 = 5$ with $p_1 = 27$ to give an angle of arrival of -15.055^o.

21
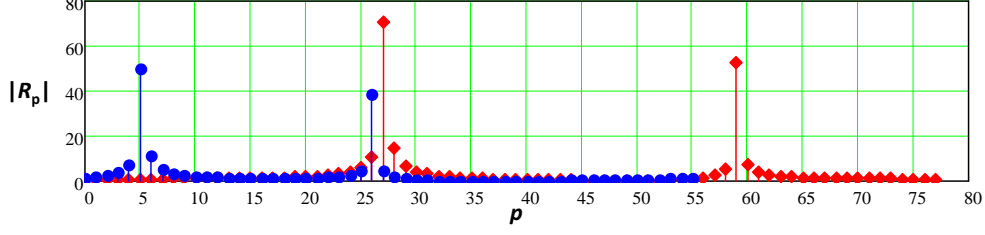
Figure 10: The magnitude of the DFT response to the two thinned arrays with thinning parameters $q = q_1 = 5$ (red) and $q = q_2 = 7$ (blue) and plane waves at 45° and -15°.

$$
\begin{array}{cc|cc}
 & & \multicolumn{2}{c}{p_1} \\
 & & 27 & 59 \\
\hline
\multirow{2}{*}{p_2} & 5 & -2 & -4.909 \\
 & 26 & -0.091 & -3 \\
\end{array}
$$

Table 1: The δp matrix for the values of the DFT samples in Figure 10.

Thus, the association problem can be solved using this δp matrix technique or equivalently, referring to the hash table to determine allowable pairs for the given values of p. However, this technique is not sufficient in all cases as we discuss in the next section.

Multiple Plane Wave Excitations with Collisions and Ambiguities

A more substantive complication occurs when two or more plane waves register in the same DFT sample, a case we describe as a collision. This can create ambiguity in the number of plane waves exciting the array. To illustrate the problem, we again consider thinned arrays with parameters $q = q_1 = 5$ (red) and $q = q_2 = 7$ (blue) illuminated with three plane wave at angles 45°, -15° and -29.5^o. The DFT beamformer response is shown in Figure 11. Here the $q = 5$ (red) array response seems to indicate the presence of two
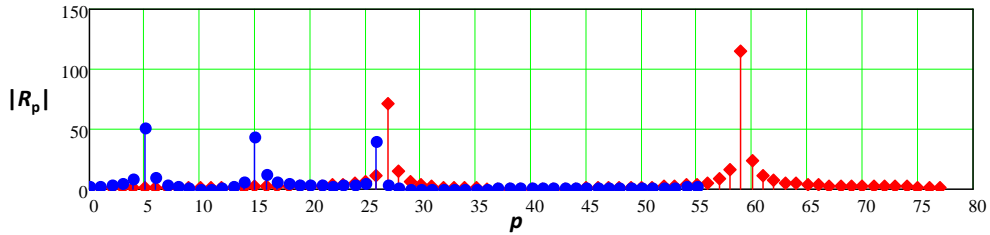
Figure 11: The magnitude of the DFT beamformer response for thinned arrays with parameters $q = q_1 = 5$ (red) and $q = q_2 = 7$ (blue) illuminated with three plane wave at angles 45°, -15° and -29.5^o.

plane waves while the $q = 7$ (blue) array response indicates three plane waves. The δp matrix of $\frac{p_2 - p_1}{q_3}$ values in Table 2 provides information on this uncertainty by associating two blue samples, $p_2 = 15$ and $p_2 = 26$, to the single red sample, $p_1 = 59$. The angles associated with the integer values of the δp matrix are indicated also and correspond to the actual angles of arrival of the three plane wave excitations.

22

	p_1	
	27	59
5	−2	−4.909
p_2 15	−1.091	−4
26	−.091	−3

	p_1	
	27	59
5	−15.055^o	–
p_2 15	–	−29.571^o
26	–	44.95^o

Table 2: The δp matrix for associating two blue samples, $p_2 = 15$ and $p_2 = 26$, to the single red sample, $p_1 = 59$ giving plane wave angles of arrival.

The DFT response data illustrated here result from noise free array voltage samples. Including receiver noise at each array samples raises the possibility of false detections in the DFT responses. Thus, we note that a noise detection in a DFT sample in one array corresponding to a plane wave detection sample in the other array creates a false plane wave indication. Confirmation of plane wave detections and angles of arrival with the third thinned array will be discussed later in this section.

The hash table expresses values of p_1 and p_2 that are compatible with solutions to the Diophantine equations for the thinned arrays. These values of p_1 and p_2 are given by

$$
\begin{aligned}
p_1 &= x + k_1 q_3 & 0 \leq p_1 \leq q_2 q_3 \\
p_2 &= x + k_2 q_3 & 0 \leq p_2 \leq q_1 q_3,
\end{aligned}
\tag{9}
$$

with integer k_1 and k_2 and $0 \leq x \leq q_3$. Either these equations or the hash tables can be used to determine possible p values and their associated angles of arrival that cause collisions.

Two additional examples of DFT sample collisions are shown in Figures 12 and 13. In Figure 12, plane waves from 69.239^o and 32.348^o excite the array. These angles are chosen to excite the DFT samples at their peak values and cause a collision in the $q = 5$ (red) DFT sample at $p_1 = 26$. Table 3 illustrates the fact that two plane waves exist for the noise free data and also gives the associated angles of arrival for these plane waves found from the hash table. From Equations (9), $p_1 = 26$ gives $x = 4$ with $k_1 = 2$. Then $p_2 = 4, 15, 26, 37,$ and 48. Angles of arrival corresponding to these five values will force collisions in the DFT response with $p_1 = 26$; Table 3 illustrates two of these values.

	p_1
	26
p_2 15	−1
48	2

	p_1
	26
p_2 15	69.239^o
48	32.348^o

Table 3: The δp matrix illustrating the fact that two plane waves exist for data collision; also illustrates the associated angles of arrival for these plane wave found from the hash table.
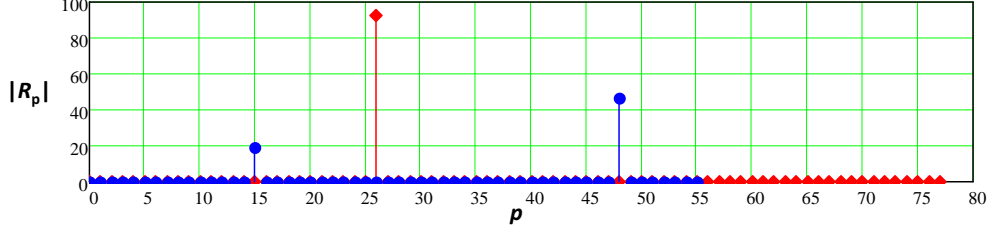
Figure 12: The magnitude of the DFT beamformer for thinned arrays with parameters $q = q_1 = 5$ (red) and $q = q_2 = 7$ (blue) with two plane waves with angles of arrival 69.239^o and 32.348^o.

In Figure 13, plane waves 69.239^o and -26.571^o excite the array causing a collision in the $q = 7$ (blue) DFT sample at $p_2 = 15$. Again the δp matrix resolves the ambiguity in the number of place wave excitations and gives the correct angles of arrival from the hash table (Table 4).

$$
\begin{array}{cc}
 & p_1 \\
 & \begin{array}{cc} 26 & 59 \end{array} \\
p_2 \;\; 15 & \begin{array}{|cc|} \hline -1 & -4 \\ \hline \end{array}
\end{array}
\qquad
\begin{array}{cc}
 & p_1 \\
 & \begin{array}{cc} 26 & 59 \end{array} \\
p_2 \;\; 15 & \begin{array}{|cc|} \hline 69.239^o & -26.571^o \\ \hline \end{array}
\end{array}
$$

Table 4: The δp matrix resolves the ambiguity in the number of place wave excitations and gives the correct angles of arrival from the hash table.

Figure 13: The magnitude of the DFT beamformer for thinned arrays illustrating a collision in the $q = 7$ (blue) DFT sample at $p_2 = 15$.

Figure 14 illustrates a further complication associated with multiple plane wave excitation of the thinned arrays. Here four plane waves excite the arrays at $60.173^o, 69.239^o$, 32.348^o, and -29.571^o. Again these angles have been chosen not only to be associated with peak values of the DFT but also to introduce collisions in both the $q = 5$ (red) samples and $q = 7$ (blue) DFT samples. Indeed, counting the number of red and blue samples in Figure 14 would seem to indicate that only three plane waves excite the array instead of the actual four plane waves. The δp matrix shown in Table 5 helps to resolve this problem as indicated by the angles of arrival associated with each integer value of $\delta p/q$. However, note that an additional false plane wave indication occurs in this situation, as noted by the red box in Table 5. Again we note the necessity of a process to confirm plane wave angles of arrival using a third thinned array.

24

	p_1					p_1		
	13	26	59			13	26	59
2	-1	-2.182	-5.182		2	60.173^o	–	–
p_2 15	0.183	-1	-4		p_2 15	–	69.239^o	-29.571^o
48	3.182	2	-1		48	–	32.348^o	-63.317^o

Table 5:
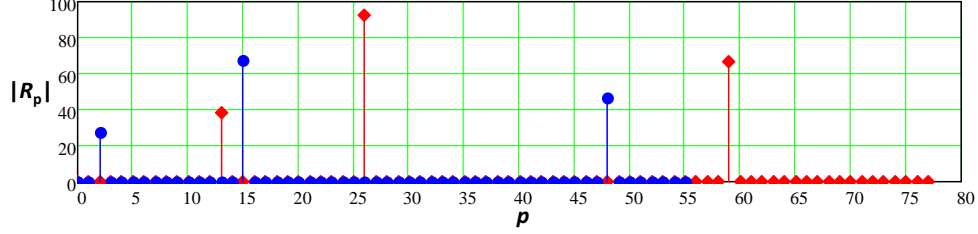
Figure 14: The magnitude of the DFT beamformer for thinned arrays illustrating a collision in the $q = 7$ (blue) DFT sample at $p_2 = 15$.

Figure 15 illustrates this confirmation process by showing the DFT samples for the third thinned array with $q = q_3 = 11$ with plane wave excitation angles of $60.173^o, 69.239^o, 32.348^o$, and -29.571^o. Note that the response corresponds to the four correct angles of arrival in Table 5. However, the incorrect angle of arrive found in Table 5, -63.317^o, from collisions in the first two thinned arrays does not produce a DFT response at $p_3 = 3$. Thus, examination of the response from the third thinned array can provide a confirmation for the angles of arrival determined from the first two thinned arrays. This confirmation process will eliminate false plane wave detections due to ambiguities due to DFT collisions and noise detections in the DFT samples.
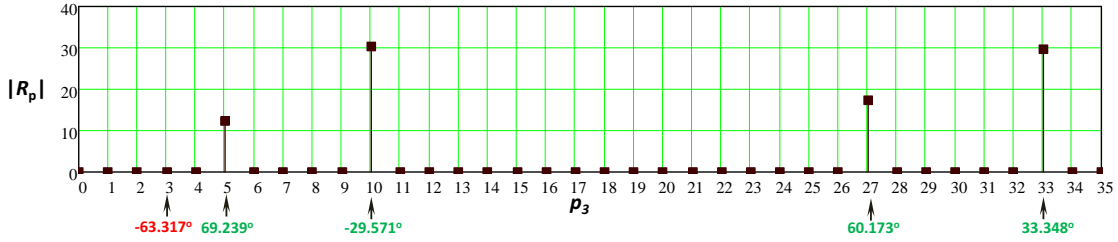
Figure 15: The magnitude of the DFT beamformer for the third thinned array with $q = q_3 = 11$ with plane wave excitation angles of $60.173^o, 69.239^o, 32.348^o$, and -29.571^o.

We note however, that it is not necessary to compute the complete DFT for the third thinned array. In fact, only the DFT samples associated with angles of arrival determined from the q_1 and q_2 need to be computed. This is an important point since our investigation is motivated by the need to reduce the digital beamforming processing rates in a sparse signal environment. Fewer computations are required for the beamforming response to a few signals than are required for the complete DFT implemented as the FFT. We consider this further in the next section.

25

Performance

We investigate the use of multiple, thinned arrays as an approach for reducing the processing rate associated with digital beamforming in a sparse signal environment. To that end, we evaluate in the following section reductions in the processing rate associated with the thinned arrays studied in the previous sections when compared to processing rates for the fully filled array of equivalent size. However, processing rates are not the only performance criterion of importance. Practical application of approaches as described here must consider the presence of receiver noise in each of the array element voltages. Receiver noise can create false signal detections which, when paired with correct signal responses or noise detections can create false plane wave indications. These false indications require further confirmation with additional processing of a third thinned array element voltages, as described in the last section. Probabilities of correct signal detections and false signal indications as a function of element signal to noise are discussed in the following.

Digital Beamforming Efficiencies with Thinned Arrays

We assume that signals from each of the thinned arrays are processed with the computational efficient Fast Fourier Transform (FFT) to create multiple, simultaneous beams from each of the arrays. The FFT is prescribed since one of our performance considerations is with beamforming processing rates associated with large arrays. One of the more efficient FFT implementations is the split-radix implementation [9] where the number of flops (floating point operations with real additions and multiplications) of standard complex data is given by

$$F(L) = 4L \, log_2(L) - 6\,L + 8,$$

where L is the number of samples employed in the FFT and is a power of 2. The number of elements in the thinned subarrays described here are not a power of 2. To resolve this discrepancy, we assume that the number of samples in each thinned subarray is a power of 2 by adding as sufficient number of zero element voltages, an approach often called zero padding. For example, the thinned array with $q = q_1 = 5$ has $q_2 q_3 = 77$ elements and the processing assumes $2^7 = 128 > 77$ element voltages, including the zero padded element voltages.

We characterize the digital beamforming efficiency of the thinned array processing as the ratio of the number of FFT processing flops required to beamform two thinned array to the number of FFT processing flops to beamform the fully filled array. That is, the efficiency of using thinned arrays with q_i and q_j is given by

$$E_{i,j} = \frac{F\left(\left.\frac{N_{el}}{q_j}\right|_2\right) + F\left(\left.\frac{N_{el}}{q_i}\right|_2\right)}{F\left(N_{el}\Big|_2\right)}.$$

Here $x\Big|_2 \equiv 2^{ceil(log_2(x))}$ where $ceil(y)$ denotes the smallest integer which is larger than y. Note that these efficiencies do not include computations necessary to (a) determine angles of arrival from precomputed hash tables and (b) confirmation of plane wave angles of arrival and elimination of false indications by digitally forming specific beam directions in the third array. These additional computations depend on the number of incident plane waves and false detections in thinned array FFT samples, both of which are random and assumed to impose a relatively small number of additional beamforming computations.

With these assumptions and caveats, the digital beamforming efficiencies of the thinned arrays discussed here are

$$\begin{aligned} E_{1,2} &= 0.259 \\ E_{1,3} &= 0.259 \\ E_{2,3} &= 0.151. \end{aligned}$$

The common values of the efficiencies $E_{1,2}$ and $E_{1,3}$ is due to the common number of FFT samples processed due to the zero padding assumption. We note that from the viewpoint of digital beamforming computational efficiency, it is preferable to use the arrays with the highest thinning factors, $q = q_2 = 7$ and $q = q_3 = 11$, as the baseline for determining plane wave indications and angles of arrival. However, this results in the greatest penalty in efficiency when confirmation of plane wave indication and angle of arrival determination is required using a third array. This is due to the fact that with the highest thinning factors, more grating lobes exist and therefore more opportunities exist for ambiguities that require third array processing for resolution.

Performance Probabilities with Receiver Noise

The presence of receiver noise at each element of the thinned array introduces the possibility of false detections at the thinned array beamformed output which in turn allows for the possibility of incorrect plane wave detections and arrival angle designations. The digital beamforming of signals from the thinned array elements assumes implicitly that an rf receiver and frequency downconverter exists at each element to prepare inphase and quadrature signals for digital conversion. The noise figure of the rf receiver sets the signal to noise of the signal processed by the digital beamformer. We assume here that this receiver noise is the predominant source of noise in the beamforming processing and signal detection.

We assume conventional signal detection at each DFT beam output. The magnitude of the output is compared to a threshold established so that the probability of the magnitude exceeding the threshold due to a noise signal alone is a fixed probability of false alarm, p_{fa}. The probability of the output exceeding the threshold when signal and noise are present, p_d, is established as a function of the signal to noise ratio at the DFT beam output, SNR. The conventional analysis of this problem considers the magnitude of the noise signal alone, r, to have the Rayleigh probability density, $p_{Rayleigh}(r)$, due to the assumed Gaussian quadrature components of the noise. That is

$$p_{Rayleigh}(r) = \frac{r}{\sigma^2} e^{-\frac{r^2}{2\sigma^2}} \quad r \geq 0.$$

Then the detection threshold, V_t, is established from the given probability of false alarm as

$$p_{fa} = \int_{V_t}^{\infty} \frac{r}{\sigma^2} e^{-\frac{r^2}{2\sigma^2}} dr = \int_{\frac{V_t^2}{2\sigma^2}}^{\infty} e^{-u} du = e^{-\frac{V_t^2}{2\sigma^2}},$$

or $\frac{V_t^2}{2\sigma^2} = -ln(p_{fa})$.

When the signal and noise are present, the magnitude of this signal, r, is Ricean distributed with probability density

$$p_{Rice}(r) = \frac{r}{\sigma^2} e^{-\frac{r^2+A^2}{2\sigma^2}} I_o(\frac{rA}{\sigma^2}) \qquad r \geq 0.$$

27

Here $I_o(x)$ denotes the modified Bessel function of the first kind of order zero. Then the probability of signal detection is given by

$$
\begin{aligned}
p_d(SNR) &= \int_{V_t}^{\infty} \frac{u}{\sigma^2} e^{-\frac{u^2+A^2}{2\sigma^2}} I_o(\frac{uA}{\sigma^2}) du \\
&= \int_{\frac{V_t^2}{2\sigma^2}}^{\infty} e^{-(v+SNR)} I_o(2\sqrt{vSNR}) dv \\
&= \int_{-ln(p_{fa})}^{\infty} e^{-(v+SNR)} I_o(2\sqrt{vSNR}) dv.
\end{aligned}
$$

In this expression, $SNR \equiv A^2/2\sigma^2$. In our work, this signal to noise is at the DFT beam output with thinning factor q_i and is given in terms of the element signal to noise, $SNR_{element}$, by

$$
SNR_i = \frac{N_{el}}{q_i} SNR_{element}.
$$

This follows from the fact that the plane wave signal adds coherently among the array elements at the DFT beam peak while the receiver noise adds non-coherently (power addition) due to the assumed statistical independence among the noise signals at the array elements. We use the actual number of array elements N_{el} instead of the number of elements in the zero padded array since the additional padded array values do not contribute to the signal and noise power at the DFT sample beam outputs.

We consider two measures of performance of the thinned array approach as function of element signal to noise radio. These are (1) the probability of correct plane wave detection and angle of arrival designation when only a single plane wave excites the arrays, (2) the probability of a missed plane wave detection when one is actually present, and (3) the probability of false plane wave detection and angle of arrival designation due to noise only. There are other possible performance measures that might be considered. Among these are (4) the probability of false signal detection and angle of arrival designation due to noise when a plane wave is present and (5) the probability of incorrect signal angle of arrival designation due to noise in the presence of a plane wave excitation. These other performance measures will not be considered here.

To determine the probability of correct plane wave detection and angle of arrival designation we recall that the plane wave DFT sample in a baseline thinned array must relate to a unique sample in the secondary, thinned array as given by the hash table for the arrays. If "a" denotes the baseline array and "b" denotes the secondary array, then the probability of correct detection and designation is given by

$$
\begin{aligned}
p_{pw}(SNR_{element}) &= p_d(SNR_a)(1-p_{fa})^{\frac{N_{el}}{q_a}-1} p_d(SNR_b)(1-p_{fa})^{q_b-1}. \\
&= p_d(\frac{N_{el}}{q_a}SNR_{element})(1-p_{fa})^{\frac{N_{el}}{q_a}-1} p_d(\frac{N_{el}}{q_b}SNR_{element})(1-p_{fa})^{q_b-1}.
\end{aligned} \tag{10}
$$

In this expression, the first two factors, $p_d(SNR_a)(1-p_{fa})^{\frac{N_{el}}{q_a}-1}$, represent the probability of detecting the plane wave on one of the N_{el}/q_a DFT samples of the baseline thinned array "a" while insuring that there are no noise false detections on the remaining $N_{el}/q_a - 1$ samples. From the hash table, there are q_b DFT samples from the secondary thinned array "b" that are acceptable. Thus, the third and fourth factors in Equation (10), $p_d(\frac{N_{el}}{q_b}SNR_{element})(1-p_{fa})^{q_b-1}$, represent the probability of detecting the plane wave on one of these DFT samples and no detections on the remaining $q_b - 1$ samples.

Figure 16 shows the probability of plane wave detection and angle of arrival designation as a function of element signal to noise with probability of false alarm detection at the DFT output sample of 10^{-4} and 10^{-6}. We show here combinations of baseline and secondary thinned arrays of $(a,b) = (1,2), (1,3)$, and $(2,3)$. Combinations with reversed roles of the thinned arrays,
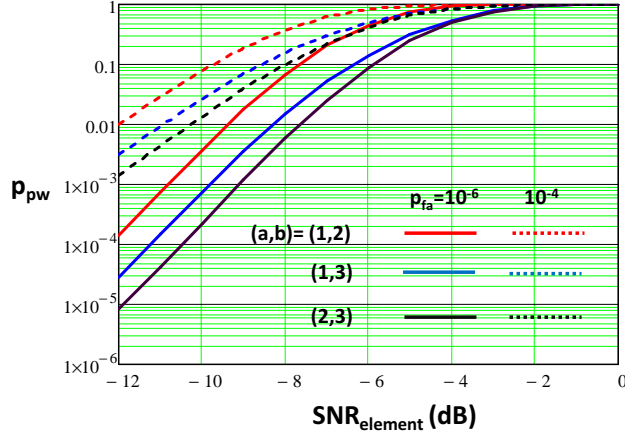
Figure 16: The probability of plane wave detection and angle of arrival designation as a function of element signal to noise with probability of false alarm detection at the DFT output sample of 10^{-4} and 10^{-6}.

$(a, b) = (2, 1), (3, 1)$, and $(3, 2)$, give approximately the same results. For a given element signal to noise, thinned array combinations with the lease thinning, $(a, b) = (1, 2)$, gives the best results. This is due to the increased array gain and signal to noise for plane wave detection even with a greater number of DFT samples where false alarms may occur.

To determine the probability of a missed plane wave detection, we again recall that the plane wave DFT sample in a baseline thinned array must relate to a unique sample in the secondary, thinned array as given by the hash table for the arrays. If "a" denotes the baseline array and "b" denotes the secondary array then the probability of a missed detection, p_{mpw}, with no false detections due to noise is given by

$$
\begin{aligned}
p_{mpw}(SNR_{element}) &= p_d(SNR_a)(1 - p_{fa})^{\frac{N_{el}}{q_a} - 1}(1 - p_d(SNR_b))(1 - p_{fa})^{q_b - 1}. \\
&\quad + (1 - p_d(SNR_a))(1 - p_{fa})^{\frac{N_{el}}{q_a} - 1}p_d(SNR_b)(1 - p_{fa})^{q_b - 1}. \\
&\quad + (1 - p_d(SNR_a))(1 - p_{fa})^{\frac{N_{el}}{q_a} - 1}(1 - p_d(SNR_b))(1 - p_{fa})^{q_b - 1}. \\
\\
&= p_d(\tfrac{N_{el}}{q_a}SNR_{element})(1 - p_{fa})^{\frac{N_{el}}{q_a} - 1}(1 - p_d(\tfrac{N_{el}}{q_b}SNR_{element}))(1 - p_{fa})^{q_b - 1} \\
&\quad + (1 - p_d(\tfrac{N_{el}}{q_a}SNR_{element}))(1 - p_{fa})^{\frac{N_{el}}{q_a} - 1}p_d(\tfrac{N_{el}}{q_b}SNR_{element})(1 - p_{fa})^{q_b - 1} \\
&\quad + (1 - p_d(\tfrac{N_{el}}{q_a}SNR_{element}))(1 - p_{fa})^{\frac{N_{el}}{q_a} - 1}(1 - p_d(\tfrac{N_{el}}{q_b}SNR_{element}))(1 - p_{fa})^{q_b - 1}. \\
\\
&= (1 - p_d(\tfrac{N_{el}}{q_a}SNR_{element}p_d(\tfrac{N_{el}}{q_b}SNR_{element})(1 - p_{fa})^{\frac{N_{el}}{q_a} + q_b - 2}
\end{aligned}
$$

In this expression, the first term represents the probability of a plane wave detection on the baseline array and no detection on the secondary array. Similarly, the second term gives the probability of a no detection on the base line array and a detection on the secondary array. Finally, the third term gives the probability on no detection on either array. In each outcome, no false indications due to noise are allowed.

Figure 17 shows the probability of a missed plane wave as a function of element signal to noise with probability of false alarm detection at the DFT output sample of 10^{-4} and 10^{-6}. Again we show here combinations of baseline and secondary thinned arrays of $(a, b) = (1, 2), (1, 3)$, and $(2, 3)$. For a given

29

element signal to noise, the thinned array combination with the lease thinning, $(a, b) = (1, 2)$, gives the best results. Again, this is due to the increased array gain and signal to noise for plane wave detection even with a greater number of DFT samples where false alarms may occur.
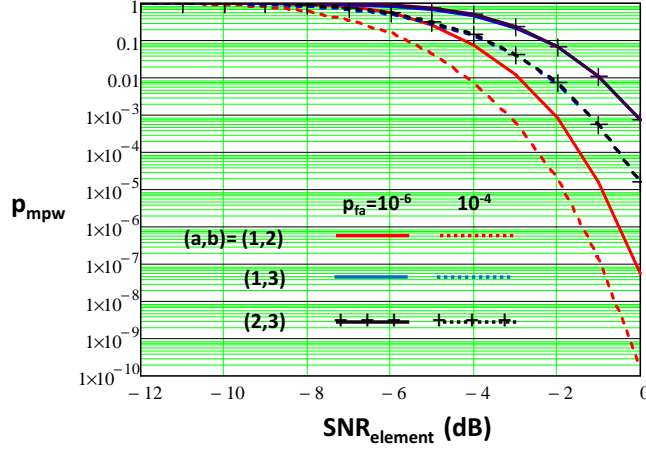
Figure 17: The probability of a missed plane wave as a function of element signal to noise with probability of false alarm detection at the DFT output sample of 10^{-4} and 10^{-6}.

Finally, we consider the probability of false plane wave indication and angle of arrival designation due only to the presence of receiver noise. At each DFT beam output, the probability of the signal exceeding the threshold is given by p_{fa}. As we have seen previously, the threshold is set by the prescribed probability of false alarm.

The binomial distribution describes the number of false alarm indications on the baseline thinned array. That is,

$$b(p, \frac{N_{el}}{q_a}, p_{fa}) = \frac{(\frac{N_{el}}{q_a})!}{p!(\frac{N_{el}}{q_a} - p)!} p_{fa}^p (1 - p_{fa})^{\frac{N_{el}}{q_a} - p},$$

denotes the probability of p statistically independent false alarms in the number of beam outputs, $\frac{N_{el}}{q_a}$, in the ath thinned array when the probability of false alarm in each beam position is p_{fa}. For each of the false alarms in the baseline array, we require that one or more false alarms occur on the q_b secondary thinned array beam positions given by the hash table. The probability of this event is

$$1 - (1 - p_{fa})^{q_b},$$

where $(1 - p_{fa})^{q_b}$ gives the probability of no false alarms among the q_b beam positions specified by the hash table for the secondary array. The equation above gives the probability of one or more false alarms among the q_b beam positions designated by the hash table for a primary array false alarm. Finally, the probability of one or more false plane wave indications and angle of arrival designations due to receiver noise is given by

$$p_{fpw} = \frac{\sum_{p=1}^{\frac{N_{el}}{q_a}} b(p, \frac{N_{el}}{q_a}, p_{fa})[1 - (1 - p_{fa})^{q_b}]^p}{\sum_{p=0}^{\frac{N_{el}}{q_a}} b(p, \frac{N_{el}}{q_a}, p_{fa})[1 - (1 - p_{fa})^{q_b}]^p}. \tag{11}$$

30
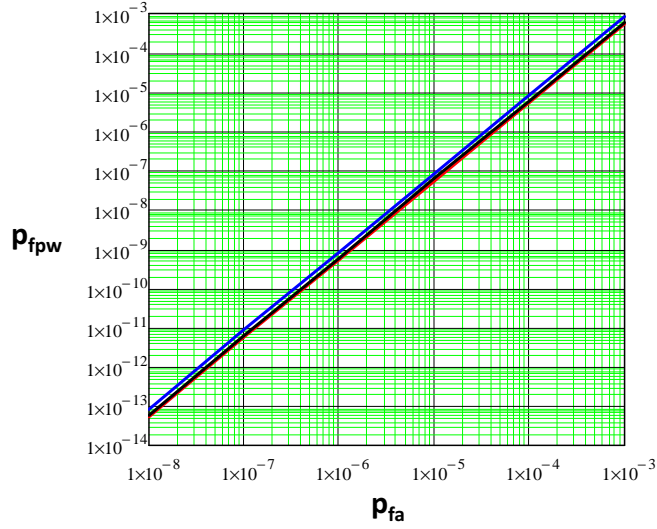
Figure 18: The probability of a false plane wave detection and designation due to receiver noise as a function of the probability of false alarm at each thinned array beam output.

This result assumes that in each case, the p secondary array beam positions of size q_b are different and statistically independent. The denominator assures that the modified binomial distribution is a valid probability distribution (sums to one). Figure 18 shows the probability of a false plane wave detection and designation due to receiver noise as a function of the probability of false alarm at each thinned array beam output. We show here combinations of baseline and secondary thinned arrays of
$(a, b) = (1, 2), (1, 3)$, and $(2, 3)$ in overlapping curves. Asymptotically we find from Equation (11) that

$$p_{fpw} = \frac{q_b}{q_a} N_{el} p_{fa}^2 + O(p_{fa}^3)$$

as $p_{fa} \to 0$. This approximation matches well the results of Figure 18.

Note that for small p_{fa}, the probability of a false plane wave detection and designation is much smaller than the probability of false alarm at each DFT beam position. This is a fortunate result of the two stage detection process using plane wave detections on both the baseline and secondary thinned array DFT responses.

Conclusions and Recommendations for Further Study

We analyzed the performance of coprime, thinned linear arrays. A linear array is formed where the number of elements with half wavelength spacing in the array is given by the product of three relatively prime integers. Three thinned arrays are formed by thinning with each of the prime integers. The DFT was used with each of the thinned arrays to form multiple beams with ambiguous grating lobes. The ambiguity in the multiple possible angles of arrival of a plane wave can be resolved by solution to Diophantine equations characteristic of thinned array pairs. We demonstrated that comparison of the multiple, possible angles of arrival in two coprime arrays results in a unique angle of arrival for a single plane wave excitation, assuming that the plane wave arrives from physically realizable angles of arrival. For each pair of coprime thinned arrays, we formed a hash table relating DFT output sample pairs to a unique angle of arrival.

We illustrated the process of plane wave signal detection and angle of arrival designation with a sample problem. A complication occurred when multiple plane waves excite the arrays resulting in the need to correctly associate multiple DFT output samples between the thinned arrays. This complication was resolved by applying the realizability condition on solutions to the Diophantine equations for the plane wave angles of arrival. An additional complication occurs when multiple plane waves register in a single DFT output sample. In some of these cases, the complications must be resolved by observing only a few, selected DFT output samples from a third thinned array. This is an important point since our investigation is motivated by the need to reduce the digital beamforming processing rates in a sparse signal environment. In fact, only the DFT samples associated with angles of arrival in the sparse signal environment need to be computed. Fewer computations are required for the beamforming response to a few signals than are required for the complete DFT implemented as the FFT on the third thinned array.

Two measures of performance of the coprime thinned arrays are provided. First, we considered improvements in the DFT beamforming processing rates assuming use of the conventional Fast Fourier Transform (FFT) with thinned array pairs. The thinned array processing rates required for plane wave detection and angle of arrival designation were compared to FFT beamforming with the complete, non-thinned array. Processing rates with the thinned arrays were 15% - 26% of the rates required for the fully filled array, depending on the thinned array pairs used. These efficiencies were computed assuming zero padding of the thinned array samples to employ the FFT algorithm in the beamforming. This comparison of beamforming processing rates is important for consideration of sFFT processing for practical ESM array applications.

Second, we considered the impact of receiver noise on the performance of the plane wave signal detection and angle designation. We assumed receiver noise added to each of the thinned array signal voltages and employed conventional detection processing at each of the DFT output samples. We provided expressions for the probability of plane wave detection and designation and the probability of missed plane wave detection and designation as a function of element signal to noise ratio with numerical values for the sample thinned array problem. Thinned array pairings and probability of false alarm served as parameters in these results. We also gave estimates of the probability of false plane wave detection and designation due to receiver noise as a function of the probability of false alarm at each DFT output sample. The dual detection process implicit in the use of two thinned arrays results in a substantial reduction in false plane wave detections due to receiver noise, beyond the false alarm level set at the DFT sample level.

We conducted this study to assess the feasibility of using thinned arrays in wideband, wide angle scanned phased arrays for ESM applications where a sparse signal environment exists in space and frequency. The thinned arrays and sFFT processing could reduce digital beamforming processing rates that surpass current hardware technology capabilities. While this preliminary study is encouraging, further analyses remain. Practical implementation requires extension of sFFT processing to two dimensions (azimuth and elevation scanned arrays) and three dimensions (azimuth and elevation scanned arrays with frequency scanning in each beam position). Recent research has extended sFFT algorithms to two dimensions [10,11,12] and indicates applying successively one dimensional sFFTs to rows and columns is not the appropriate approach. The performance of these advances in beamforming computational rate and detection/false detection probabilities as a function of sparse signal complexity is required. Further, the application of these advanced algorithms to thinned arrays formed with analog sub-arrays and bandpass receivers should be investigated in terms of pattern performance, sparse signal complexity, computational complexity, and detection performance. Restrictions on array sizes formed from the products of coprime integers needs to be investigated in terms of limits on practical application. The compatibility of coprime thinning and the requirement for data zero padding to effectively use FFT algorithms needs to be investigated.

32

References

[1] Gilbert, A. C., et al, "A Tutorial on Fast Fourier Sampling," IEEE Signal Processing Magazine, March 2008, pp 57-66.

[2] Gilbert, A. C., et al, "Recent Developments in the Sparse Fourier Transform," IEEE Signal Processing Magazine, September 2014, pp 91- 100.

[3] Katabi, D., et al, "The Sparse FFT - From Theory to Practice," Presentation at the 2013 Workshop on Sparse Fourier Transform, February 2013, MIT Computer Science and Artificial Intelligence Laboratory.

[4] Hassanieh, H., et al, "Faster GPS via the Sparse Fourier Transform," Presentation at the 2013 Workshop on Sparse Fourier Transform, February 2013, MIT Computer Science and Artificial Intelligence Laboratory.

[5] Agarwal, A., "FPGA-based Design of a Million Point Sparse FFT," Presentation at the 2013 Workshop on Sparse Fourier Transform, February 2013, MIT Computer Science and Artificial Intelligence Laboratory.

[6] Hassanieh, H., et al, "GHz-Wide Sensing and Decoding Using the Sparse Fourier Transform," Proceedings of the 33rd Annual IEEE International Conference on Computer Communications (INFOCOM'14), April 27th - May 2nd, 2014, pp 2256-2264.

[7] Hassanieh, H., et al, "Big Band: GHz-Wide Sensing and Decoding on Commodity Radios," Technical Report MIT-CSAIL-TR-2013-009, MIT Computer Science and Artificial Intelligence Laboratory, May 2013.

[8] Boufounos, P., "Fourier Methods in Array Processing," Presentation at the 2013 Workshop on Sparse Fourier Transform, February 2013, MIT Computer Science and Artificial Intelligence Laboratory.

[9] Yavne, R., "An Economical Method for Calculating the Discrete Fourier Transform," Proceedings of the American Federation of Information Processing Societies (AFIPS) Fall Joint Computer Conference, Vol. 33, 1968, pp 115-125.

[10] Rauh, A. and G. R. Arce, "Sparse 2D Fast Fourier Transform," Proceeding of the 10th International Conference on Sampling Theory and Applications, July 2013.

[11] Ghazi, H., et al, "Sample Optimal Average Case Sparse Fourier Transform in Two Dimensions," 51st Annual Allerton Conference on Communications, Control and Computing, October 2013 pp 1258-1265.

[12] Chew, W. C. and J. M. Song, "Fast Fourier Transform of Sparse Spatial Data to Sparse Fourier Data," Proceedings of the 2000 IEEE Antennas and Propagation Society, July 2000, pp 2324-2327.

3. A General Anisotropic Representation for Spatially and Temporally Dispersive Media that Separates Electric and Magnetic Polarization Effects.

Arthur D. Yaghjian

3.1 Introduction

The rigorous homogenization of natural materials and metamaterials must take into account spatial dispersion as well as temporal dispersion, that is, it must formulate constitutive parameters that depend on the spatial as well as frequency variation of the fields. This has been done in the past by Landau and Lifshitz [1] and Agranovich and Ginzburg [2] using a method that combines the electric and magnetic polarization into a single permittivity tensor. Therefore, the research that was proposed and which has been accomplished was to formulate a general anisotropic representation for spatially and temporally dispersive media that separates electric and magnetic polarization effects.

3.2 Exact Causal Solution for Macroscopic Permittivity and Permeability Tensors

An exact causal solution was determined for macroscopic permittivity and permeability tensors that are conveniently computed from the microscopic Maxwell equations. The theory generalizes the method of Landau and Lifshitz and constitutes the first rigorous characterization of spatial dispersion that explicitly applies to magnetic (or diamagnetic) as well as electric materials. The theory was immediately used to determine a causal permeability for diamagnetic metamaterials, specifically, a three-dimensional array of perfectly electrically conducting spheres — a classic problem that had previously defied solution [3]. By enhancing the understanding of spatial dispersion, the theory facilitates the continued understanding and development of materials. As an integral part of the theory, which was published as both an invited book chapter [4] and a feature journal article [5], detailed reality conditions, reciprocity relations, passivity conditions, and causality relations were derived for the macroscopic anisotropic permittivities and permeabilities. Criteria that can be evaluated numerically was found for deciding if the electrical separation distance is small enough for an array of inclusions to behave as a continuum satisfying Maxwell's macroscopic equations [6], and for a free-space/array interface to satisfy continuum boundary conditions [7]. The general three-dimensional formulation was also modified to determine the constitutive parameters of one-dimensional magnetodielectric periodic structures [8].

The electric and magnetic theory of spatial dispersion was also applied to resolve four fundamental issues in classical electromagnetics [9]: i) The conventional (spatially nondispersive) macroscopic definition of magnetiz-ation and, thus, the permeability becomes physically meaningless as the wavelength approaches the size of the unit cell. ii) The definition of multipole moments of higher-order than electric dipoles becomes origin depen-dent as the size of the unit cell becomes comparable to a wavelength and, thus, magnetization as well as all other higher-order moments cannot be uniquely defined at high frequencies. iii) It is mathematically impossible for conventionally defined permeability that is diamagnetic at low frequencies to be a causal function of frequency satisfying the Kramers-Kronig relations. iiii) In a multipole

expansion, electric quadrupole moments appear to contribute to the same order as magnetic dipole moments, yet at low frequencies they are seldom significant in dipolar material.

3.3 Generalized Claussius-Mossotti Procedure for Obtaining the Low-frequency Constituitive Parameters of Electric Quadrupolar Material

Another spin-off of the theory has been its facilitating a generalized Claussius-Mossotti procedure to obtain in closed form the low-frequency constitutive parameters of electric quadrupolar material [10]. This generalized Claussius-Mossotti derivation is the first application of the Clausius-Mossotti method to media containing multipoles of higher order than dipoles and it opens the way to the Clausius-Mossotti homogenization of higher-order multipolar media.

3.4 Determination of the Quality-factor (Q) Lower Bounds that Apply to Electrically Small, Lossy or Lossless, Combined Electric and Magnetic Dipole Antennas Confined to an Arbitrarily Shaped Volume

After accomplishing more than the proposed tasks on developing "a general macroscopic anisotropic representation for spatially dispersive media," Yaghjian conducted an intensive research effort into determining the quality-factor (Q) lower bounds that apply to electrically small, lossy or lossless, combined electric and magnetic dipole antennas confined to an arbitrarily shaped volume. Lower-bound formulas for Q were derived for dipole antennas with specified electric and magnetic dipole moments excited by both electric and magnetic (or magnetization) surface currents as well as by electric surface currents alone. With either excitation, separate formulas were found for the dipole antennas containing only lossless or "nondispersive-conductivity" material and for the dipole antennas containing "highly dispersive lossy" material. The formulas prove useful to the engineering and physics communities because they involve only the quasi-static electric and magnetic polarizabilities of the associated perfectly conducting volume of the antenna, the ratio of the powers radiated by the specified electric and magnetic dipole moments, and the efficiency of the antenna. The work was invited to a special issue of Progress in Electromagnetics Research devoted to the memory of Professor Robert E. Collin [11].

A rather extraordinary prediction arose from the formulation of Q-energy related to the quality factor of highly lossy dispersive material. By using highly dispersive lossy material in the tuning element of an electrically small antenna, the antenna can be tuned without increasing the stored energy or the quality factor. This led to a new formula for the minimum Q of an electrically small electric or magnetic dipole antenna, namely $Q = 0.5\eta / (ka)^3$ for a spherical antenna (ka is the electrical radius of the sphere and η is the radiation efficiency of the antenna) — one half the Chu lower bound or twice the bandwidth previously considered possible. Examples using hypothetical Lorentz material confirmed this unexpected prediction [12].

3.5 References
[1] L.D. Landau, E.M. Lifshitz, and L.P. Pitaevskii, *Electrodynamics of Continuous Media*, 2nd edition, Oxford, England: Pergamon Press, 1984, ch. XII.

[2] V.M. Agranovich and V.L. Ginzburg, *Crystal Optics with Spatial Dispersion, and Excitons*, 2nd edition, Berlin, Springer-Verlag, 1984.

[3] A.D. Yaghjian, A. Alù, and M.G. Silveirihna, "Causality of Diamagnetic Materials," *Proceedings of EuCAP*, pp.3309–3313, April 2013.

[4] A.D. Yaghjian, A. Alù, and M.G. Silveirihna "Anisotropic Representation for Spatially Dispersive Periodic Metamaterial Arrays," in *Transformation Electromagnetics and Metamaterials*, Springer, 2014 (Invited).

[5] A.D. Yaghjian, A. Alù, and M.G. Silveirihna, "Homogenization of Spatially Dispersive Metamaterial Arrays in Terms of Generalized Electric and Magnetic Polarizations," *Photonics and Nanostructures – Fundamentals and Applications*, vol. 11, pp. 374–396, November 2013 (Invited).

[6] A.D. Yaghjian, "Definition of an EM Continuum and Boundary Conditions for Electric Quadrupolar Continua," *Proceedings of EMTS*, pp. 656–659, May 2013 (Invited).

[7] A.D. Yaghjian, "Boundary Conditions for Electric Quadrupolar Continua," *Radio Science*, vol. 49, pp. 1289– 1299, December 2014 (Invited).

[8] O. Breinbjerg and A.D. Yaghjian, "Permittivity and Permeability for Floquet-Bloch Space Harmonics in Infinite 1D Magneto-Dielectric Periodic Structures," *Proceedings of Metamaterials*, pp. 70–72, August 2014.

[9] A.D. Yaghjian, "Resolving Some Fundamental Issues in the Representation of EM Materials Using a Rigorous Spatially Dispersive Formulation of Electric and Magnetic Polarizations," *Proc. Metamaterials 2013*, pp. 373–375, September 2013 (Invited).

[10] A.D. Yaghjian, "Generalized Claussius-Mossotti Homogenization for the Permittivity of an Electric Quadru-polar Medium," *Proc. of the Int'l Conf. Days on Diffraction*, pp. 240–246, May 2014 (Invited).

[11] A.D. Yaghjian, M. Gustafsson, and B.L.G. Jonsson, "Minimum Q for Lossy and Lossless Electrically Small Dipole Antennas," *PIER*, vol. 143, pp. 641–673, November 2013 (Invited).

[12] A.D. Yaghjian, M. Gustafsson, and B.L.G. Jonsson "Quality Factor for Antennas (A Tutorial)," *FERMAT*, vol. 4, July-August, 2014 (Invited).

4. Plane-wave Expansions with Directional Spectra; Gaussian-beam Scattering-matrix Theory; and Array Realizations of Complex-source Beams

Thorkild B. Hansen

4.1 Plane-wave Expansions with Directional Spectra

Plane-wave expansions have been useful for solving a large variety of problems involving acoustic and electromagnetic fields. In particular, transducer and antenna theory is often formulated in terms of plane waves because transmission and reception phenomena can be treated straightforwardly with plane waves. Moreover, numerical methods for solving scattering problems, such as the fast multipole method (FMM) also rely on plane-wave expansions. The fact that plane-wave expansions are diagonalized is the key to their usefulness in numerical calculations. Diagonalization simply means that each outgoing plane wave created by a source gives rise to only one incoming plane wave in the receiver region, which contains the observation points.

New exact plane-wave expansions were derived for general acoustic and electromagnetic fields radiated by arbitrary sources of finite extent in both 2D and 3D. The spectra of these expansions equal the product of a Gaussian translation operator and the far-field patterns of the sources evaluated on the real unit circle in 2D and on the real unit-sphere in 3D. At high frequencies, the Gaussian translation operator decays exponentially outside the stationary-point cone determined by the boundaries of the source region as viewed from the receiver region. Hence, the directionality of the Gaussian translation operator makes it possible to disregard a large fraction of the plane-wave translations.

The derivation involves analytic continuation of Gegenbauer's addition theorem to obtain an exact plane-wave expansion of a real point-source field from which the Gaussian translation operator emerges. Sampling theorems determine the plane-wave sampling rate required by the Gaussian translation operator, and since the formulation is based on an exact identity, arbitrarily high accuracy can be achieved. The required sampling rate depends not only on the diameter of the source and receiver regions but also on the actual locations of the sources and receivers within those regions.

For antenna applications, a corresponding plane-wave antenna transmission formula was obtained in which the patterns of the transmitting and receiving antennas are multiplied by the Gaussian translation operator. Hence, at sufficiently high frequencies, the spectrum is guaranteed to be directional, regardless of the patterns of the transmitting and receiving antennas. In such situations, the antenna interaction can be computed to a prescribed accuracy from the antenna pattern values inside cones.

The problem of antenna near-field scanning in 3D was used as an application example. A multilevel computation scheme was formulated with the Gaussian translation operator to determine the far-field pattern of the antenna under test (AUT) from the measured probe output. It was demonstrated that the reduction in computational effort (as compared to the conventional FMM

approach) achievable with the Gaussian translation operator in typical near-field scanning geometries is in the range from 75% to 90% depending on the probe-AUT separation. In addition, it was shown that due to its directionality, the Gaussian translation operator can significantly improve the condition number of the normal equation that determines the AUT far-field pattern from the probe output. This improvement will help speed up the convergence rate of iterative solvers. Further, the Gaussian translation operator can be used when the probe pattern is known only in one hemisphere, as is common in practice (the standard FMM translation operator requires that the probe pattern be known over the entire unit sphere).

Other researchers had previously attempted to obtain directional plane-wave expansions in 2D and 3D. The previous 2D work either involved heuristic (non-exact) plane-wave expansions or plane-wave expansions that require that the source pattern be evaluated at complex angles. Previous 3D work, which also requires that the source pattern be evaluated at complex angles, produced only a semi-directional spectrum that works well only for quasi-planar geometries. None of this previous work produced exact sampling theorems that ensure a prescribed accuracy.

The new exact plane-wave expansions derived in this project are completely general and apply to arbitrary acoustic and electromagnetic fields. They represent new exact wave expansions that are not simply optimizations of previous work or numerical tricks that work only in special situations. Indeed, there are only a handful of exact plane-wave expansions in existence, and the Gaussian translation operator represents one of them. Hence, in addition to the applications explored here, these new expansions may well give rise to unforeseen future uses.

The publications related to this subject are listed in section 4.4 and can be classified as follows

- Scalar fields in 2D: [1], [3], [8]
- Scalar fields in 3D: [2]
- Electromagnetic fields in 3D: [4]
- Antenna transmission formula: [4]
- Near-field scanning: [5] (under review, attached in Section 4.5: Appendix)

4.2 Gaussian-beam Scattering Matrix Theory
A scattering problem consists of determining the scattered field from some object that is illuminated by a primary field. Scattering-matrix theories solve this problem by relating the expansion coefficients of the scattered field to the expansion coefficients of the primary field. For example, in Kerns' plane-wave scattering-matrix theory, the plane-wave spectrum of the scattered field is expressed in terms of the plane-wave spectrum of the primary field and a scattering matrix unique to the scatterer. Similarly, with Waterman's spherical-wave scattering-matrix theory (often referred to as the T-matrix method), the spherical-wave expansion coefficients of the scattered and primary fields are related through a matrix equation.

Neither the plane-wave scattering matrix nor the T-matrix employ directional basis fields and as a consequence to ensure high accuracy one must in general perform "full" calculations even if the primary source and the receiver regions are of limited extent.

A new exact scattering-matrix theory that is as general as the two theories mentioned above was derived in this project. It employs directional basis fields (Gaussian beams) that make it possible to reduce the computational effort for certain configurations. More importantly, it demonstrated, for the first time, that any scattering body can be replaced by a set of receiving and transmitting beams whose weights are related through the Gaussian scattering matrix. Hence, this work provides an entirely new way of characterizing scattering bodies. This representation also appears to be useful for numerical computations and radar simulations.

The publications related to this subject are listed in section 4.4. Publication [6], under review, is attached in Section 4.5: Appendix)

- Scalar fields in 3D: [6]
- Electromagnetic fields in 3D: [9]

4.3 Array Realizations of Complex-source Beams

Complex-source beams are exact solutions to the wave equation that were first introduced in the frequency domain by Deschamps in 1971. These beams are used in both acoustic and electromagnetic wave theories and are often referred to as Gaussian beams in the frequency domain and as pulsed-beam wavelets or complex-source pulsed beams in the time domain.

Due to their usefulness in various forward and inverse wave-propagation problems, several papers by other researchers have been devoted to obtaining volume and surface sources that radiate complex-source beams. In this project, the inverse source problem for the complex-source beam was investigated as an array optimization problem. The excitation coefficients were determined from a least-squares solution for array elements that each has a typical pattern of a small radiator with sidelobes. By extending a 2D theorem on the spatial bandwidth of complex-source beams, it was shown that for any nonzero error tolerance, the physical dimension of the array is smaller than the diameter of the branch-cut disk of the complex point source, provided that this branch-cut disk is at least a couple of wavelengths across.

The following publication related to the array realizations of complex-source beams is listed in section 5.4. This publication, under review, is attached in Section 4.5: Appendix.

- Scalar fields in 3D: [7]

4.4 References
Journal Articles in Peer-Reviewed Journals:
[1] T.B. Hansen, "Translation operator based on Gaussian beams for the fast multipole method in two dimensions," *Wave Motion*, vol. 50, pp.793-808, June 2013.

[2] T.B. Hansen, "Translation operator based on Gaussian beams for the fast multipole method in three dimensions," *Wave Motion*, vol. 50, pp.940-954, July 2013.

[3] T.B. Hansen, "Numerical properties of a Gaussian translation operator for the 2D FMM," *IEEE Transactions on Antennas Propagation*, vol. 62, pp. 3119-3129, June 2014.

[4] T.B. Hansen, "Exact plane-wave expansion with directional spectrum: application to transmitting and receiving antennas*, IEEE Transactions on Antennas Propagation*, vol. 62,pp. 4187-4198, August 2014.

[5] T.B. Hansen and O. Borries, "Gaussian translation operator in a multi-level scheme," *Radio Science", in review.*

[6] T.B. Hansen, "Exact Scattering-Matrix Theory Based on Gaussian Beams," *Journal of the Acoustical Society America,* in review.

[7] T.B. Hansen, "Array realization of complex-source beam," *Wave Motion*, in review.

Conference Articles in Peer-Reviewed Proceedings:
[8] T.B. Hansen, "Translation operator based on Gaussian beams," *2013 IEEE International Symposium on Antennas and Propagation and USNC-URSI National Radio Science Meeting,* Orlando, Florida, USA, July 7-12, 2013, paper no. 2808.

[9] T.B. Hansen, "Electromagnetic scattering-matrix theories based on plane waves and complex-source beams,'' *Progress In Electromagnetics Research Symposium*, Prague, Czech Republic, European Union, July 6-9, 2015, 5 pp., invited.

Invited Lectures:
[10] T.B. Hansen, "Spherical near-field scanning with higher-order probes," Syracuse University, Syracuse, NY, April 26, 2012. Organized by the Syracuse Chapter of the AP/MTT/EMC Societies of the IEEE. Additional support provided by CASE and the L.C. Smith College of Engineering at Syracuse University.

[11] T.B. Hansen, "Spherical near-field scanning with higher-order probes," TICRA, Copenhagen, Denmark, December 17, 2012.

4.5 Appendix

4.5.1

Gaussian translation operator in a multi-level scheme

Thorkild B. Hansen,[1] and Oscar Borries[2]

Corresponding author: Thorkild B. Hansen, Seknion Inc., Boston, MA, USA. (thorkild.hansen@att.net)

[1]Seknion Inc., Boston, MA, USA.

[2]TICRA, Copenhagen, Denmark.

A multilevel computation scheme for time-harmonic fields in three dimensions will be formulated with a new Gaussian translation operator that decays exponentially outside a circular cone centered on the line connecting the source and observation groups. This Gaussian translation operator is directional and diagonal with its sharpness determined by a beam parameter. When the beam parameter is set to zero, the Gaussian translation operator reduces to the standard FMM translation operator. The directionality of the Gaussian translation operator makes it possible to reduce the number of plane waves required to achieve a given accuracy. The sampling rate can be determined straightforwardly to achieve any desired accuracy. The use of the computation scheme will be illustrated through a near-field scanning problem where the far-field pattern of a source is determined from near-field measurements with a known probe. Here, the Gaussian translation operator improves the condition number of the matrix equation that determines the far-field pattern. The Gaussian translation operator can also be used when the probe pattern is known only in one hemisphere, as is common in practice.

1. Introduction

Fast computation methods like the fast multipole method (FMM) [*Rokhlin*, 1990], [*Coifman et al.*, 1993], [*Song et al.*, 1997], [*Chew et al.*, 2006], [*Ergül et al.*, 2014] use plane-wave expansions [*Kerns*, 1981], [*Hansen et al.*, 1999] to compute the field in a receiver group due to sources in a source group. The spectrum of one such plane-wave expansion equals the product of the source far-field pattern and a so-called translation operator. The translation operator converts outgoing plane waves from the source group to incoming plane waves at the receiver group. Since the basis functions are plane waves, each outgoing plane wave gives rise to only one incoming plane wave, and the translation operator is said to be diagonal.

The standard translation operators used widely in the time-harmonic FMM [*Rokhlin*, 1990], [*Coifman et al.*, 1993] emerges from an exact field representation and therefore can achieve any desired accuracy. Moreover, sampling rules prescribe exactly how to achieve any desired accuracy. In two dimensions the far-field pattern of the source needs only be sampled at equidistant angles over the interval from 0 to 2π. In three dimensions the far-field pattern of the source needs only be sampled on the unit sphere.

However, these standard translation operators are not sufficiently directional to make it possible to disregard a large fraction of the plane waves, even for large well-separated groups. Most often one must include plane waves propagating in all directions, not just plane waves propagating in an angular region centered on the direction from the source group to the receiver group.

To reduce the required number of plane waves, a number of different directional translation operators were derived for two dimensions [*Wagner et al.*, 1994], [*Burkholder et al.*, 1996], [*Michielssen et al.*, 1996], [*Hu et al.*, 1999]. The ray-propagation FMM papers [*Wagner et al.*, 1994] and [*Burkholder et al.*, 1996], which inspired the present work, derive approximate translation operators using a windowing technique and high-frequency asymptotics, respectively. In the steepest-descent FMM papers [*Michielssen et al.*, 1996] and [*Hu et al.*, 1999] the translation operator is obtained from a contour-integral representation of the Hankel function. The algorithm in [*Hu et al.*, 1999] outperforms (see [*Hu et al.*, 1999, p.760]) the previous algorithms [*Wagner et al.*, 1994], [*Burkholder et al.*, 1996], [*Michielssen et al.*, 1996].

The starting point of the derivation in [*Hu et al.*, 1999] is an exact contour-integral representation of the Hankel function given by [*Hu et al.*, 1999, eq.(4)]. The contour is deformed to a modified steepest-descent path, so that the far-field pattern of the source must be evaluated at complex angles of observation. Therefore, one must use interpolation/extrapolation techniques to evaluate the far-field pattern of the source at the required complex observation directions. Also, different pattern discretizations are needed at different portions of the complex integration contour. Hence, the translation operator from [*Hu et al.*, 1999] is considerably more complicated to implement than the standard 2D translation operator from [*Rokhlin*, 1990].

In three dimensions, the 3D steepest-descent FMM [*Chew et al.*, 2006, ch.17] was developed to reduce the number of plane waves required for quasi-planar source-receiver geometries. With this approach, only plane waves in a narrow range of

angles near the horizon are needed, thus improving performance over the standard FMM. In other words, in the 3D steepest-descent FMM the translation operator is directional in one dimension along the quasi-planar source-receiver geometry. As the name implies, it employs a steepest-descent contour-integral representation of the Green's function. Therefore, evanescent plane waves come into play and the far-field pattern of the source must be evaluated at complex angles of observation. As a result, the steepest-descent FMM employs an integration scheme that is more complicated than the one used in the present paper and in the standard FMM.

The present paper employs a new directional translation operator (called the Gaussian translation operator) in a multilevel scheme in three dimensions. The Gaussian translation operator was derived in [*Hansen*, 2013c] by combining Gaussian beams and plane-wave expansions. It was extended to electromagnetic fields in [*Hansen*, 2014b]. Since the Gaussian translation operator emerges from an exact representation, any desired accuracy, all the way to machine precision, can be achieved. Moreover, the Gaussian translation operator requires only that the far-field pattern of the source be sampled over the unit sphere. The paper [*Hansen*, 2013a] derives the corresponding two-dimensional Gaussian translation operator, which is numerically examined in [*Hansen*, 2014a]. In contrast, to the quasi-planar configuration used in the 3D steepest-descent FMM [*Chew et al.*, 2006, ch. 17], the plane-wave expansion of the present paper is designed to reduce the number of required plane waves for source-receiver geometries where the receivers lie inside a circular cone when observed

from each point in the source region. Hence, the Gaussian translation operator decays

exponentially outside a circular cone.

We shall set up the multilevel scheme for the problem where the near field of an

electromagnetic source is recorded by a probe on a surrounding surface, similar to the

problem considered in [*Schmidt et al.*, 2009]. The goal is to determine the far-field

pattern of the source (antenna under test) from the recorded probe output.

The paper is organized as follows. In Section 2 we formulate the near-field scan-

ning problem in terms of a matrix equation. Section 3 describes a multilevel group

structure for the probe positions on the scanning surface. Section 4 employs the

Gaussian translation operator to compute the plane-wave expansions in groups at

the coarsest level. In Section 5 we compute the plane-wave expansions at lower levels

using anterpolation. The actual probe output is computed in Section 6 using the

plane-wave receiving characteristic of the probe. Multiplication by the Hermitian

conjugate matrix (needed to obtain the least-squares solution) is discussed in Section

7.

The special case of the Hertzian dipole probe scanning a sphere is considered in

Section 8. In Section 9 we present numerical examples to illustrate the benefits

achievable with the Gaussian translation operator in near-field scanning problems.

Finally, Section 10 contains conclusions.

The standard rectangular coordinates are denoted by (x, y, z) with unit vectors

$\hat{\mathbf{x}}$, $\hat{\mathbf{y}}$, and $\hat{\mathbf{z}}$, so that a general point can be expressed as $\mathbf{r} = x\hat{\mathbf{x}} + y\hat{\mathbf{y}} + z\hat{\mathbf{z}}$. The

spherical coordinate (r, θ, ϕ) are related to the rectangular coordinates through $x =$

105 $r \sin\theta \cos\phi$, $y = r \sin\theta \sin\phi$, and $z = r \cos\theta$ with the radial unit vector given by

106 $\hat{\mathbf{r}} = \hat{\mathbf{x}} \sin\theta \cos\phi + \hat{\mathbf{y}} \sin\theta \sin\phi + \hat{\mathbf{z}} \cos\theta$. The two other spherical unit vectors are

107 $\hat{\boldsymbol{\theta}} = \hat{\mathbf{x}} \cos\theta \cos\phi + \hat{\mathbf{y}} \cos\theta \sin\phi - \hat{\mathbf{z}} \sin\theta$ and $\hat{\boldsymbol{\phi}} = -\hat{\mathbf{x}} \sin\phi + \hat{\mathbf{y}} \cos\phi$. Throughout,

108 $e^{-i\omega t}$ time dependence with $\omega > 0$ is assumed and suppressed. The wave number is

109 $k = 2\pi/\lambda = \omega/c$, with c being the wave speed and λ the wavelength.

2. Matrix formulation of general near-field scanning problem

110 Figure 1 shows the scanning geometry for the antenna under test (AUT) with its

111 reference point at that origin. The output of a probe is recorded on a surface S that

112 contains the AUT. All points on S are assumed a couple of wavelengths from the

113 AUT so that multiple interactions can be neglected.

The far-field pattern $\boldsymbol{\mathcal{F}}(\hat{\mathbf{r}})$ of the electric field $\mathbf{E}(\mathbf{r})$ of the AUT is given by [*Hansen et al.*, 1999, eq.(3.13)]

$$\boldsymbol{\mathcal{F}}(\hat{\mathbf{r}}) = \lim_{r \to \infty} \mathbf{E}(r\hat{\mathbf{r}}) \, r \, e^{-ikr} \tag{1}$$

so that the electric far field is

$$\mathbf{E}(\mathbf{r}) \sim \frac{\boldsymbol{\mathcal{F}}(\hat{\mathbf{r}}) \, e^{ikr}}{r}, \quad r \to \infty. \tag{2}$$

114 We emphasize that the far-field pattern $\boldsymbol{\mathcal{F}}(\hat{\mathbf{r}})$ corresponds to a certain fixed orienta-

115 tion of the AUT when its reference point is at the origin.

116 The probe output due to the field of the AUT is recorded on S when the probe

117 reference point is at $\mathbf{r}_p$ with $p = 1, 2, ..., P$. The probe orientation is determined by

118 the subscript q, which can be either 1 or 2. The corresponding probe output is V_{pq}.

119 For example, if S is a sphere and the probe is a tangential electric dipole, we would

120   let $q = 1$ and $q = 2$ indicate that the dipole is parallel to the θ and ϕ unit vectors,

121   respectively. If the probe has two output ports, there is only one physical probe

122   orientation at each $\mathbf{r}_p$, and the subscript q is simply the port number.

The unknown values of the AUT pattern are arranged in a vector $\mathbf{F}$. In other

words, $\mathbf{F}$ contains the unknown pattern values for both polarizations over the unit

sphere of directions. Let the recorded probe output collected over the scan surface S

be arranged in the vector $\mathbf{V}$. Since multiple interactions can be neglected, we have a

matrix formula for the probe output in terms of the AUT far-field pattern:

$$\bar{\mathbf{M}} \, \mathbf{F} = \mathbf{V} \tag{3}$$

where $\bar{\mathbf{M}}$ is the system matrix. The least-squares solution to (3) satisfies the normal

equation

$$\bar{\mathbf{M}}^H \, \bar{\mathbf{M}} \, \mathbf{F} = \bar{\mathbf{M}}^H \, \mathbf{V} \tag{4}$$

123   where $\bar{\mathbf{M}}^H$ is the Hermetian conjugate of $\bar{\mathbf{M}}$.

124   To solve (4) for $\mathbf{F}$ with an iterative scheme requires the computation of numer-

125   ous matrix-vector products involving both $\bar{\mathbf{M}}$ and $\bar{\mathbf{M}}^H$. In this paper we speed up

126   the computation of these matrix-vector products using the multilevel fast multipole

127   method with the Gaussian translation operator.

3. Multilevel group structure

128   The probe reference points $\mathbf{r}_p$ on the surface S will now be arranged in a multilevel

129   group structure with H levels. The group diameter and the number of groups at level

130   h is denoted by D_h and G_h, respectively. The center points for the groups at level

131 h are $\mathbf{r}_{g,h}$ with $g = 1, 2, 3, ..., G_h$. We refer to the level with the largest and smallest

132 group diameters as the coarsest and finest levels, respectively.

133   As shown in Figure 2, the coarsest-level groups have the same dimension as the

134 AUT. The dimension of the AUT is the diameter $2R_{AUT}$ of the minimum sphere

135 centered at the origin that contains the AUT. The coarsest-level groups on S are

136 thus also chosen to have diameter $D_H = 2R_{AUT}$.

137   It is critically important that the following rule be obeyed when groups are created.

138 For all points $\mathbf{r}_p$ in a group, the sphere that bounds the group must contain the

139 physical probe when its reference point is located at $\mathbf{r}_p$. For example, if a point $\mathbf{r}_p$

140 is inside but extremely close the to boundary of one such sphere, this point cannot

141 be part of the group since the physical probe would not be contained in the sphere

142 when its reference point is at $\mathbf{r}_p$.

143   The groups at level $h = H - 1$ are obtained by dividing each of the groups at

144 level $h = H$ into eight. Hence, the diameter of the groups at level $h = H - 1$ is

145 $D_{H-1} = \frac{1}{2}D_H$. This process of halving the group diameters is continued until we

146 reach the finest level $h = 1$, where the diameter is D_1. Naturally, we must choose D_1

147 greater than the diameter of the probe.

4. Plane-wave expansions for the coarsest-level groups

The electric field in group g at the coarsest level $h = H$ can be computed from the

AUT far-field pattern using the plane-wave expansion [*Hansen*, 2014b, eq.(52)]

$$\mathbf{E}(\mathbf{r}) = \frac{ik}{4\pi} \int d\Omega_k \, \boldsymbol{\mathcal{F}}(\hat{\mathbf{k}}) \, T_N(\hat{\mathbf{k}}, \mathbf{r}_{g,H}, \Delta) \, e^{ik\hat{\mathbf{k}} \cdot (\mathbf{r} - \mathbf{r}_{g,H})} \tag{5}$$

where the region of integration is the unit sphere

$$\int d\Omega_k \, F(\hat{\mathbf{k}}) \equiv \int\limits_0^{2\pi} d\phi \int\limits_0^\pi d\theta \, \sin\theta \, F(\hat{\mathbf{x}}\sin\theta\cos\phi + \hat{\mathbf{y}}\sin\theta\sin\phi + \hat{\mathbf{z}}\cos\theta) \qquad (6)$$

and [$Hansen$, 2014b, eq.(49)]

$$T_N(\hat{\mathbf{k}}, \mathbf{r}_{g,H}, \Delta) = e^{k\Delta(\hat{\mathbf{k}}\cdot\hat{\mathbf{r}}_{g,H}-1)} \sum_{n=0}^N i^n(2n+1)\, \tilde{h}_n^{(1)}(k\{|\mathbf{r}_{g,H}| + i\Delta\})\, P_n(\hat{\mathbf{k}}\cdot\hat{\mathbf{r}}_{g,H}) \quad (7)$$

is the Gaussian translation operator with beam parameter Δ. Moreover, $P_n(Z)$ is the Legendre polynomial of order n, and

$$\tilde{h}_n^{(1)}(Z) = h_n^{(1)}(Z)\, e^{\mathrm{Im}(Z)} \qquad (8)$$

148   is the normalized spherical Hankel function of the first kind and order n, with $h_n^{(1)}(Z)$

149   being the standard spherical Hankel function of the first kind and order n. When

150   $\Delta = 0$, the Gaussian translation operator (7) equals the standard 3D translation

151   operator [$Coifman\ et\ al.$, 1993].

We next show how to determine the truncation number N so that the maximum relative error of the plane-wave expansion (5) is less than a selected value $\mathcal{E}$. Details can be found in [$Hansen$, 2014b, sec.VI]. First introduce N_s and $\mathcal{E}_s$ through

$$N = N_s + 2, \qquad \mathcal{E} = \frac{\mathcal{E}_s}{4}. \qquad (9)$$

152   Then define

$$U_n(\mathbf{r}_{g,H}, \Delta, \mathbf{R}_e) = ik(-1)^n(2n+1)\, h_n^{(1)}(k\{|\mathbf{r}_{g,H}| + i\Delta\})$$

$$\cdot j_n\!\left(k\sqrt{(\mathbf{R}_e - i\Delta\hat{\mathbf{r}}_{g,H})^2}\right) P_n\!\left(\frac{\hat{\mathbf{r}}_{g,H}\cdot(\mathbf{R}_e - i\Delta\hat{\mathbf{r}}_{g,H})}{\sqrt{(\mathbf{R}_e - i\Delta\hat{\mathbf{r}}_{g,H})^2}}\right) \qquad (10)$$

where $\mathbf{R}_e$ is a vector with length D_H that results in the slowest decay rate of $U_n(\mathbf{r}_{g,H}, \Delta, \mathbf{R}_e)$. Note that

$$(\mathbf{R}_e - i\Delta\hat{\mathbf{r}}_{g,H})^2 = (\mathbf{R}_e - i\Delta\hat{\mathbf{r}}_{g,H}) \cdot (\mathbf{R}_e - i\Delta\hat{\mathbf{r}}_{g,H}) \tag{11}$$

is a complex number. Finally, for a desired relative accuracy $\mathcal{E}_s$, we determine the smallest N_s so that

$$\left| \sum_{n=N_s+1}^{\infty} U_n(\mathbf{r}_{g,H}, \Delta, \mathbf{R}_e) \right| < \frac{\mathcal{E}_s}{|\mathbf{R}_e + \mathbf{r}_{g,H}|}. \tag{12}$$

When $\Delta = 0$ the following closed-form expression holds [*Chew et al.*, 2006, p. 88]

$$N_s = k|D_H| + \zeta|kD_H|^{1/3}, \qquad \zeta = \frac{(-3\ln\mathcal{E}_s)^{2/3}}{2} \tag{13}$$

where ln is the natural logarithm and $|\mathbf{r}_{g,H}| > N_s/k$ must be satisfied. Notice that when $\Delta = 0$, N_s depends only on $|\mathbf{R}_e| = D_H$. When $\Delta > 0$, N_s depends also on the direction of $\mathbf{R}_e$.

We write (5) as

$$\mathbf{E}(\mathbf{r}) = \frac{1}{4\pi} \int d\Omega_k \, \boldsymbol{\mathcal{S}}_{g,H}(\hat{\mathbf{k}}) \, e^{ik\hat{\mathbf{k}}\cdot(\mathbf{r}-\mathbf{r}_{g,H})} \tag{14}$$

where

$$\boldsymbol{\mathcal{S}}_{g,H}(\hat{\mathbf{k}}) = ik \, \boldsymbol{\mathcal{F}}(\hat{\mathbf{k}}) \, T_N(\hat{\mathbf{k}}, \mathbf{r}_{g,H}, \Delta) \tag{15}$$

is the plane-wave spectrum, which will be used in the next section to compute the plane-wave spectra at lower-level groups.

5. Plane-wave expansions in lower-level groups

We shall now use the plane-wave spectrum (15) along with anterpolation to compute the plane-wave spectrum that determines the field in a group g' at level

$h = H - 1$, which is assumed to be a child of the group g at level $h = H$ where

(14) holds. The formula (14) implies that the field in group g' at level $h = H - 1$ is

$$\mathbf{E}(\mathbf{r}) = \frac{1}{4\pi} \int d\Omega_k \, \boldsymbol{\mathcal{S}}_{g',H-1}(\hat{\mathbf{k}}) \, e^{ik\hat{\mathbf{k}}\cdot(\mathbf{r}-\mathbf{r}_{g',H-1})} \tag{16}$$

with

$$\boldsymbol{\mathcal{S}}_{g',H-1}(\hat{\mathbf{k}}) = \boldsymbol{\mathcal{S}}_{g,H}(\hat{\mathbf{k}}) \, e^{ik\hat{\mathbf{k}}\cdot(\mathbf{r}_{g',H-1}-\mathbf{r}_{g,H})}. \tag{17}$$

158 Since the diameter of the groups at level $h = H - 1$ is half of the diameter of the

159 groups at level $h = H$, we anterpolate the spectrum using a Lagrangian approach

160 with fourth-order polynomials [*Ergül et al.*, 2014, sec. 3.3]. This procedure can be

161 repeated for lower-level groups until $\boldsymbol{\mathcal{S}}_{g,1}(\hat{\mathbf{k}})$ is known for all groups.

6. Probe output in the finest-level groups

The electric field in group g at the finest level $h = 1$ is thus given by the plane-wave

expansion

$$\mathbf{E}(\mathbf{r}) = \frac{1}{4\pi} \int d\Omega_k \, \boldsymbol{\mathcal{S}}_{g,1}(\hat{\mathbf{k}}) \, e^{ik\hat{\mathbf{k}}\cdot(\mathbf{r}-\mathbf{r}_{g,1})}. \tag{18}$$

162 To compute the probe output, we introduce the plane-wave receiving characteristic

163 of the probe at location p and orientation q as $\boldsymbol{\mathcal{R}}_{pq}(\hat{\mathbf{k}})$, so that the probe output is

164 $V = \mathbf{E}_0 \cdot \boldsymbol{\mathcal{R}}_{pq}(\hat{\mathbf{k}})$ when the incident electric field is the plane wave $\mathbf{E}(\mathbf{r}) = \mathbf{E}_0 \, e^{ik\hat{\mathbf{k}}\cdot(\mathbf{r}-\mathbf{r}_p)}$.

Combining the plane-wave expansion (18) with the definition of the plane-wave re-

ceiving characteristic gives us the the following transmission formula that determines

the probe output V_{pq} in terms of the spectrum $\boldsymbol{\mathcal{S}}_{g,1}(\hat{\mathbf{k}})$ as

$$V_{pq} = \frac{1}{4\pi} \int d\Omega_k \, \boldsymbol{\mathcal{S}}_{g,1}(\hat{\mathbf{k}}) \cdot \boldsymbol{\mathcal{R}}_{pq}(\hat{\mathbf{k}}) \, e^{ik\hat{\mathbf{k}}\cdot(\mathbf{r}_p-\mathbf{r}_{g,1})} \tag{19}$$

165 when probe location p is in group g at level $h = 1$. The integral (19) is computed

166 numerically in spherical coordinates using the trapezoidal rule in ϕ and a Gauss-

167 Legendre rule in $\cos\theta$.

168 The full computation of the matrix-vector product $\bar{\mathbf{M}}\mathbf{F}$ can be summarized as

169 follows.

170 • The proper sampling rate for the AUT far-field pattern is determined by the

171 truncation number $N_{AUT} = kR_{AUT} + \zeta(kR_{AUT})^{1/3}$. Hence, we start with the AUT

172 far-field pattern sampled at roughly $2(N_{AUT} + 1)^2$ points given by the vector $\mathbf{F}$.

173 • The AUT far-field pattern is then interpolated to obtain its values at $2(N + 1)^2$

174 points, where N is given by (9). Also, the rectangular components of the AUT far-

175 field pattern are computed at each of these $2(N+1)^2$ points from the corresponding θ

176 and ϕ components. To ensure the desired accuracy of the entire computation scheme,

177 it is critically important that the up-sampled AUT far-field pattern is computed

178 accurately.

179 • With these up-sampled rectangular components of the AUT far-field pattern, we

180 use (15) to compute the rectangular components of the incoming plane-wave spectrum

181 in each of the groups at the coarsest level $h = H$.

182 • For $h = H - 1, H - 2, ..., 1$ the incoming plane-wave spectra are computed using

183 phase-shifting and a fourth-order Lagrange anterpolation [*Ergül et al.*, 2014, sec. 3.3].

184 Hence, $\boldsymbol{\mathcal{S}}_{g,1}(\hat{\mathbf{k}})$ are known at each of the finest-level groups.

185 • Finally, the probe outputs V_{pq} are computed using (19) at each of the desired

186 points on the scan surface.

7. Multiplication by the Hermitian conjugate

To solve the normal equation (4) iteratively, we also need to perform vector-matrix multiplications with the Hermitian conjugate matrix $\bar{\mathbf{M}}^H$. This multiplication process starts with the probe outputs and works up the tree using shifting and interpolation. We employ a Lagrangian approach with fourth-order polynomials [*Ergül et al.*, 2014, sec. 3.3]. Once we reach the level $h = H$, we use the complex conjugate of the directional translation operator (7) to complete the process.

8. Hertzian dipole probe scanning a sphere

In this section we consider the special case where the surface S is a sphere of radius R_s and the probe is an electric Hertzian dipole. The probe locations $\mathbf{r}_p$ can be expressed in terms of the spherical coordinates (θ_p, ϕ_p) as

$$\mathbf{r}_p = \hat{\mathbf{x}}\, a \sin\theta_p \cos\phi_p + \hat{\mathbf{y}}\, a \sin\theta_p \sin\phi_p + \hat{\mathbf{z}}\, a \cos\theta_p. \tag{20}$$

We let $q = 1$ correspond to the dipole being parallel to

$$\hat{\boldsymbol{\theta}}_p = \hat{\mathbf{x}}\, \cos\theta_p \cos\phi_p + \hat{\mathbf{y}}\, \cos\theta_p \sin\phi_p - \hat{\mathbf{z}}\, \sin\theta_p \tag{21}$$

and $q = 2$ correspond to the dipole being parallel to

$$\hat{\boldsymbol{\phi}}_p = -\hat{\mathbf{x}}\, \sin\phi_p + \hat{\mathbf{y}}\, \cos\phi_p. \tag{22}$$

Since the output of a Hertzian dipole is proportional to the electric field in the direction of the dipole, we find from (18) that

$$V_{pq} = \frac{\ell}{4\pi}\, \hat{\mathbf{u}}_{pq} \cdot \int d\Omega_k\, \boldsymbol{\mathcal{S}}_{g,1}(\hat{\mathbf{k}})\, e^{ik\hat{\mathbf{k}}\cdot(\mathbf{r}_p - \mathbf{r}_{g,1})} \tag{23}$$

193 where $\hat{\mathbf{u}}_{p1} = \hat{\boldsymbol{\theta}}_p$, $\hat{\mathbf{u}}_{p2} = \hat{\boldsymbol{\phi}}_p$, and ℓ is a length proportional to the dipole moment. The

194 expression (23) could also have been derived by inserting the formula [*Hansen et al.,*

195 1999, eq.(6.64)] for the receiving characteristic of the Hertzian dipole into (19).

196   With the sphere as scanning surface, it is natural to spread the probe positions $\mathbf{r}_p$

197 evenly as follows. First select a set of θ values spaced $\Delta_{\theta\phi}$ apart starting at $\theta = 0$

198 and ending at $\theta = \pi$. For each of these values of θ, a set of ϕ values is selected in

199 the range $0 \le \phi < 2\pi$ so that they are spaced roughly $\Delta_{\theta\phi}$ apart. At the poles, only

200 one ϕ value ($\phi = 0$) is needed. This procedure results in fewer probe positions than

201 would be obtained with a rectangular $\theta - \phi$ grid.

9. Numerical example

202   Next we present numerical examples using the Hertzian dipole probe and spherical

203 scanning surface described in Section 8. The desired relative accuracy is set to $\mathcal{E} =$

204 10^{-3} corresponding to $60\,\mathrm{dB}$, which is the dynamic range of a typical high quality

205 anechoic chamber.

206   We first assume that the minimum sphere containing the AUT has radius $R_{AUT} =$

207 5λ and investigate the savings obtained with the Gaussian translation operator for

208 typical values of the scan-sphere radius: $5R_{AUT} \le R_s \le 10R_{AUT}$. In this configu-

209 ration we have 8100 unknown AUT far-field pattern values and 11654 probe output

210 measurements. We only include plane waves that lie inside the cone where the magni-

211 tude of the translation operator is greater than 10^{-4} times its maximum magnitude.

212 All other plane waves are neglected.

Figure 3 shows the parameter Δ of the Gaussian translation operator as a function of R_s obtained by the following procedure [*Hansen*, 2013c]: First one chooses a value for N that is typically 10% larger than the value used for $\Delta = 0$. Then one determines the largest Δ for the selected value of N that results in an error less than $\mathcal{E}$. Figure 4 shows the corresponding reduction of computational effort achieved with the Gaussian translation operator in the translation and interpolation processes. (Let N_{pw}^g and N_{pw}^s denote the number of plane waves used by the Gaussian and standard translation operators during translation, respectively. Then the dotted line in Figure 4 is simply $1 - N_{pw}^g/N_{pw}^s$.) As expected, the greater the scan radius the greater the savings achieved with the Gaussian translation operator.

Figure 5 shows the magnitude of the standard and Gaussian translation operators for the smallest of the scan spheres under consideration: $R_s = 25\lambda$. This figure shows the exponential decay of the Gaussian translation operator outside the plateau region; see [*Hansen*, 2014b] for a discussion. For this scan sphere four group levels came into play, and $N = 78$ and $N = 86$ for the standard ($\Delta = 0$) and Gaussian ($\Delta = 2.4\lambda$) translation operator, respectively (see Figure 3). Due to its directionality, the Gaussian translation operator reduces the number of plane waves required in the translation by almost 75% (see Figure 4), even though it requires a higher sampling rate.

As a final numerical experiment we considered the smaller problem with $R_{AUT} = 3\lambda$ and $R_s = 15\lambda$. Here the number of far-field pattern values is 3600 and the number of probe outputs is 5306, so the matrix $\bar{\mathbf{M}}$ can be computed explicitly in a reasonable

time period. Based on this computation, we fund that the condition number of the

normal matrix $\bar{\mathbf{M}}^H \bar{\mathbf{M}}$ was $6.4 \cdot 10^{11}$ for the standard translation operator and $3.2 \cdot 10^{10}$

for the Gaussian translation operator with $\Delta = 1.8\lambda$. Hence, the directionality of

the Gaussian translation operator helps improve the condition number of the normal

equation (4) for spherical scanning. [*Schmidt et al.*, 2009] discusses the poor condi-

tioning of the normal matrix for scanning problems. Also, we found that if global

interpolation/anterpolation schemes are used instead of the local ones, the condition

number is on the order of 10^{17}. Therefore, global interpolation/anterpolation schemes

do not work well in the near-field scanning problem.

Using a Hertzian dipole placed at the boundary of the minimum AUT sphere

$r = R_{AUT}$, we verified that the parameters used in this section indeed all lead to a

relative accuracy better than $\mathcal{E} = 10^{-3}$ for the computed probe output.

10. Conclusions

The new directional Gaussian translation operator was used in a multilevel compu-

tation scheme for computing the far-field pattern of an AUT from near-field measure-

ments. The theory was developed for arbitrary probes and arbitrary scan surfaces.

We demonstrated that the reduction in computational effort achievable by the

Gaussian translation operator in typical spherical near-field scanning geometries is

in the range from 75% to 90% depending on the probe-AUT separation. In addition,

it was shown that due to its directionality, the Gaussian translation operator could

improve the condition number of the normal equation that determines the AUT far-

field pattern from the probe output. This improvement will also help speed up the convergence rate of iterative solvers.

References

Burkholder, R.J. and D.H. Kwon, (1996), High-frequency asymptotic acceleration of the fast multipole method, *Radio Science, 31*(5), 1199–1206.

Chew, W.C., J.M. Jin, E. Michielssen, and J. Song, eds, (2006), Fast and Efficient Algorithms in Computational Electromagnetics, *Artech House,* Reprinted January 2006 by CCEML, UIUC.

Coifman, R., V. Rokhlin, and S. Wandzura, (1993), The fast multipole method for the wave equation: A pedestrian prescription, *IEEE Antennas and Propagation Magazine, 35*, 7-12.

Ergül, Ö. and L. Gürel, (2014), The Multilevel Fast Multipole Algorithm (MLFMA) for Solving Large-Scale Computational Electromagnetics Problems, *Wiley.*

Hansen, T.B., and A.D. Yaghjian (1999), Plane-Wave Theory of Time-Domain Fields, *IEEE Press.*

Hansen, T.B. (2013a), Translation operator based on Gaussian beams for the fast multipole method in two dimensions, *Wave Motion, 50*, 793–808.

274 Hansen, T.B. (2013c), Translation operator based on Gaussian beams for the fast

275   multipole method in three dimensions, *Wave Motion, 50*, 940–954.

276 Hansen, T.B. (2014a), Numerical properties of a Gaussian translation operator for

277   the 2D FMM, *IEEE Trans. Antennas Propagat.*, *62*, 3119-3129.

278 Hansen, T.B. (2014b), Exact plane-wave expansion with directional spectrum, *IEEE*

279   *Trans. Antennas Propagat.*, *62*, 4187–4198.

280 Hu, B., W.C. Chew, E. Michielssen, and J.S. Zhao (1999), Fast inhomogeneous plane

281   wave algorithm for the fast analysis of two-dimensional scattering problems, *Radio*

282   *Science, 34*, 759–772.

283 Kerns, D.M. (1981), Plane-Wave Scattering-Matrix Theory of Antennas and

284   Antenna-Antenna Interactions, *NBS Monograph 162*, Washington, DC: U.S. Gov-

285   ernment Printing Office.

286 Michielssen, E. and W.C. Chew (1996), Fast steepest descent path algorithm for

287   analyzing scattering from two-dimensional objects, *Radio Science, 31*, 1215–1224.

288 Rokhlin, V. (1990), Rapid solution of integral equations of scattering theory in two

289   dimensions, *Journal of Computational Physics, 86*, 414–439.

290 Schmidt, C.H., and T.F. Eibert (2009), Multilevel plane wave based near-field far-

291   field transformation for electrically large antennas in free-space or above material

292   halfspace, *IEEE Trans. Antennas Propagat., 57*, 1382–1390.

293 Song, J.M., C.C. Lu, and W.C. Chew, (1997), Multilevel fast multipole algorithm

294   for electromagnetic scattering by large complex objects, *IEEE Trans. Antennas*

295   *Propagat., 45*, 1488–1493.

296 Wagner, R.L. and W.C. Chew (1994), A ray-propagation fast multipole algorithm,

297   *Microwave and Optical Technology Letters, 7*(10), 435–438.

Scan surface *S* surrounding AUT

AUT
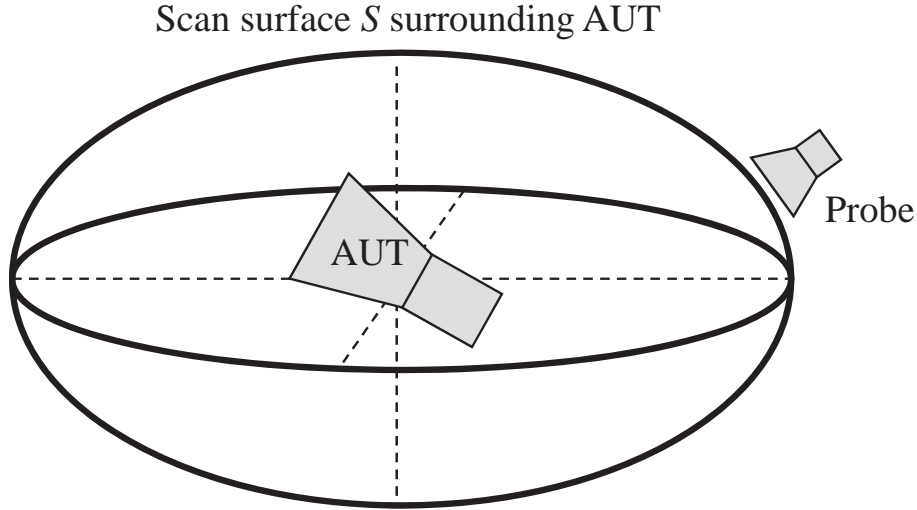
Probe

Figure 1. *The scanning geometry for the antenna under test (AUT) with reference point at the origin. The output of a probe is recorded on a surface S that contains the AUT. All points of S are assumed a couple of wavelength from the AUT so that multiple interactions can be neglected.*

298

299

300

301

Coarsest-level group on S equal
in size to the minimum sphere

Minimum sphere
containing AUT

Scan surface S
surrounding AUT
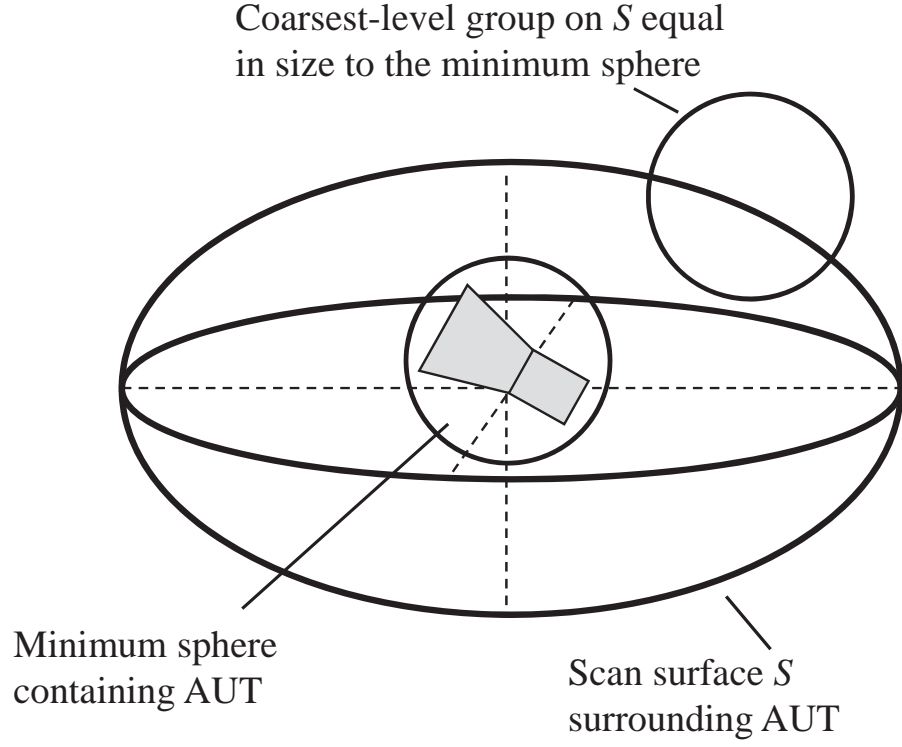
Figure 2. *The coarsest-level groups have the same diameter as the AUT. The diameter of the AUT is twice the radius R_{AUT} of the minimum sphere centered at the origin that contains the AUT. The coarsest-level groups on S are thus chosen to have diameter $D_H = 2R_{AUT}$.*
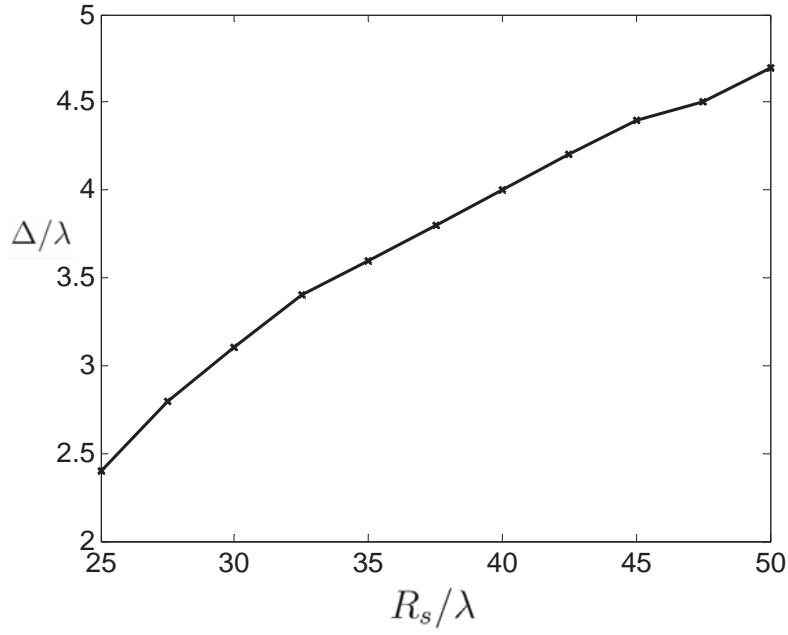
Figure 3.   *The parameter Δ of the Gaussian translation operator as a function of scan-sphere radius R_s with $R_{AUT} = 5\lambda$.*
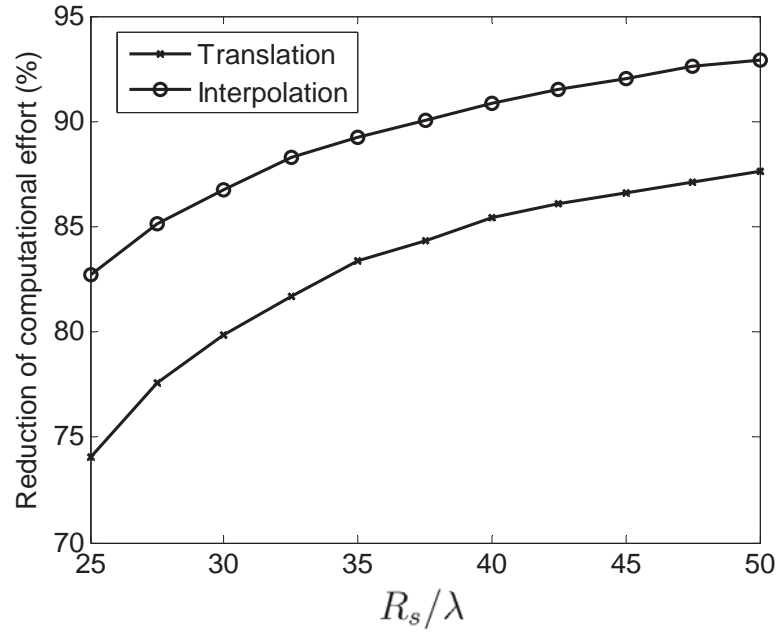
Figure 4.   *Reduction of computational effort achieved with the Gaussian translation operator during the translation and interpolation processes as functions of scan-sphere radius R_s with $R_{AUT} = 5\lambda$.*
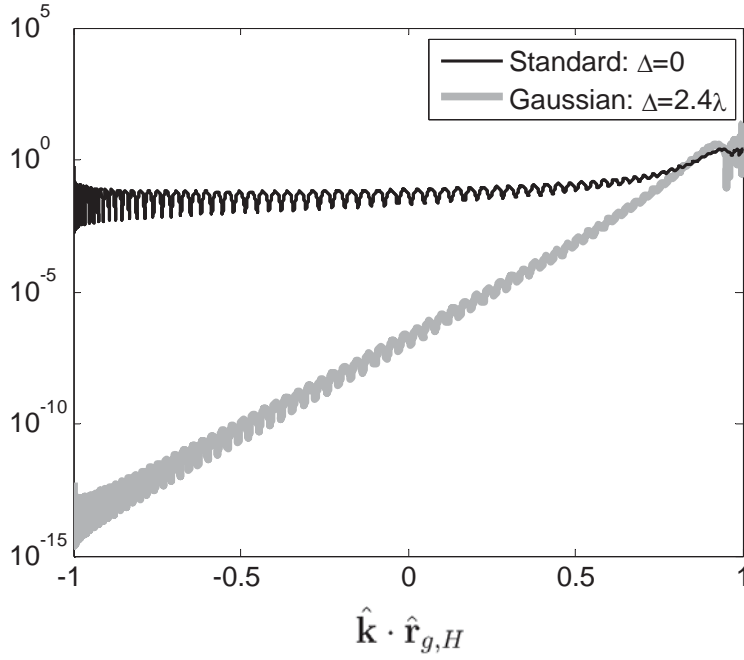
Figure 5. *The magnitude of the standard $(\Delta = 0)$ and Gaussian $(\Delta = 2.4\lambda)$ translation operators for $R_s = 25\lambda$ and $R_{AUT} = 5\lambda$. The truncation numbers for the standard and Gaussian translation operators are $N = 78$ and $N = 86$, respectively.*

4.5.2 Exact Scattering-Matrix Theory Based on Gaussian Beams

Thorkild B. Hansen*

Seknion Inc.

150 Lakeshore Road

Boxford, MA 01921, USA

February 13, 2015

Abstract

An exact Gaussian scattering-matrix theory for scalar time-harmonic fields is derived. The scattered field is expressed in terms of Gaussian beams whose weighs are determined by the Gaussian scattering matrix and the output of Gaussian receivers. The Gaussian beams used here are sometimes referred to as complex source-point beams. The scattering-matrix theory has the same structure as Kerns' plane-wave scattering matrix theory, but with directional basis fields. The Gaussian scattering matrix is determined from Waterman's T-matrix. A numerical example involving a Dirichlet sphere validates the theory.

I Introduction

A scattering problem consists of determining the scattered field from some object that is illuminated by a primary field. One popular solution method is scattering-matrix theory, which provides a way of determining the expansion coefficients of the scattered field from the expansion coefficients of the primary field. For example, in Kerns' [1] plane-wave scattering-matrix theory, the plane-wave spectrum of the scattered field is expressed in terms of the plane-wave spectrum of the

---

*thorkild.hansen@att.net.

primary field and a scattering matrix unique to the scatterer. Similarly, with Waterman's [2], [3], [4] spherical-wave scattering-matrix theory (often referred to as the T-matrix method), the spherical-wave expansion coefficients of the scattered and primary fields are related through a matrix equation.

Scattering-matrix theory has seen an increased popularity in the areas of electromagnetic, acoustic, and elastic scattering [5], [6]. In particular, in recent years the T-matrix method has been used in connection with plasmonic nanoparticles [7] [8], effective-medium theory [9], imaging [10], inverse scattering [11], coated scatterers [12], and boundary integral problems [13]. Neither the plane-wave scattering matrix nor the T-matrix employ directional basis fields and as a consequence one must in general perform "full" calculations even if the primary source and the observation regions are of limited extent.

The present paper describes an exact scattering-matrix theory that is as general as the two theories mentioned above. Moreover, it employs directional basis fields (Gaussian beams) that make it possible to reduce the computational effort for certain configurations. Deschamps [14] discovered the Gaussian beams that we use as basis fields. These beams are obtained by substituting a complex source point into the free-space Green's function in the frequency domain. The wave object thus obtained is also called a complex source-point beam and is an exact solution to the Helmholtz equation, which exhibits Gaussian behavior in the paraxial region [14], [15], [16], [17], [18], [19], [20].

Gaussian beams are suitable as basis fields in exact expansions of arbitrary acoustic and electromagnetic fields with finite source regions in both the time and frequency domains [21], [22], [23], [24], [25], [26], [27], [28], [29]. More recently, Gaussian beams have been used to develop a directional translation operator for the Fast Multipole Method as well as a new exact plane-wave theory with a directional spectrum [30], [31], [32], [33].

The present paper is organized as follows. The scattering problem under consideration is described in Section II, and the Gaussian beams are introduced in Section III. Sections IV and V explain how Gaussian beams can be used to expand scattered and primary fields. Section VI derives the Gaussian scattering-matrix formula for arbitrary scatterers, which is subsequently applied in Section VII to the Dirichlet sphere. Section VIII validates the theory through a numerical example,
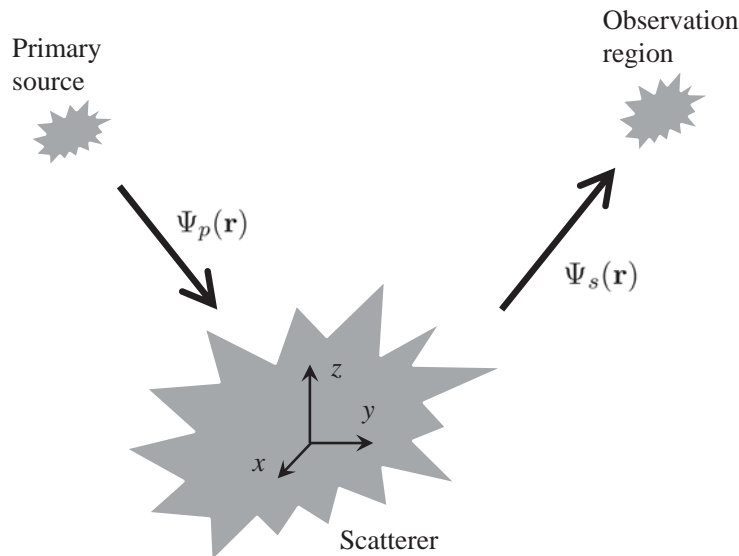
66

Figure 1: *The scattering configuration. The field $\Psi_p(\mathbf{r})$ of the primary source encounters the scatterer. The scattered field $\Psi_s(\mathbf{r})$ is observed in the observation region. The global (x, y, z) coordinate system has origin near the scatterer.*

and Section IX discusses future research topics.

II The scattering problem

Figure 1 shows the scattering problem under consideration, which involves scalar fields that satisfy the homogeneous Helmholtz equation in the source-free regions of 3D space. The primary source generates the field $\Psi_p(\mathbf{r})$ that interacts with the scatterer to produce the scattered field $\Psi_s(\mathbf{r})$. The scattered field is observed in the observation region. A minimum sphere of radius R_s centered at the origin encloses the scatterer. Both the primary source region and the observation region are assumed to be outside this sphere.

The standard rectangular coordinates are denoted by (x, y, z) with unit vectors $\hat{\mathbf{x}}$, $\hat{\mathbf{y}}$, and $\hat{\mathbf{z}}$, so that a general point in space can be expressed as $\mathbf{r} = x\hat{\mathbf{x}} + y\hat{\mathbf{y}} + z\hat{\mathbf{z}}$. The spherical coordinates (r, θ, ϕ) are related to the rectangular coordinates through $x = r\sin\theta\cos\phi$, $y = r\sin\theta\sin\phi$, and $z = r\cos\theta$ with the radial spherical unit vector given by $\hat{\mathbf{r}} = \sin\theta\cos\phi\hat{\mathbf{x}} + \sin\theta\sin\phi\hat{\mathbf{y}} + \cos\theta\hat{\mathbf{z}}$. Throughout, $e^{-i\omega t}$ time dependence with $\omega > 0$ is assumed and suppressed. The wave number is
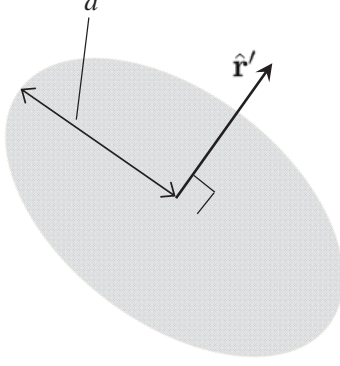
Figure 2: *The sources of the Gaussian beam in (1) reside on a disk with radius a, centered at the origin with normal $\hat{\mathbf{r}}'$.*

$k = 2\pi/\lambda = \omega/c$, with c being the wave speed and λ the wave length.

III   The Gaussian beam

The Gaussian beam of the present paper (also referred to as a complex source-point beam) was first obtained by Deschamps [14] by inserting a complex source point $\mathbf{r}' = ia\hat{\mathbf{r}}'$ with $a > 0$ into the free-space Green's function to get

$$\Psi_{GB}(\mathbf{r}) = \frac{e^{ik\sqrt{(\mathbf{r}-ia\hat{\mathbf{r}}')^2}}}{4\pi\sqrt{(\mathbf{r}-ia\hat{\mathbf{r}}')^2}} \tag{1}$$

where the distance $\sqrt{(\mathbf{r} - ia\hat{\mathbf{r}}')^2}$ is complex with the square root defined to have a non-negative real part and its branch cut placed along the negative real axis [16], [27]. For fixed $\hat{\mathbf{r}}'$ and varying $\mathbf{r}$ the branch cut manifests itself in real 3D space by a branch-cut disk of radius a, centered at the origin with normal $\hat{\mathbf{r}}'$; see Figure 2. Hence, the field Ψ_{GB} satisfies the homogeneous Helmholtz equation everywhere except on the branch-cut disk where the sources reside.

The far-field formula

$$\Psi_{GB}(\mathbf{r}) \sim \frac{e^{ikr}}{4\pi r} e^{ka\hat{\mathbf{r}}\cdot\hat{\mathbf{r}}'} \tag{2}$$

shows that for $k > 0$ and $a > 0$ the Gaussian beam radiates most strongly in the direction $\hat{\mathbf{r}}'$ and most weakly in the direction $-\hat{\mathbf{r}}'$. The name "Gaussian beam" refers to the fact that Ψ_{GB} exhibits

Gaussian behavior near the direction $\hat{\mathbf{r}}'$: let $\cos\Theta = \hat{\mathbf{r}} \cdot \hat{\mathbf{r}}'$ in (2) to get

$$\Psi_{GB}(\mathbf{r}) \sim \frac{e^{ikr}}{4\pi r} e^{ka(1-\Theta^2/2)} \tag{3}$$

when Θ is small.

We say that the Gaussian beam (1) is generated by a Gaussian transmitter whose sources reside on the disk in Figure 2. We shall also introduce the corresponding Gaussian receiver whose output equals the incident field evaluated at $ia\hat{\mathbf{r}}'$. Consider an incident plane wave $\Psi(\mathbf{r}) = e^{-ik\hat{\mathbf{r}}^i \cdot \mathbf{r}}$ propagating in the direction $-\hat{\mathbf{r}}^i$. The output due to this incident field determines the plane-wave receiving characteristic of the Gaussian receiver: $\Psi(ia\hat{\mathbf{r}}') = e^{ka\hat{\mathbf{r}}^i \cdot \hat{\mathbf{r}}'}$. Hence, the Gaussian receiver has indeed the pattern of a Gaussian beam.

We shall use both Gaussian transmitters and receivers in the following sections to obtain the Gaussian scattering-matrix theory. Next we present an exact Gaussian-beam expansion for the scattered field.

IV   The scattered field

Outside the minimum sphere for the scatterer in Figure 1, the scattered field can be expanded in terms of outgoing spherical waves as

$$\Psi_s(\mathbf{r}) = \sum_{\ell=0}^{L} \sum_{m=-\ell}^{\ell} \mathcal{A}_{\ell m} \, h_\ell^{(1)}(kr) Y_{\ell m}(\theta, \phi), \quad r > R_s \tag{4}$$

where the truncation is

$$L = kR_s + \gamma(kR_s)^{1/3}, \qquad \gamma = \frac{(-3\ln\mathcal{E})^{2/3}}{2} \tag{5}$$

with $\mathcal{E}$ being the desired relative accuracy. For example, $\gamma \simeq 6$ if $\mathcal{E} = 10^{-6}$. Moreover, $h_\ell^{(1)}$ is the spherical Hankel function of the first kind and order ℓ, and $Y_{\ell m}$ is the spherical harmonic which satisfies the orthogonality relation

$$\int d\Omega' \, Y_{\ell'm'}(\theta', \phi') Y_{\ell m}^*(\theta', \phi') = \delta_{\ell\ell'} \, \delta_{mm'} \tag{6}$$

69

where δ_{pq} is the Kronecker delta,

$$\int d\Omega' = \int_0^{2\pi} d\phi' \int_0^{\pi} d\theta' \sin\theta' \tag{7}$$

denotes the integral over the unit sphere, and $*$ denotes complex conjugation.

The spherical expansion coefficients can be expressed in terms of the field on a real sphere with radius $R > R_s$

$$\mathcal{A}_{\ell m} = \frac{1}{h_\ell^{(1)}(kR)} \int d\Omega \, \Psi_s(R\hat{\mathbf{r}}) \, Y_{\ell m}^*(\theta, \phi) \tag{8}$$

and in terms of the far-field pattern

$$\mathcal{F}_s(\theta, \phi) = \lim_{r \to \infty} r \, e^{-ikr} \Psi_s(r\hat{\mathbf{r}}) \tag{9}$$

as

$$\mathcal{A}_{\ell m} = k \, i^{n+1} \int d\Omega \, \mathcal{F}_s(\theta, \phi) \, Y_{\ell m}^*(\theta, \phi). \tag{10}$$

The scattered field also can be expressed in terms of Gaussian beams propagating in all directions away from the source region [23], [25]

$$\Psi_s(\mathbf{r}) = \int d\Omega' W_s(\hat{\mathbf{r}}') \frac{e^{ik\sqrt{(\mathbf{r}-ia_s\hat{\mathbf{r}}')^2}}}{4\pi\sqrt{(\mathbf{r}-ia_s\hat{\mathbf{r}}')^2}}, \quad r > R_s, \quad r > a_s > 0 \tag{11}$$

where

$$W_s(\hat{\mathbf{r}}') = \sum_{\ell=0}^{L} \sum_{m=-\ell}^{\ell} \frac{\mathcal{A}_{\ell m} Y_{\ell m}(\theta', \phi')}{ik \, j_\ell(ika_s)} \tag{12}$$

is a weighting function. The original sources of Ψ_s are thus replaced by sources that reside on a collection of disks centered at the origin with normals pointing in all directions. The weighting function W_s determines the "strength" of each of these transmitting disks.

V The primary field

Inside the minimum sphere, the field of the primary source can be expanded in terms of standing spherical waves as

$$\Psi_p(\mathbf{r}) = \sum_{\ell=0}^{L} \sum_{m=-\ell}^{\ell} \mathcal{B}_{\ell m} \, j_\ell(kr) Y_{\ell m}(\theta, \phi), \quad r < R_s \tag{13}$$

where j_ℓ is the spherical Bessel function of order ℓ, and $\mathcal{B}_{\ell m}$ are the spherical expansion coefficients of the primary source. The expansion coefficients $\mathcal{B}_{\ell m}$ can be expressed in terms of the primary field evaluated at imaginary points $ia_p\hat{\mathbf{r}}$ as [25]

$$\mathcal{B}_{\ell m} = \frac{1}{j_\ell(ika_p)} \int d\Omega \, \Psi_p(ia_p\hat{\mathbf{r}}) \, Y_{\ell m}^*(\theta, \phi), \quad 0 < a_p < R_s. \tag{14}$$

Since $j_\ell(ika_p)$ is non-zero for any $ka_p > 0$, the formula (14) does not degenerate at internal resonances like the standard formula for standing-wave expansion coefficients.

As discussed in Section III, $\Psi_p(ia_p\hat{\mathbf{r}})$ is the output of a receiving disk. We can combine (13) and (14) to get the field at an interior observation point $\mathbf{r}$ directly in terms of the output $\Psi_p(ia_p\hat{\mathbf{r}}')$ of the receiving disks:

$$\Psi_p(\mathbf{r}) = \int d\Omega' U(\mathbf{r}, \hat{\mathbf{r}}') \Psi_p(ia_p\hat{\mathbf{r}}'), \quad r < R_s \tag{15}$$

where

$$U(\mathbf{r}, \hat{\mathbf{r}}') = \sum_{\ell=0}^{L} \sum_{m=-\ell}^{\ell} \frac{j_\ell(kr)}{j_\ell(ika_p)} Y_{\ell m}^*(\theta', \phi') Y_{\ell m}(\theta, \phi) \tag{16}$$

is a weighting function.

A The point-source field

In a numerical example in Section VIII we shall use a point source as the primary source. If the point source is located at the point $\mathbf{r}_0$ with spherical coordinates (r_0, θ_0, ϕ_0), the expansion coefficients are

$$\mathcal{B}_{\ell m} = ik \, h_\ell^{(1)}(kr_0) \, Y_{\ell m}^*(\theta_0, \phi_0) \tag{17}$$

71

and the primary field is

$$\Psi_p(\mathbf{r}) \equiv \frac{e^{ik|\mathbf{r}-\mathbf{r}_0|}}{4\pi|\mathbf{r}-\mathbf{r}_0|} = ik \sum_{\ell=0}^{L} \sum_{m=-\ell}^{\ell} h_\ell^{(1)}(kr_0) \, Y_{\ell m}^*(\theta_0, \phi_0) \, j_\ell(kr) Y_{\ell m}(\theta, \phi), \quad r < R_s < r_0. \tag{18}$$

VI   The Gaussian scattering matrix

Waterman's T-matrix, denoted in the present paper by $T_{mm'\ell\ell'}$, determines the coefficients $\mathcal{A}_{\ell m}$ of the scattered field in terms of the coefficients $\mathcal{B}_{\ell m}$ of the primary field as [2], [3]

$$\mathcal{A}_{\ell m} = \sum_{\ell'=0}^{L} \sum_{m'=-\ell'}^{\ell'} T_{mm'\ell\ell'} \, \mathcal{B}_{\ell' m'}. \tag{19}$$

Thus, $T_{mm'\ell\ell'}$ is a spherical-wave scattering matrix that employs standing and outgoing waves. Inserting (14) and (19) into (12) gives a formula for the weighting function for the scattered field

$$W_s(\hat{\mathbf{r}}') = \sum_{\ell=0}^{L} \sum_{m=-\ell}^{\ell} \frac{Y_{\ell m}(\theta', \phi')}{ik \, j_\ell(ika_s)} \sum_{\ell'=0}^{L} \sum_{m'=-\ell'}^{\ell'} \frac{T_{mm'\ell\ell'}}{j_{\ell'}(ika_p)} \int d\Omega'' \, \Psi_p(ia_p\hat{\mathbf{r}}'') \, Y_{\ell' m'}^*(\theta'', \phi'') \tag{20}$$

which can be inserted into (11) to get

$$\Psi_s(\mathbf{r}) = \int d\Omega' \frac{e^{ik\sqrt{(\mathbf{r}-ia_s\hat{\mathbf{r}}')^2}}}{4\pi\sqrt{(\mathbf{r}-ia_s\hat{\mathbf{r}}')^2}} \int d\Omega'' \Psi_p(ia_p\hat{\mathbf{r}}'') \, Q(\hat{\mathbf{r}}', \hat{\mathbf{r}}'') \tag{21}$$

where

$$Q(\hat{\mathbf{r}}', \hat{\mathbf{r}}'') = \frac{1}{ik} \sum_{\ell=0}^{L} \sum_{m=-\ell}^{\ell} \frac{Y_{\ell m}(\theta', \phi')}{j_\ell(ika_s)} \sum_{\ell'=0}^{L} \sum_{m'=-\ell'}^{\ell'} \frac{Y_{\ell' m'}^*(\theta'', \phi'')}{j_{\ell'}(ika_p)} \, T_{mm'\ell\ell'} \tag{22}$$

is the desired Gaussian scattering matrix.

The formula (21) expresses the scattered field directly in terms of the output of Gaussian receivers pointing in all directions (that is, in terms of the incident field evaluated at imaginary points of the form $ia_p\hat{\mathbf{r}}''$, where $\hat{\mathbf{r}}''$ covers the unit sphere). The directivity of these receivers ensure that one can neglect directions $\hat{\mathbf{r}}''$ that do not point towards the primary source region. Similarly, the directivity of the transmitting Gaussian beams in the $\hat{\mathbf{r}}'$ integral ensure that one can neglect directions $\hat{\mathbf{r}}'$ that do not point towards the observation region. These properties will be demonstrated in a numerical example in Section VIII. Also, note that the Gaussian scattering

matrix contains two free parameters (the disk radii a_p and a_s) that can be used to optimize the efficiency of the scattering calculation.

Let us briefly discuss how $\Psi_p(ia_p\hat{\mathbf{r}}'')$ can be obtained through simulations or measurements. If the software used to perform simulations defines the square root to have non-negative real part and its branch cut along the negative real axis (Matlab's square root is defined this way), one simply sets the observation point equal to the imaginary point $ia_p\hat{\mathbf{r}}''$. No further work is needed. If the software defines the square root differently, one must write a new square-root function defined as described above.

If the primary field is measured on a sphere centered on the primary source, outgoing spherical expansion coefficients are known. One can then compute $\Psi_p(ia_p\hat{\mathbf{r}}'')$ directly from the formula (11) applied to the primary source. Also, if the primary source is far from the scatterer, the incident field in the region of the scatterer is a single plane wave for which $\Psi_p(ia_p\hat{\mathbf{r}}'')$ is given at the end of Section III.

Consider next a simple physical disk scatterer on which certain boundary conditions hold. This scatterer *cannot* be modeled by a Gaussian receiver and transmitter that reside in the same plane as the physical disk. Such a model would violate the law of reflection since the scattered field would always attain its maximum value in the direction normal to the physical disk, regardless of the direction of the primary source. Indeed, the scattering matrix (22) couples a receiving disk with normal $\hat{\mathbf{r}}''$ to a transmitting disk with normal $\hat{\mathbf{r}}'$, where $\hat{\mathbf{r}}''$ is not necessarily equal to $\hat{\mathbf{r}}'$.

The Gaussian scattering-matrix theory can be generalized to antennas with input and output ports, as has been done for the scattering-matrix theories that employ plane waves [1], cylindrical waves [34], and spherical waves [35]. This generalization could be achieved by combining the Gaussian antenna-antenna transmission formulas in [25] and [29] with the Gaussian scattering matrix.

Let us briefly compare the Gaussian scattering-matrix formulation to the plane-wave scattering-matrix formulation (one-sided) in which the scattered field is written as [1, pp.57-61]

$$\Psi_s(\mathbf{r}) = \int d\mathbf{K}' \, e^{i\mathbf{k}' \cdot \mathbf{r}} \int d\mathbf{K}'' \, \mathcal{T}_p(\mathbf{K}'') \, S(\mathbf{K}', \mathbf{K}'') \tag{23}$$

where $S(\mathbf{K}', \mathbf{K}'')$ is the plane-wave scattering matrix, and $\mathcal{T}_p(\mathbf{K}'')$ is the plane-wave spectrum of the primary field. Moreover, $\mathbf{K}'$ is the transverse part of the plane-wave propagation vector $\mathbf{k}'$ for the scattered field. Similarly, $\mathbf{K}''$ is the transverse part of the plane-wave propagation vector $\mathbf{k}''$ for the primary field. The plane-wave spectrum of the primary field $\mathcal{T}_p(\mathbf{K}'')$ can be thought of as the output of a plane-wave receiver that picks out a single plane-wave component of the primary field.

It is challenging to use the plane-wave expansion (23) in numerical computations that require a preselected accuracy. First, the integrand of the $\mathbf{K}'$ has an integrable singularity at $|\mathbf{K}'| = k$ that in many situations necessitates a change of variables [36, ch.3]. Second, in general the integrands do not decay until the evanescent regions $|\mathbf{K}'| > k$ and $|\mathbf{K}''| > k$ are reached. In some situations one must integrate all the way into the evanescent regions to avoid strong end-point contributions [33]. Nevertheless, there are some favorable situations where the integrals in (23) can be truncated to include only small regions in the propagating domains without introducing significant errors [37].

The beam expansion (21) has the same form as the plane-wave expansion (23), with the Gaussian transmitter field $\exp(ik\sqrt{(\mathbf{r} - ia_s\hat{\mathbf{r}}')^2})/(4\pi\sqrt{(\mathbf{r} - ia_s\hat{\mathbf{r}}')^2})$ replacing the plane wave $e^{i\mathbf{k}'\cdot\mathbf{r}}$, and the Gaussian receiver output $\Psi_p(ia_p\hat{\mathbf{r}}'')$ replacing the plane-wave spectrum $\mathcal{T}_p(\mathbf{K}'')$. However, neither $e^{i\mathbf{k}'\cdot\mathbf{r}}$ nor $\mathcal{T}_p(\mathbf{K}'')$ are directional, and the integrals in (23) are numerically challenging as discussed above. The T-matrix is also not directional because all spherical expansion coefficients are needed to compute the field in any direction. However, the T-matrix method is numerically much more well behaved than then plane-wave approach (23).

VII The Dirichlet sphere

Consider a sphere centered at the origin with radius R_s on which the Dirichlet boundary condition holds: $\Psi_p(R_s\hat{\mathbf{r}}) + \Psi_s(R_s\hat{\mathbf{r}}) = 0$. We find readily that the T-matrix elements are zero unless $\ell = \ell'$ and $m = m'$ with

$$T_{m\ell} = -\frac{j_\ell(kR_s)}{h_\ell^{(1)}(kR_s)} \tag{24}$$

so that the Gaussian scattering matrix is

$$Q(\hat{\mathbf{r}}', \hat{\mathbf{r}}'') = -\frac{1}{4\pi ik} \sum_{\ell=0}^{L} \frac{(2\ell + 1)\, j_\ell(kR_s)\, P_\ell(\hat{\mathbf{r}}' \cdot \hat{\mathbf{r}}'')}{h_\ell^{(1)}(kR_s)\, j_\ell(ika_s)\, j_\ell(ika_p)} \tag{25}$$
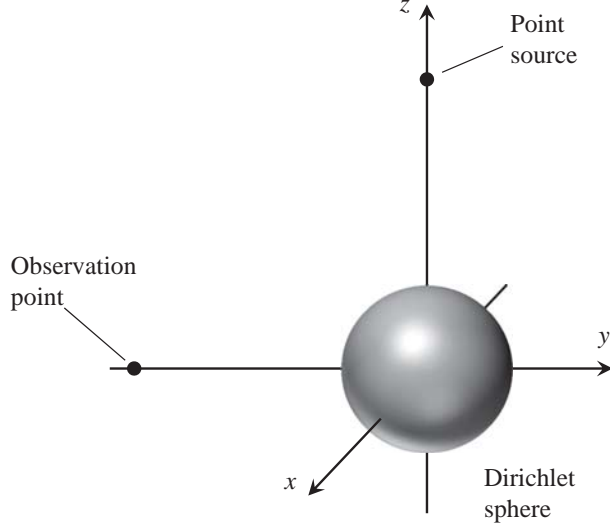
Figure 3: *Dirichlet sphere with radius $R_s = 5\lambda$ illuminated by a real point source on the z axis at $z = 15\lambda$. The observation point is on the y axis at $y = -15\lambda$. Both transmitting and receiving disks have radius $a_s = a_p = 14\lambda$.*

where we have used [38, eq.(14.30.9)]

$$\frac{2\ell + 1}{4\pi} P_\ell(\hat{\mathbf{r}}' \cdot \hat{\mathbf{r}}'') = \sum_{m=-\ell}^{\ell} Y_{\ell m}(\theta', \phi') Y_{\ell m}^*(\theta'', \phi'') \tag{26}$$

with P_ℓ being the Legendre polynomial of order ℓ. As expected, the Gaussian scattering matrix for this sphere depends only on $\hat{\mathbf{r}}'$ and $\hat{\mathbf{r}}''$ through the dot product $\hat{\mathbf{r}}' \cdot \hat{\mathbf{r}}''$. Hence, like the T-matrix, the Gaussian scattering matrix simplifies significantly when the scatterer is a sphere.

For use in the numerical verification of the theory, we note that the scattered field due to a point source at $\mathbf{r}_0$ is given by the Mie series

$$\Psi_s(\mathbf{r}) = -ik \sum_{\ell=0}^{L} \sum_{m=-\ell}^{\ell} \frac{j_\ell(kR_s) h_\ell^{(1)}(kr_0)}{h_\ell^{(1)}(kR_s)} Y_{\ell m}^*(\theta_0, \phi_0) h_\ell^{(1)}(kr) Y_{\ell m}(\theta, \phi), \quad r > R_s. \tag{27}$$

It is easy to verify that the primary point-source field in (18) and the Mie scattered field in (27) indeed produce a zero total field on the sphere $r = R_s$.
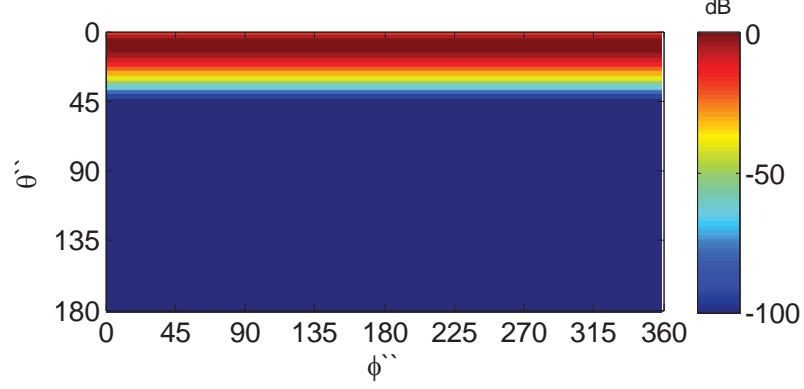
75

Figure 4: *Normalized magnitude in dB of the function $I_3(\mathbf{r}, \hat{\mathbf{r}}'')$ for the scattering configuration in Figure 3. The receiving disks with normals pointing towards the point source at $\theta'' = 0$ contribute most strongly to the integral over $\hat{\mathbf{r}}''$.*

VIII   Numerical example

To validate the Gaussian scattering-matrix theory, consider the Dirichlet sphere illuminated by a real point source on the z axis as shown in Figure 3. The sphere radius is $R_s = 5\lambda$ and the point source is at $z = 15\lambda$. The observation point is on the negative y axis at $y = -15\lambda$. The radii of the transmitting and receiving disks are $a_s = a_p = 14\lambda$.
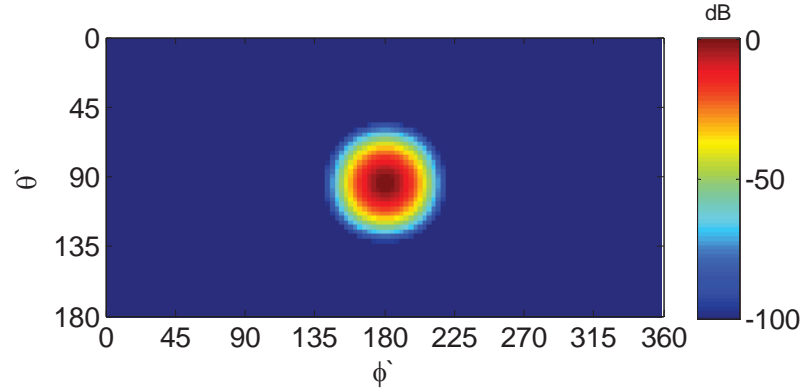
Figure 5: *Normalized magnitude in dB of the function $I_1(\mathbf{r}, \hat{\mathbf{r}}')$ for the scattering configuration in Figure 3. The transmitting disks with normals pointing towards the observation point at $(\theta, \phi) = (90°, 180°)$ contribute most strongly to the integral over $\hat{\mathbf{r}}'$.*

76

To investigate the possibility of omitting portions of the $\hat{\mathbf{r}}'$ and $\hat{\mathbf{r}}''$ integrations, we write the Gaussian-beam representation (21) as

$$\Psi_s(\mathbf{r}) = \int d\Omega' I_1(\mathbf{r}, \hat{\mathbf{r}}') \tag{28}$$

where

$$I_1(\mathbf{r}, \hat{\mathbf{r}}') = \frac{e^{ik\sqrt{(\mathbf{r}-ia_s\hat{\mathbf{r}}')^2}}}{4\pi\sqrt{(\mathbf{r}-ia_s\hat{\mathbf{r}}')^2}} \int d\Omega'' I_2(\mathbf{r}, \hat{\mathbf{r}}', \hat{\mathbf{r}}'') \tag{29}$$

with

$$I_2(\mathbf{r}, \hat{\mathbf{r}}', \hat{\mathbf{r}}'') = \Psi_p(ia_p\hat{\mathbf{r}}'')\, Q(\hat{\mathbf{r}}', \hat{\mathbf{r}}''). \tag{30}$$

To investigate the integrand in the $\mathbf{r}''$ integral, Figure 4 shows the normalized magnitude of

$$I_3(\mathbf{r}, \hat{\mathbf{r}}'') = \max_{\hat{\mathbf{r}}'}(|I_2(\mathbf{r}, \hat{\mathbf{r}}', \hat{\mathbf{r}}'')|). \tag{31}$$

We see that the receiving disks with normals pointing towards the point source at $\theta'' = 0$ contribute most strongly to the integral over $\hat{\mathbf{r}}''$. Indeed, at $\theta'' = 45°$ the value of $I_3(\mathbf{r}, \hat{\mathbf{r}}'')$ is more than $100\,\mathrm{dB}$ below its peak at $\theta'' = 0$.

The plot in Figure 5 of the normalized magnitude of $I_1(\mathbf{r}, \hat{\mathbf{r}}')$ shows that the transmitting disks with normals pointing towards the observation point at $(\theta, \phi) = (90°, 180°)$ contribute most strongly to the integral over $\hat{\mathbf{r}}'$. The magnitude of $I_1(\mathbf{r}, \hat{\mathbf{r}}')$ is more than $100\,\mathrm{dB}$ below its peak when the $\hat{\mathbf{r}}'$ is roughly $30°$ away from the peak direction $(\theta', \phi') = (90°, 180°)$.

Using $L = 60$ and discretizing the $\hat{\mathbf{r}}'$ and $\hat{\mathbf{r}}''$ integrals with $\Delta\theta = \Delta\phi = 2.9752°$, the relative difference $|\Psi_{Mie} - \Psi_{Gauss}|/|\Psi_{Mie}|$ between the Mie series (27) and the Gaussian scattering-matrix solution (21) is $1.1 \cdot 10^{-7}$. We have thus numerically validated the new Gaussian scattering-matrix theory and demonstrated the directionality of the integrands of both the $\hat{\mathbf{r}}'$ and $\hat{\mathbf{r}}''$ integrals in (21).

IX   Conclusions and future work

We presented and validted an exact Gaussian-beam scattering matrix theory that is as general as Kerns' plane-wave scattering matrix theory and Waterman's T-matrix theory. A number of possible

research topics emerge from the material presented above.

The Gaussian transmitters and receivers contained in the scattering-matrix theory ensure that the integrands of the expression for the scattered field are significantly non-zero only in certain regions whose location and size depend on the scattering geometry. The sharpness of the integrands depends on the two free parameters a_s and a_p that determine the radii of the transmitting and receiving disk. Since the scattering matrix also depends on a_s and a_p, a careful analysis is required to determine the optimal values of a_s and a_p for a given scattering configuration.

The scattering-matrix expression (21) for the scattered field could be combined with a Gaussian-beam expansion of the primary field. By interchanging the integration over $\hat{\mathbf{r}}''$ in (21) with the integration over the beams of the primary source, one would obtain an alternative field expression that would involve the output of a Gaussian receiver due to the field of a Gaussian transmitter. Such expressions can be extremely directional as has been observed in the transmission formulas of [25] and [29].

Similarly, if the scattered field is received by an antenna, one can employ a Gaussian receiver representation that determines the antenna output. Now the integration over Gaussian receivers can be interchanged with the integration over $\hat{\mathbf{r}}'$ in (21). One would thereby achieve an alternative expression for the antenna output that would involve the output of a Gaussian receiver due to the field of a Gaussian transmitter.

A simple three-component model for a radar system could be obtained by letting the transmitter be a single Gaussian transmitter, the target be modeled by a Gaussian scattering matrix, and the receiver be a single Gaussian receiver. Such a model would take into account the directivity of all three components of the system. A time-domain version of this radar system was suggested in [39]. However, [39] did not use a scattering matrix.

The Gaussian scattering-matrix theory is exact for arbitrary scatterers. However, it may be of interest to derive approximate scattering matrices for large scatterers based on physical optics or other high-frequency approximations. It may be possible to express the Gaussian scattering matrix directly as an integral over the surface of the scatterer.

Asymptotic expressions for the scattrered field in certain parameter regimes could be obtained from (21) using existing asymptotic integration techniques. Such expressions could likely be fine-

tuned by selecting the free parameters a_s and a_p appropriately.

The scalar scattering matrix of the present paper can be generalized to electromagnetic fields in a straightforward manner. Also, one can generalize the scatterer to an antenna that has an input and an output port. Thus one obtains a Gaussian antenna scattering-matrix theory analogous to the standard theories in [1], [34], and [35].

The 3rd Generation Partnership Project (3GPP) is a standards body created to ensure that the various components of wireless systems (cellular networks, mobile phones, etc.) operate according to the same standard. Some of the channel models developed in 3GPP specify antennas with Gaussian pattern near the main lobe [40]. These antenna models could easily be incorporated into the Gaussian scattering-matrix theory to obtain a convenient tool for simulating wireless systems.

The formula (22) expresses the Gaussian scattering matrix $Q(\hat{\mathbf{r}}', \hat{\mathbf{r}}'')$ in terms of Waterman's T-matrix $T_{mm'\ell\ell'}$. It would be interesting, for a given scatterer, to derive an expression for $Q(\hat{\mathbf{r}}', \hat{\mathbf{r}}'')$ from first principles.

The formula (22) relates the Gaussian scattering matrix to Waterman's T-matrix. A similar formula (perhaps simpler) could likely be derived that relates the Gaussian scattering matrix to the plane-wave scattering matrix $S(\mathbf{K}', \mathbf{K}'')$ in (23).

The Gaussian scattering-matrix theory was developed in this paper for time-harmonic fields. Conversion to the time domain using analytic-signal fields would provide a method for analyzing pulsed scattering problems.

Acknowledgments

References

[1] D.M. Kerns, *Plane-Wave Scattering-Matrix Theory of Antennas and Antenna-Antenna Interactions,* NBS Monograph 162, Washington, DC: U.S. Government Printing Office, 1981.

[2] P.C. Waterman, "Matrix formulation of electromagnetic scattering," *Proceedings of the IEEE,* Vol. 53, pp. 805-812, August 1965.

[3] P.C. Waterman, "Symmetry, unitarity, and geometry in electromagnetic scattering," *Phys. Rev. D*, Vol. 3, pp. 825-839, February 1971.

[4] P.C. Waterman, "T-matrix methods in acoustic scattering," *J. Acoust. Soc. Am.*, Vol. 125, pp. 42-51, January 2009.

[5] V.V. Varadan and V.K. Varadan, "Low-frequency expansions for acoustic wave scattering using Watermans T-matrix method," *J. Acoust. Soc. Am.*, Vol. 66, pp. 586-589, August 1979.

[6] M.I. Mishchenko, L.D. Travis, D.W. Mackowski, "T-matrix method and its applications to electromagnetic scattering by particles: A current perspective," *Journal of Quantitative Spectroscopy Radiative Transfer*, Vol. 111, pp. 1700-1703, 2010.

[7] N.G. Khlebtsov, L.A. Dykman, "Optical properties and biomedical applications of plasmonic nanoparticles," *Journal of Quantitative Spectroscopy Radiative Transfer*, Vol. 111, pp. 1-35, 2010.

[8] N.G. Khlebtsov, "T-matrix method in plasmonics: An overview," *Journal of Quantitative Spectroscopy and Radiative Transfer,* Vol. 123, pp. 184-217, 2013.

[9] N.C. Kothari, "Effective-medium theory of a nonlinear composite medium using the T-matrix approach: Exact results for spherical grains," *Phys. Rev. A,* Vol. 41, No. 8, pp. 4486-4492, April 1990.

[10] X. Ye, R. Song, X. Chen, "Application of T-matrix method in solving mixed boundary separable obstacle problem," *Opt. Express,* Vol. 22, No. 13, pp. 16273-81, June 2014.

[11] H.W. Levinson and V.A. Markel, "Solution of the inverse scattering problem by T-matrix completion," arXiv:1401.3319, 14 January 2014.

[12] A. Quirantes, "A T-matrix method and computer code for randomly oriented, axially symmetric coated scatterers," *Journal of Quantitative Spectroscopy Radiative Transfer*, Vol. 92, pp. 373-381, 2005.

[13] P.A. Martin, "On connections between boundary integral equations and T-matrix methods," *Engineering Analysis with Boundary Elements*, Vol. 27, pp. 771-777, 2003.

[14] G.A. Deschamps, "Gaussian beam as a bundle of complex rays," *Electron. Lett.*, Vol. 7, pp. 684-685, 1971.

[15] J.B. Keller and W. Streifer, "Complex rays with an application to gaussian beam," *J. Opt. Soc. Amer.,* Vol. 61, pp. 40-43, 1971.

[16] L.B. Felsen, "Complex-point-source solutions of the field equations and their relation to the propagation and scattering of Gaussian beams", *Symp. Math. Instituta di alta Matetmatica,* Vol. 18, pp. 39-56, 1976.

[17] M. Couture and P.A. Belanger, "From Gaussian beam to complex-source-point spherical wave", *Phys. Rev. A*, Vol. 24, pp. 355-359, 1981.

[18] L.B. Felsen, "Geometrical theory of diffraction, evanescent waves and complex rays," *Geophys. J. R. Astron. Soc.*, Vol. 79, pp. 77-88, 1982.

[19] E. Heyman, V. Lomakin, and G. Kaiser, "Physical source realization of complex source pulsed beams" *J. Acoust. Soc. Am.*, Vol. 107, No. 4, pp. 1880-1891, 2000.

[20] G. Kaiser, "Physical wavelets and their sources: Real physics in complex spacetime," *Top. Rev. J. Phys. A*, Vol. 36, R29R338, 2003, http://arxiv.org/abs/math-ph/0303027

[21] A.N. Norris, "Complex point-source representation of real point sources and the Gaussian beam summation method," *J. Opt. Soc. Am.,* Vol. 3, No. 12, pp. 2005-2010, Dec. 1986.

[22] E. Heyman, "Complex source pulsed beam representation of transient radiation," *Wave Motion*, Vol. 11, pp. 337-349, 1989.

[23] A.N. Norris and T.B. Hansen, "Exact complex source representations of time-harmonic radiation," *Wave Motion*, Vol. 25, pp. 127-141, 1997.

[24] T.B. Hansen and A.N. Norris, "Exact complex source representations of transient radiation," *Wave Motion*, Vol. 26, pp. 101-115, 1997.

[25] T.B. Hansen, "Efficient field computation using Gaussian beams for both transmission and reception," *Wave Motion*, Vol. 48, pp. 243258, April 2011.

[26] K. Tap, P. H. Pathak and R. J. Burkholder, "Exact complex source point beam expansions for electromagnetic fields," *IEEE Trans. Antennas Propagat.*, Vol. 59, pp. 3379-3390, September 2011.

[27] T.B. Hansen and G. Kaiser, "Generalized Huygens principle with pulsed-beam wavelets," *Journal of Physics A: Mathematical and Theoretical*, Vol. 42, No. 47, 27 November 2009, paper # 475403.

[28] T.B. Hansen and G. Kaiser, "Huygens' principle for complex spheres," *IEEE Trans. Antennas Propagat.*, Vol. 59, pp. 3835-3847, October 2011.

[29] T.B. Hansen, "Exact Gaussian-beam theory for outgoing and standing spherical waves: Application to transmitting and receiving antennas," *IEEE Trans. Antennas Propagat.*, Vol. 60, pp. 1291-1302 , March 2012.

[30] T.B. Hansen, "Translation operator based on Gaussian beams for the fast multipole method in two dimensions," *Wave Motion*, Vol. 50, pp. 793-808, June 2013.

[31] T.B. Hansen, "Translation operator based on Gaussian beams for the fast multipole method in three dimensions," *Wave Motion*, Vol. 50, pp. 940-954, July 2013.

[32] T.B. Hansen, "Numerical properties of a Gaussian translation operator for the 2D FMM," *IEEE Trans. Antennas Propagat.*, Vol. 62, pp. 3119-3129, June 2014.

[33] T.B. Hansen, "Exact plane-wave expansion with directional spectrum: Application to transmitting and receiving antennas," *IEEE Trans. Antennas Propagat.*, Vol. 62, pp. 4187-4198, August 2014.

[34] A.D. Yaghjian, "Near-field antenna measurements on a cylindrical surface: A source scattering-matrix formulation," Nat. Bur. Stand. Tech. Note 696, Boulder CO, (Revised), September 1977.

[35] J.E. Hansen, ed., J. Hald, F. Jensen, and F.H. Larsen, *Spherical Near-Field Antenna Measurements,* London: Peter Peregrinus, 1988.

[36] T.B. Hansen and A.D. Yaghjian, *Plane-Wave Theory of Time-Domain Fields,* New York: IEEE Press 1999.

[37] A.D. Yaghjian, "Efficient computation of antenna coupling and fields within the near-field region," *IEEE Trans. Antennas Propagat.,* Vol. 30, pp. 113-128, January 1982.

[38] F.W.J Olver, D.W. Lozier, R.F. Boisvert, and C.W. Clark, *NIST Handbook of Mathematical Functions,* New York: Cambridge University Press, 2010.

[39] G. Kaiser, "Short-pulse radar via electromagnetic wavelets," in C.E. Baum, L. Carin and A.P. Stone, eds., *Ultra-Wideband, Short-Pulse Electromagnetics 3,* New York: Plenum Press, 1997.

[40] 3GPP Technical Specification Group Radio Access Network, "Spatial channel model for Multiple Input Multiple Output (MIMO) simulations," Release 8, 3GPP TR 25.996 V8.0.0, 2008.

List of Figures

Figure 1: *The scattering configuration. The field $\Psi_p(\mathbf{r})$ of the primary source encounters the scatterer. The scattered field $\Psi_s(\mathbf{r})$ is observed in the observation region. The global (x, y, z) coordinate system has origin near the scatterer.*

Figure 2: *The sources of the Gaussian beam in (1) reside on a disk with radius a, centered at the origin with normal $\hat{\mathbf{r}}'$.*

Figure 3: *Dirichlet sphere with radius $R_s = 5\lambda$ illuminated by a real point source on the z axis at $z = 15\lambda$. The observation point is on the y axis at $y = -15\lambda$. Both transmitting and receiving*

disks have radius $a_s = a_p = 14\lambda$.

Figure 4: *Normalized magnitude in dB of the function $I_3(\mathbf{r}, \hat{\mathbf{r}}'')$ for the scattering configuration in Figure 3. The receiving disks with normals pointing towards the point source at $\theta'' = 0$ contribute most strongly to the integral over $\hat{\mathbf{r}}''$.*

Figure 5: *Normalized magnitude in dB of the function $I_1(\mathbf{r}, \hat{\mathbf{r}}')$ for the scattering configuration in Figure 3. The transmitting disks with normals pointing towards the observation point at $(\theta, \phi) = (90°, 180°)$ contribute most strongly to the integral over $\hat{\mathbf{r}}'$.*

4.5.3   Array realization of complex-source beam

Thorkild B. Hansen

Seknion Inc.
150 Lakeshore Road
Boxford, MA 01921
USA
thorkild.hansen@att.net

Abstract

An array is constructed to radiate the far-field pattern of a single complex point source. For any nonzero error tolerance, the physical dimension of the array is smaller (sometimes much smaller) than the diameter of the branch-cut disk of the complex point source. The inverse source problem is formulated for non-resonant arrays with reactive zones that do not extend significantly beyond the physical dimensions of the array. Both time-harmonic and pulsed beams are considered. In numerical examples, each array element consists of real point sources in an end-fire configuration.

Keywords: Complex point source, Far-field pattern, Array realization, Non-resonant array

1. Introduction

Complex-source beams are exact solutions to the wave equation that were first introduced in the frequency domain by Deschamps [1] and subsequently in the time domain by Heyman and Felsen [2], [3]. These beams are used in both acoustic and electromagnetic wave theories and are often referred to as Gaussian beams in the frequency domain and as pulsed-beam wavelets or complex-source pulsed beams in the time domain.

Complex-source beams are useful for providing solutions to scattering and propagation problems in complex configurations [4], [5], [6], [7] [8], [9], [10], [11], [12], [13], [14], [15]. They are also suitable as basis functions in exact expansions of arbitrary acoustic and electromagnetic fields with finite source regions in both the time and frequency domains [16], [3], [17], [18], [19], [20], [21], [22], [23]. Recently, complex sources were employed to obtain new exact plane-wave expansions that led to directional translation operators for the fast multipole method [24], [25], [26], [27].

The paper [28] lists a number of uses for complex-source beams: (i) high-resolution probing of the propagation environment, (ii) selectively excite local scattering and diffraction phenomena, (iii) benchmark solutions for scattering of collimated wave packets by canonical configurations, (iv) propagation in inhomogeneous, dispersive, and random media, (v) wave-based data processing and local inverse scattering. Hence, complex-source beams have many properties that make it worthwhile to develop physically realizable source representations. Indeed, several papers have been devoted to obtaining volume and surface sources that

radiate complex-source beams [28], [29], [30], [31], [32].

The present paper investigates the inverse source problem for the complex-source beam as an array optimization problem. We determine excitation coefficients of array elements that each have a typical pattern of a small radiator with sidelobes. For convenience we assume that the array elements are located on a sphere, but the method used in the present paper works for any surface. By extending a recently-developed 2D theorem on the spatial bandwidth of complex-source beams [24], we show that for any nonzero error tolerance, the physical dimension of the array is smaller than the diameter of the branch-cut disk of the complex point source.

The paper is organized as follows. In Section 2 we present Green's function and spherical-wave expressions for arbitrary fields generated by source of finite extent. Also, Section 2 shows the proper truncation of the spherical-wave expansion for non-resonant sources. In Section 3 we introduce the complex-source beam and determine the proper truncation of the spherical-wave expansion of its far-field pattern. Section 3 also determines the smallest possible source region required to exactly reproduce the far-field pattern of a complex-source beam. Section 4 presents the array realizations of the complex-source beam and includes numerical examples. Sections 2, 3, and 4 all deal with frequency-domain fields. Section 5 shows array realizations of complex-source pulsed beams and Section 6 contains conclusions.

The standard rectangular coordinates are denoted by (x, y, z) with unit vectors $\hat{\mathbf{x}}$, $\hat{\mathbf{y}}$, and $\hat{\mathbf{z}}$, so that a general point in space can be expressed as $\mathbf{r} = x\hat{\mathbf{x}} + y\hat{\mathbf{y}} + z\hat{\mathbf{z}}$. The spherical coordinates (r, θ, ϕ) are related to the rectangular coordinates through $x = r\sin\theta\cos\phi$, $y = r\sin\theta\sin\phi$, and $z = r\cos\theta$ with the radial spherical unit vector given by $\hat{\mathbf{r}} = \sin\theta\cos\phi\hat{\mathbf{x}} + \sin\theta\sin\phi\hat{\mathbf{y}} + \cos\theta\hat{\mathbf{z}}$. We also make extensive use of the unit vector $\hat{\mathbf{r}}'$, which is simply $\hat{\mathbf{r}}$ evaluated at (θ', ϕ'). Throughout Sections 2, 3, and 4, we assume and supress $e^{-i\omega t}$ time dependence with $\omega > 0$. The wave number is $k = 2\pi/\lambda = \omega/c$, with c being the wave speed and λ the wave length.

2. Properties of non-resonant sources
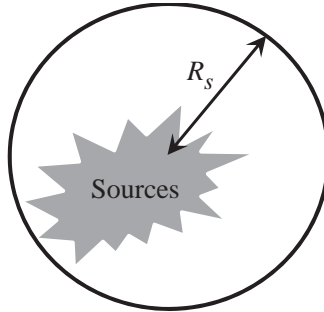
Figure 1: *The source function $Q(\mathbf{r}')$ resides inside a sphere centered at the origin with radius R_s. This figure depicts a configuration where the actual source region is not centered on the origin.*

This section is devoted to describing the far field that can be radiated by non-resonant sources of a given physical extent. A wave field $\Psi(\mathbf{r})$ that satisfies Helmholtz equation with constant wave speed can be expressed in terms of its source function $Q(\mathbf{r}')$ and the scalar free-space Green's function

$$G(\mathbf{r}, \mathbf{r}') = \frac{e^{ik\sqrt{(\mathbf{r}-\mathbf{r}')^2}}}{4\pi\sqrt{(\mathbf{r}-\mathbf{r}')^2}} \tag{1}$$

as

$$\Psi(\mathbf{r}) = \int dV' \, G(\mathbf{r}, \mathbf{r}') \, Q(\mathbf{r}') \tag{2}$$

where the integral extends over the source region, which is assumed of finite extent and located inside the sphere $r = R_s$, as shown in Figure 1. In other words, $Q(\mathbf{r}') = 0$ for $r' > R_s$. The distance between the integration point $\mathbf{r}'$ and the observation point $\mathbf{r}$ is written as $\sqrt{(\mathbf{r}-\mathbf{r}')^2}$ since this form of the distance function makes generalization to complex source points straightforward.

When $r \gg r'$, $\sqrt{(\mathbf{r}-\mathbf{r}')^2} \sim r - \hat{\mathbf{r}} \cdot \mathbf{r}'$ so that

$$G(\mathbf{r}, \mathbf{r}') \sim \frac{e^{-ik\hat{\mathbf{r}}\cdot\mathbf{r}'} \, e^{ikr}}{4\pi r}, \quad r \to \infty \tag{3}$$

which shows that the far field can be expressed as

$$\Psi(\mathbf{r}) \sim \mathcal{F}(\hat{\mathbf{r}}) \frac{e^{ikr}}{r}, \quad r \to \infty \tag{4}$$

where

$$\mathcal{F}(\hat{\mathbf{r}}) = \frac{1}{4\pi} \int dV' \, Q(\mathbf{r}') \, e^{-ik\hat{\mathbf{r}}\cdot\mathbf{r}'} \tag{5}$$

is the far-field pattern, which can also be expressed in terms of the field as

$$\mathcal{F}(\hat{\mathbf{r}}) = \lim_{r\to\infty} r \, e^{-ikr} \Psi(r\hat{\mathbf{r}}). \tag{6}$$

The wave field $\Psi(\mathbf{r})$ has the spherical-harmonics expansion

$$\Psi(\mathbf{r}) = \sum_{n=0}^{N_Q} \sum_{m=-n}^{n} \mathcal{A}_{nm} \, h_n^{(1)}(kr) Y_{nm}(\theta, \phi), \quad r > R_s + \lambda \tag{7}$$

where N_Q is a truncation limit that will be discussed below. The region of validity of (7) is expressed as $r > R_s + \lambda$ to ensure that the observation point is outside the reactive zone of the source. Also, Y_{nm} is the spherical harmonic, j_n is the spherical Bessel function, and $h_n^{(1)}$ is the spherical Hankel function of the first kind. The spherical harmonic satisfies the orthogonality relation

$$\int d\Omega' \, Y_{n'm'}(\theta', \phi') Y_{nm}^*(\theta', \phi') = \delta_{nn'} \, \delta_{mm'} \tag{8}$$

where δ_{pq} is the Kronecker delta and

$$\int d\Omega' = \int_0^{2\pi} d\phi' \int_0^{\pi} d\theta' \sin\theta' \tag{9}$$

is the integral over the unit sphere. Moreover, $*$ denotes complex conjugation. Employing the large-argument approximation of the spherical Hankel function

$$h_n^{(1)}(Z) \sim i^{-n-1}\frac{e^{iZ}}{Z}, \quad Z \to \infty \tag{10}$$

with (6) shows that the far-field pattern has the spherical-harmonics expansion

$$\mathcal{F}(\theta, \phi) = \frac{1}{k}\sum_{n=0}^{N_Q}\sum_{m=-n}^{n} \mathcal{A}_{nm}\, i^{-n-1}\, Y_{nm}(\theta, \phi). \tag{11}$$

Employing the orthogonality relation (8), we see that the spherical expansion coefficients can be expressed in terms of the field on a sphere with radius R as

$$\mathcal{A}_{nm} = \frac{1}{h_n^{(1)}(kR)}\int d\Omega\, \Psi(R\hat{\mathbf{r}})\, Y_{nm}^*(\theta, \phi), \quad R > R_s + \lambda \tag{12}$$

and in terms of the far-field pattern as

$$\mathcal{A}_{nm} = k\, i^{n+1}\int d\Omega\, \mathcal{F}(\theta, \phi)\, Y_{nm}^*(\theta, \phi). \tag{13}$$

We shall now discuss the standard truncation formula that determines the truncation limit N_Q that ensures a given relative error $\mathcal{E}$ for the expansion of the far-field pattern of a non-resonant source. This truncation formula is derived for a single real point source at $\mathbf{r}' = R_s\hat{\mathbf{z}}$ for which (11) is

$$\frac{e^{-ikR_s\cos\theta}}{4\pi} = \frac{1}{4\pi}\sum_{n=0}^{\infty}(2n+1)\, i^{-n}j_n(kR_s)\, P_n(\cos\theta) \tag{14}$$

where $P_n(Z)$ is the Legendre polynomial of order n. For a prescribed relative error $\mathcal{E}$, the standard truncation number N_Q is the smallest positive integer for which

$$\max_{\theta}\left|e^{-ikR_s\cos\theta} - \sum_{n=0}^{N_Q}(2n+1)\, i^{-n}j_n(kR_s)\, P_n(\cos\theta)\right| < \mathcal{E} \tag{15}$$

is satisfied. For $kR_s > 1$ the truncation number is [33], [34], [35], [36], [37, pp. 86-88]

$$N_Q = \text{int}\left(kR_s + \gamma(kR_s)^{1/3}\right), \quad \gamma = \frac{(-3\ln\mathcal{E})^{2/3}}{2} \tag{16}$$

where "int" denotes the integer part and "ln" is the natural logarithm. This equation shows that a typical non-resonant source with $R_s = N_Q/k$ can radiate a pattern whose spherical expansion coefficients are significantly nonzero at least up to $n = N_Q$. The truncation formula (16) does not hold for resonant sources, which can radiate far fields that require a much larger number of terms in the spherical expansion [38].

3. Complex-source beam

The complex-source beam $\Psi_{CSB}(\mathbf{r})$ of the present paper is obtained by inserting a complex source point $\mathbf{r}' = ia\hat{\mathbf{r}}'$ with $a > 0$ into the free-space Green's function to get (after introducing the $4\pi\, e^{-ka}$ normalization
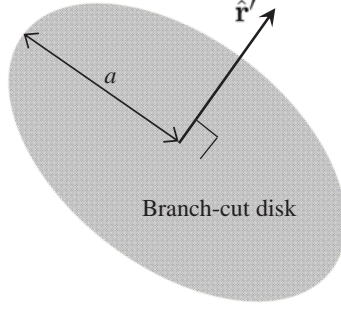
Figure 2: *The sources of the complex-source beam in (17) reside on the branch-cut disk with radius a, centered at the origin with normal $\hat{\mathbf{r}}'$.*

factor)

$$\Psi_{CSB}(\mathbf{r}) = 4\pi\, e^{-ka}\, G(\mathbf{r}, ia\hat{\mathbf{r}}') = e^{-ka}\, \frac{e^{ik\sqrt{(\mathbf{r}-ia\hat{\mathbf{r}}')^2}}}{\sqrt{(\mathbf{r}-ia\hat{\mathbf{r}}')^2}} \tag{17}$$

where the distance $\sqrt{(\mathbf{r}-ia\hat{\mathbf{r}}')^2}$ is complex with the square root defined to have a non-negative real part and its branch cut placed along the negative real axis [6], [21]. Hence, the field Ψ_{CSB} satisfies the homogeneous Helmholtz equation everywhere except on the branch cut of the square root where the sources reside. The manifestation of this branch cut in 3D space are those points $\mathbf{r}$ where $(\mathbf{r}-ia\hat{\mathbf{r}}')^2$ is a negative number. One readily finds that

$$(\mathbf{r}-ia\hat{\mathbf{r}}')^2 = r^2 - a^2 - 2ia\,\hat{\mathbf{r}}'\cdot\mathbf{r} \tag{18}$$

is negative on a disk of radius a, centered at the origin with normal $\hat{\mathbf{r}}'$; see Figure 2. This branch-cut disk in 3D space contains the sources of $\Psi_{CSB}(\mathbf{r})$. Expressions for these sources can be found by applying the Helmholtz operator $(\nabla^2 + k^2)$ to $\Psi_{CSB}(\mathbf{r})$; see [29], [30], [31].

The e^{-ka} normalization in (17) ensures that the far-field pattern of the beam $\Psi_{CSB}(\mathbf{r})$ has a maximum value of one:

$$\mathcal{F}_{CSB}(\hat{\mathbf{r}}) = e^{ka(\hat{\mathbf{r}}\cdot\hat{\mathbf{r}}'-1)} \tag{19}$$

which shows that for $k > 0$ and $a > 0$ the beam radiates most strongly in the direction $\hat{\mathbf{r}}'$ and most weakly in the direction $-\hat{\mathbf{r}}'$. Note that Ψ_{CSB} exhibits Gaussian behavior near the direction $\hat{\mathbf{r}}'$: let $\cos\Theta = \hat{\mathbf{r}}\cdot\hat{\mathbf{r}}'$ in (19) to get

$$\mathcal{F}_{CSB}(\hat{\mathbf{r}}) \simeq e^{-ka\,\Theta^2/2} \tag{20}$$

when Θ is small.

3.1. Smallest possible source region

The inverse source problem, which consists of determining sources that radiate a given far-field pattern, does not have a unique solution [39]. However, for a given far-field pattern one can determine the smallest

possible region in which sources must reside [40], [41, sec. 3.2.8]. Let us determine the smallest possible source region that can radiate the pattern (19). We first consider $\hat{\mathbf{r}}' = \hat{\mathbf{z}}$ and determine the minimum dimension required in the direction normal to the disk. Following the procedure in [40], [41, sec. 3.2.8], we compute

$$\left| \mathcal{F}_{CSB}(\pi/2 - i\alpha, \phi) \, e^{-kz|\cos(\pi/2 - i\alpha)|} \right| = \left| e^{-ka} \, e^{-k(z-ia)\sinh\alpha} \right| = e^{-ka} \, e^{-kz\sinh\alpha} \tag{21}$$

which approaches zero for $z > 0$ and infinity for $z < 0$ as $\alpha \to \infty$. We obtain a similar result when $\hat{\mathbf{r}}' = -\hat{\mathbf{z}}$, so it follows that sources residing in the plane of the branch-cut disk can produce the pattern (19). To determine the extent of the minimum source region in the direction orthogonal to the disk normal, we consider $\hat{\mathbf{r}}' = \hat{\mathbf{x}}$ to get

$$\left| \mathcal{F}_{CSB}(\pi/2 - i\alpha, \phi) \, e^{-kz|\cos(\pi/2 - i\alpha)|} \right| = e^{-ka} \, e^{-k(z - a\cos\phi)\sinh\alpha} \tag{22}$$

which approaches zero for all ϕ and $z > a$ and approaches infinity for $z < a$ and $\phi = 0$ as $\alpha \to \infty$. These results combined with the theorem in [40], [41, sec. 3.2.8] show that the branch-cut disk in Figure 2 is the smallest source region that can exactly produce the pattern (19). Of course, there are larger source regions that can also produce that exact same pattern. As we shall see, smaller source regions can be devised to produce the pattern (19) to within any prescribed error limit. Naturally, if one lets the prescribed error limit approach zero, the physical extent of these smaller source regions approach the size of the branch-cut disk.

3.2. Spherical-harmonics expansion of the far-field pattern

Let us next examine the spherical-harmonics expansion of the complex-source beam. Analytical continuation of the Green's function expansion [42, p.742] gives

$$\frac{e^{-ka} \, e^{ik\sqrt{(\mathbf{r} - ia\hat{\mathbf{r}}')^2}}}{\sqrt{(\mathbf{r} - ia\hat{\mathbf{r}}')^2}} = 4\pi \, ik \, e^{-ka} \sum_{n=0}^{\infty} \sum_{m=-n}^{n} j_n(ika) \, h_n^{(1)}(kr) \, Y_{nm}(\theta, \phi) Y_{nm}^*(\theta', \phi') \tag{23}$$

and

$$e^{ka(\hat{\mathbf{r}} \cdot \hat{\mathbf{r}}' - 1)} = 4\pi \, e^{-ka} \sum_{n=0}^{\infty} \sum_{m=-n}^{n} i^{-n} j_n(ika) \, Y_{nm}(\theta, \phi) Y_{nm}^*(\theta', \phi'). \tag{24}$$

When the disk normal is in the z direction so that $\hat{\mathbf{r}}' = \hat{\mathbf{z}}$, the formula (24) reduces to

$$e^{ka(\cos\theta - 1)} = e^{-ka} \sum_{n=0}^{\infty} (2n+1) \, i^{-n} j_n(ika) \, P_n(\cos\theta). \tag{25}$$

For a prescribed relative error $\mathcal{E}$, the truncation number N_a is the smallest positive integer for which

$$\max_{\theta} \left| e^{ka(\cos\theta - 1)} - e^{-ka} \sum_{n=0}^{N_a} (2n+1) \, i^{-n} j_n(ika) \, P_n(\cos\theta) \right| < \mathcal{E} \tag{26}$$

is satisfied. The truncation formula for the corresponding complex-source formula in 2D was derived in [24]. Since spherical and cylindrical Bessel function are related through

$$j_n(Z) = \sqrt{\frac{\pi}{2Z}} \, J_{n+1/2}(Z) \tag{27}$$

90
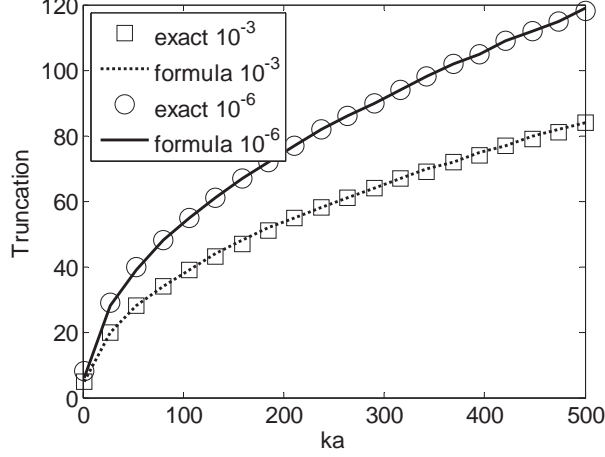
Figure 3: *The exact truncation number computed from (26) and the truncation number obtained from the formula (28) for $\mathcal{E} = 10^{-3}$ and $\mathcal{E} = 10^{-6}$. $\tilde{\gamma}$ is 3.7169 and 5.2565 when $\mathcal{E}$ is 10^{-3} and 10^{-6}, respectively.*

we can use the analysis from [24] to show that the truncation formula for the 3D formula (23) is

$$N_a = \text{int}\left(\tilde{\gamma}\sqrt{ka}\right) + 1, \quad \tilde{\gamma} = \sqrt{-2\ln\mathcal{E}}. \tag{28}$$

Figure 3 shows the exact truncation number computed from (26) and the truncation number obtained from the formula (28) for $\mathcal{E} = 10^{-3}$ and $\mathcal{E} = 10^{-6}$. This figure validates (28). For large ka, N_a in (28) is much smaller that N_Q in (16) with $R_s = a$. Indeed, the truncation formula (16) for general non-resonant sources grows linearly with frequency, whereas the truncation formula (28) for the complex-source beam grows as the square root of frequency. Therefore, $N_a/k < a$ when a is greater than just a few wavelengths, and the pattern of the complex-source beam can be created (even when a tight error bound is imposed) by a non-resonant source located inside a sphere with $R_s < a$.

3.3. Comparison to the constant-source disk radiator

For comparison we briefly consider the constant source that resides on a circular disk of radius a with $\hat{\mathbf{z}}$ as normal. The source function $Q(\mathbf{r}')$ is equal to a nonzero constant on the disk $x^2 + y^2 = a^2$, $z = 0$, and zero everywhere else. Its far-field pattern is

$$\mathcal{F}(\theta) = \frac{2\,J_1(ka\sin\theta)}{ka\sin\theta} \tag{29}$$

where $J_1(Z)$ is the cylindrical Bessel function of order one. The minimum source region for this pattern is also the physical disk [41, p. 145]. However, the truncation required to expand the pattern (29) is given by (16) with $R_s = a$. Hence, despite the fact that the constant source is non-singular, its far-field pattern expansion requires a much larger number of terms than the far-field pattern of the complex-source beam, which has a singularity along the rim of the source disk. Further, for a given prescribed accuracy, the array required to radiate the pattern (29) of the constant source must be bigger than the array required to radiate

91

the pattern (19) of the complex source. This is quite remarkable but in accordance with the fact that the directivity of the complex-source beam is low relative to the size of the branch-cut disk; see [22]. To illustrate, we note that for $ka = 50$, the $3\,\mathrm{dB}$ beam-widths of the complex-source beam (25) and the constant-source pattern (29) are $13.5°$ and $3.7°$, respectively. Also, the truncation formula (16) shows that the far-field pattern (29) *cannot* be created (even when a large error limit is allowed) by a non-resonant source located inside a sphere with $R_s < a$.
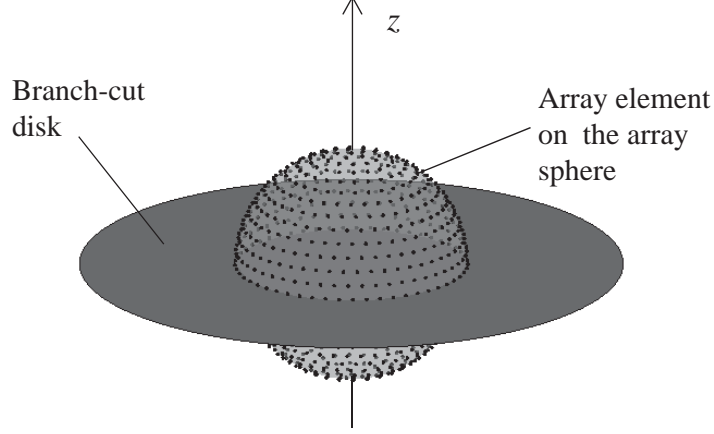
Figure 4: *The branch-cut disk with radius a in the $x - y$ plane and the array sphere of radius R_s on which the array elements reside. The array elements are spaced roughly Δ_S apart on the sphere. Here $R_s < a$ as in all the numerical examples. The array radiates a field that approximates that of the branch-cut disk.*

4. Array realization of a complex-source beam

The results from the previous sections will now be used to design a non-resonant array that radiates the far-field pattern of the complex-source beam to within a prescribed error limit. As discussed in Section 2, a typical non-resonant source with minimum radius R_s can radiate a pattern with an upper truncation limit of roughly $N_Q = kR_s$. Hence, (28) shows that to radiate a complex-source beam with beam parameter a with a precision of $\mathcal{E}$ requires that the array minimum radius be roughly

$$R_s = \tilde{\gamma}\sqrt{\frac{a}{k}} \tag{30}$$

which gives

$$a = \frac{kR_s^2}{\tilde{\gamma}^2} \tag{31}$$

and

$$\frac{R_s}{a} = \frac{\tilde{\gamma}}{\sqrt{ka}} \tag{32}$$

so that the required size of the array becomes smaller relative to the beam parameter as the frequency increases. The value of R_s given by (30) is conservative, and in actual implementations one can expect to

92

achieve a higher accuracy than $\mathcal{E}$ for the array far-field pattern when the array elements are well behaved; see Section 4.1.

We employ an array whose elements are distributed over a sphere with radius R_s as shown in Figure 4. The array elements are located on "rings" on the sphere: $\theta = \theta_q$, with $q = 1, ..., N_r$ where N_r is the number of rings. The ring at equator ($\theta = 90°$) contains the largest number of array elements and the rings at north and south poles ($\theta = 0$ and $\theta = 180°$) contain just one element each.
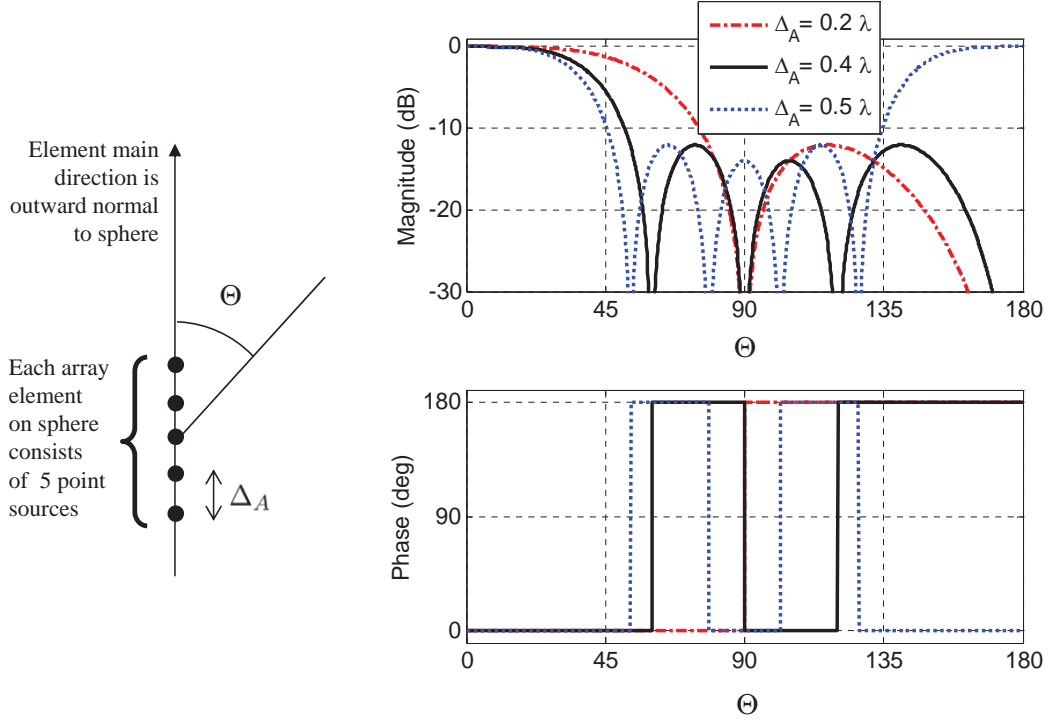
Figure 5: *Each array element on the sphere consists of five point sources arranged in an equal-weighted end-fire configuration. The distance between point sources is denoted by Δ_A as shown. The figure shows the array-element pattern for $\Delta_A = 0.2\lambda$, $\Delta_A = 0.4\lambda$, and $\Delta_A = 0.5\lambda$.*

Each array element consists of five point sources arranged in an equal-weighted end-fire configuration. The element pattern for three different point-source separations Δ_A are shown in Figure 5. We shall use $\Delta_A = 0.4\lambda$ since this results in strong radiation in the direction $\Theta = 0$ and weaker radiation in the opposite direction $\Theta = 180°$. When $\Delta_A = 0.5\lambda$ the array is not usable since the radiation in the directions $\Theta = 0$ and $\Theta = 180°$ are equally strong. Hence, each dot on the sphere in Figure 4 represents an outward radiating end-fire element with three sidelobes.

The array excitation coefficients are determined by matching the array far-field pattern to the far-field pattern (25) of the complex-source beam through a least-squares approach. Since the far-field pattern of the complex-source beam is independent of ϕ, the array excitation coefficients are the same for all elements on

a ring. The array excitation coefficients are denoted by A_q, so the array pattern has the form

$$\mathcal{F}_A(\theta, \phi) = \sum_{q=1}^{N_r} A_q \sum_{p=1}^{N_e(q)} \mathcal{F}_e(\theta, \phi; \mathbf{r}'_{pq}) \tag{33}$$

with

$$\mathbf{r}'_{pq} = R_s \sin \theta_q \cos \phi_{pq} + R_s \sin \theta_q \sin \phi_{pq} + R_s \cos \theta_q \tag{34}$$

where ϕ_{pq}, $p = 1, ..., N_e(q)$ determines the ϕ location of each array element on the ring with $\theta = \theta_q$. The number of elements on the ring $\theta = \theta_q$ is $N_e(q)$. Moreover, $\mathcal{F}_e(\theta, \phi; \mathbf{r}'_{pq})$ is the pattern of a single array element with reference point at $\mathbf{r}'_{pq}$ on the sphere, which is a translated and rotated version of the element pattern shown in Figure 5.

The array excitation coefficients A_q are determined through a least-squares method to minimize

$$C = \sum_{j=1}^{J} \left| \mathcal{F}_A(\theta_j, \phi_j) - e^{ka(\cos \theta_j - 1)} \right|^2 \tag{35}$$

where (θ_j, ϕ_j), $j = 1, ..., J$ is a set of evenly distributed points on the far-field sphere.
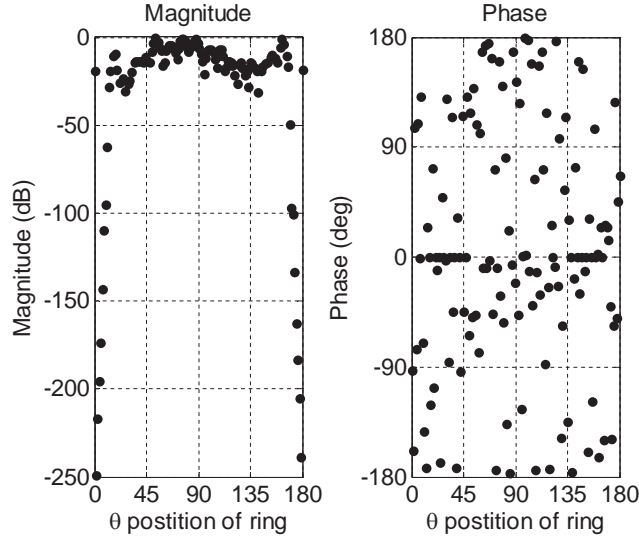
Figure 6: *Magnitude and phase of excitation coefficients for array elements on 132 rings given by $\theta = \theta_q$. The array elements are located on a sphere with $R_s = 21\lambda$. The excitation coefficients are computed to make the array radiate the pattern of a complex source with $a = 100\lambda$. The total number of array elements is 21850.*

4.1. Numerical example

We next present a numerical example where $a = 100\lambda$ and the error limit is set to $\mathcal{E} = 10^{-6}$. The formula (30) for the radius of the array sphere gives $R_s = 21\lambda$, and we space the array elements on the sphere roughly $\Delta_S = \lambda/2$ apart. For this configuration, $N_r = 132$ and the total number of array elements is 21850.
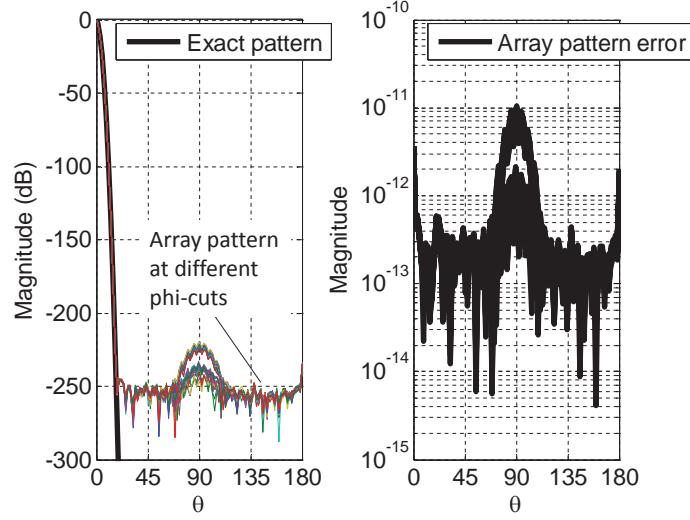
Figure 7: *Exact far-field pattern of the complex source and the pattern of the array with excitation coefficients given in Figure 6. The array pattern error is at the $-220\,dB$ level.*
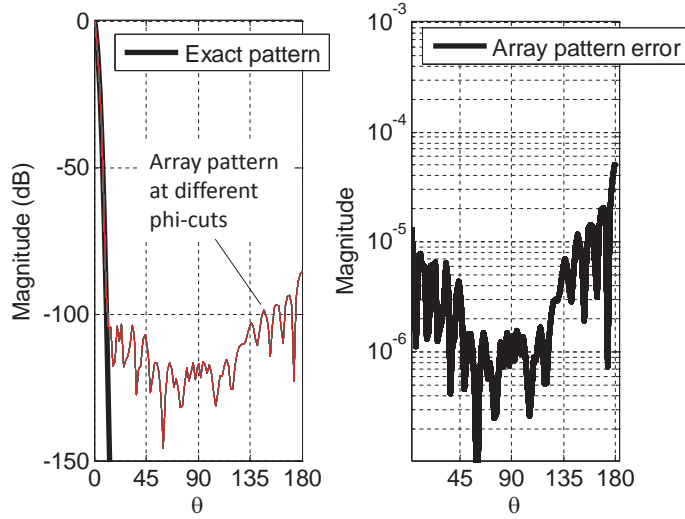
Figure 8: *Exact far-field pattern of the complex source and the pattern of the array with excitation coefficients given in Figure 6. The dynamic range for the excitation coefficients is limited to $100\,dB$ resulting in an array pattern error at the $-80\,dB$ level.*

Figure 6 shows amplitude and phase of the 132 excitation coefficients A_q obtained from the least-squares approach. Figure 7 shows the corresponding array pattern and its deviation from the exact pattern. We see that the array pattern error is at the $-220\,$dB level. A high-quality anechoic chamber has a dynamic range of $60\,$dB, and radar signals have a dynamic range that is typically several tens of decibels ($100\,$dB in extreme cases) [43, p. 4]. Hence, a measurement instrument in an anechoic chamber or a radar receiver would not be able to distinguish between two patterns in Figure 7 whose difference is at the $-220\,$dB level. In other words, due to noise and other disturbances, experiments performed with the array pattern will

produce exactly the same results as experiments performed with the exact complex-source beam pattern. Nevertheless, a weighted least-squares method could further reduce the error away from the main-beam direction, if desired.

In Figure 8 the array pattern and its error is computed with the dynamic range of the array excitation coefficients limited to 100 dB. In other words, all array excitation coefficients A_q with a magnitude less than -100 dB are set to zero. This set of "truncated" excitation coefficients produce a far-field pattern with a -80 dB error level. Again, for practical purposes this array pattern can be considered exact.

This numerical example has demonstrated that we can practically reproduce the exact far-field pattern of a complex source with $a = 100\lambda$ using an array whose diameter is only one fifth of the diameter of the branch-cut disk. In the next section we consider the array realization of a complex-source pulsed beam.

5. Array realization of complex-source pulsed beam

With $f = \omega/(2\pi)$ being the frequency, a real function of time $h(t)$ can be computed from its Fourier transform

$$H(f) = \int_{-\infty}^{\infty} h(t)\, e^{2\pi\, ift} dt \tag{36}$$

as

$$h(t) = 2\,\mathrm{Re}\left(\int_{0}^{\infty} H(f)\, e^{-2\pi\, ift}\, df\right) \tag{37}$$

where "Re" indicates that the real part is taken. We shall create an array that radiates a complex-source pulsed beam whose driving function has the Gaussian spectrum

$$H(f) = e^{-(f-f_c)^2/(2\sigma^2)}, \quad f \geq 0 \tag{38}$$

where f_c is the center frequency and σ the standard deviation. The complex-source pulsed beam driven by this signal has a frequency-domain far-field pattern given by

$$\mathcal{F}_{CSB}(\theta, f) = e^{-(f-f_c)^2/(2\sigma^2)}\, e^{2\pi f a\,(\cos\theta - 1)}, \quad f \geq 0 \tag{39}$$

where we have assumed that wave-speed is one so that $k = 2\pi/\lambda = 2\pi f$. We chose the center frequency to be $f_c = 1$, the standard deviation to be $\sigma = 0.1$, and the disk radius to be $a = 3$. Figure 9 shows the time and frequency domain far-field patterns associated with these parameter values.

The array sphere radius is $R_s = 2$ and the array element spacing is $\Delta_S = 0.35$. Figure 9 shows that the maximum effective frequency is roughly $f = 1.4$, so the minimum effective wavelength is $\lambda_{min} = 1/1.4 = 0.7143$. Hence, with $\Delta_S = 0.35$ we have ensured that the array element spacing on the sphere is less than half a wavelength at all frequencies of the driving signal. This configuration has 376 array elements distributed on $N_r = 18$ rings.

96
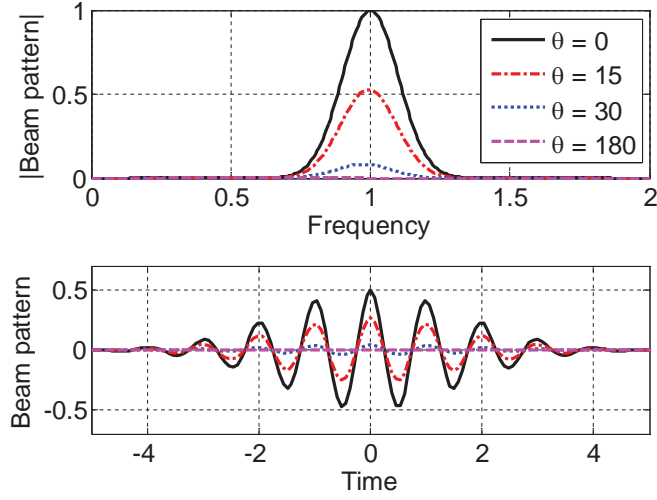
Figure 9: *The top plot is the exact frequency spectrum (39) of the beam pattern for different values of θ for a complex source with source point $\mathbf{r}_s = ia\hat{\mathbf{z}}$. The parameters are $a = 3$, $f_c = 1$, and $\sigma = 0.1$. The bottom plot is the corresponding time-domain beam pattern.*

As before, each array element consists of 5 point sources in the end-fire configuration shown in Figure 5. By choosing the spacing between point sources to be $\Delta_A = 0.28$ we have $\Delta_A = 0.4\lambda_{min}$, which ensures that the array element always radiates most strongly in the direction $\Theta = 0$ over the entire frequency band of the pulse in Figure 9. Figure 10 shows the array excitation coefficients obtained by solving the least-squares problem as functions of frequency for four of the eighteen rings. These excitation coefficients behave smoothly with respect to frequency in the frequency band of interest: $0.6 < f < 1.4$.
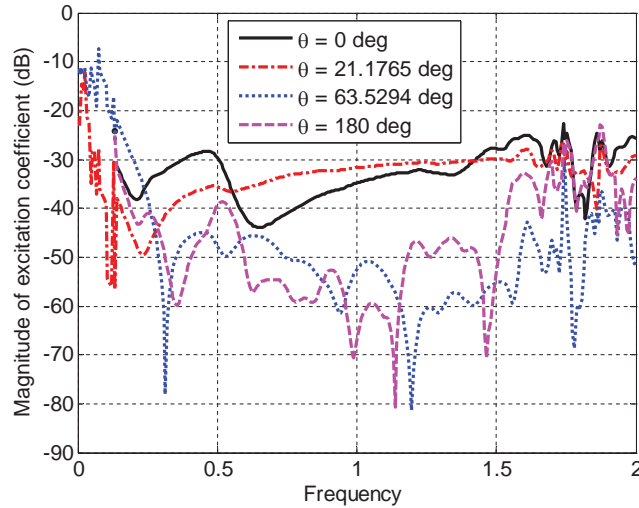
Figure 10: *Array excitation coefficients as functions of frequency for array elements on four rings. The parameters are $R_s = 2$, $\Delta_S = 0.35$, $\Delta_A = 0.28$, $a = 3$, $f_c = 1$, and $\sigma = 0.1$.*

97

Outside the frequency band of interest (for example around $f = 1.75$) the excitation coefficients exhibit non-smooth behavior. This is due to the fact that $\Delta_A = 0.28 \simeq 1/(2f)$ at $f = 1.75$, and thus each array element radiates an equal amount of power into both of its end-fire directions $\Theta = 0$ and $\Theta = 180°$; see Figure 5. Indeed, we verified numerically that had we chosen $\Delta_A = 0.4$, the non-smooth behavior would have occurred around $f = 1.25$, which is in the frequency range of interest. A non-smooth behavior of the frequency-domain excitation coefficients results in the corresponding time-domain excitation coefficients having long time durations. Therefore, it is important to choose proper array elements that work over the entire frequency band of interest.
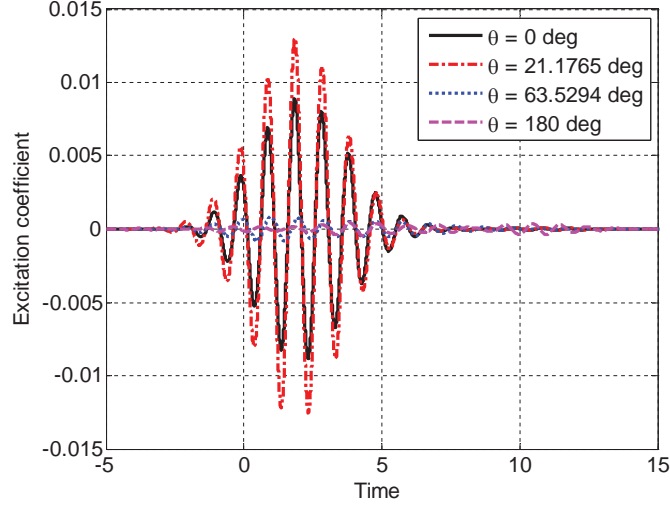
Figure 11: *Array excitation coefficients as functions of time for array elements on four rings. The parameters are $R_s = 2$, $\Delta_S = 0.35$, $\Delta_A = 0.28$, $a = 3$, $f_c = 1$, and $\sigma = 0.1$.*

Figure 11 shows the corresponding time-domain excitation coefficients obtained by multiplying the frequency-domain excitation coefficients in Figure 10 by the driving function in (38) and taking the inverse Fourier transform (37). We see that the durations of the excitation coefficients are roughly the same as the duration of the pulsed beam. Due to the geometry of the sphere, the excitation coefficients are shifted in time.

Figure 12 shows the array far-field pattern and its deviation from the desired complex-source pulsed beam far-field pattern. The maximum error of the array pattern is $4 \cdot 10^{-4}$, which is $62\,\mathrm{dB}$ below the maximum value of the exact pattern in Figure 9. Hence, we have achieved a very accurate representation of a complex-source pulsed beam with $a = 3$ using an array that is located on a sphere of radius $R_s = 2$.

6. Conclusions

Simple non-resonant array solutions were presented for reproducing (to within a specified error limit) the far-field pattern of complex-source beams in both frequency and time domains. Remarkably, the physical
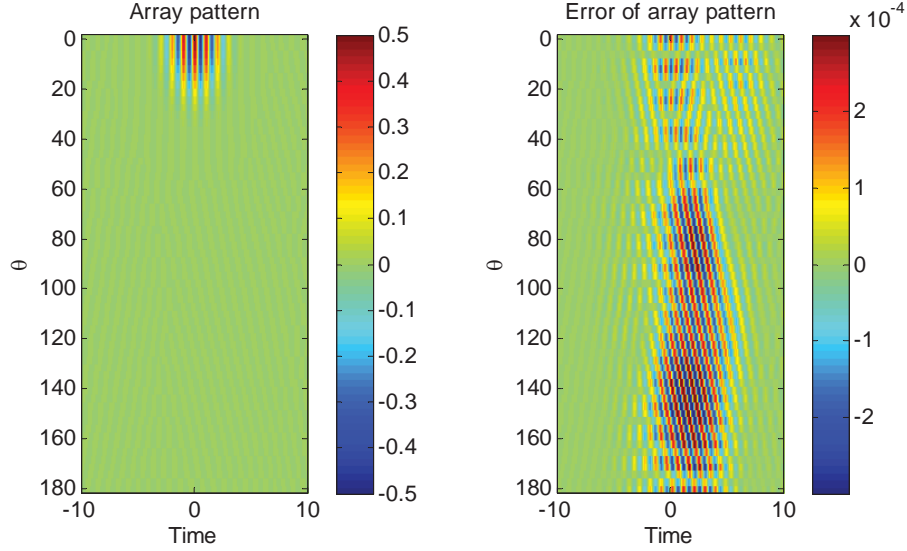
Figure 12: *The time-domain array pattern and its deviation from the desired complex-source pattern. The parameters are* $R_s = 2$, $\Delta_S = 0.35$, $\Delta_A = 0.28$, $a = 3$, $f_c = 1$, *and* $\sigma = 0.1$.

dimensions of these arrays are smaller than the physical dimensions of the branch-cut disks. The numerical examples demonstrated the validity of the theory using array elements with a typical sidelobe structure. Hence, the results of the paper can be reproduced with ordinary electro-acoustic transducers as array elements. Also, the least-squares approach used to determine the array excitation coefficients does not require that the array surface be a sphere. It would work for any surface of sufficient physical extent. Arrays for radiating an electromagnetic complex-source beam can be obtained in a similar manner.

We emphasize that the arrays in Sections 4 and 5 would *not* radiate the pattern of a typical source contained in the sphere with radius a, regardless of the excitation coefficients. Indeed, these arrays would be too small to radiate the pattern of the constant source discussed Section 3.3. These small arrays work only for the complex-source beam, which has a broad beam-width relative to the size of the branch-cut disk.

Acknowledgments

References

[1] G.A. Deschamps, "Gaussian beam as a bundle of complex rays," *Electron. Lett.*, vol. 7, pp. 684-685, 1971.

[2] E. Heyman and L.B. Felsen, "Propagating pulsed beam solutions by complex source parameter substitution", *IEEE Trans. Antennas Propagat.*, vol. 34, pp. 1062-1065, August 1986.

[3] E. Heyman, "Complex source pulsed beam representation of transient radiation," *Wave Motion*, vol. 11, pp. 337-349, 1989.

[4] J.B. Keller and W. Streifer, "Complex rays with an application to gaussian beam," *J. Opt. Soc. Amer.*, vol. 61, pp. 40-43, 1971.

[5] M. Couture and P.A. Belanger, "From Gaussian beam to complex-source-point spherical wave", *Phys. Rev. A*, vol. 24, pp. 355-359, 1981.

[6] L.B. Felsen, "Complex-point-source solutions of the field equations and their relation to the propagation and scattering of Gaussian beams", *Symp. Math. Instituta di alta Matetmatica,* vol. 18, pp. 39-56, 1976.

[7] L.B. Felsen, "Geometrical theory of diffraction, evanescent waves and complex rays," *Geophys. J. R. Astron. Soc.*, vol. 79, pp. 77-88, 1982.

[8] M.M. Popov, "A new method of computation of wave fields using Gaussian beams," *Wave Motion,* vol. 4, pp. 85-97, 1982.

[9] V. Červený, M.M. Popov, and I. Pšenčik, "Computation of wave fields in inhomogeneous mediaGaussian beam approach," *Geophys. J. R. Astr. Soc.,* vol. 70, pp. 109-128, 1982.

[10] V.M. Babich and M.M. Popov, "Gaussian summation method (review)," *Radiophys. Quantum Electron.,* vol. 39, pp. 1063-1081, 1989.

[11] B.S. White, A.N. Norris, A. Bayliss, and R. Burridge, "Some remarks on the Gaussian beam summation method," *Geophys. J. R. Astr. Soc.,* vol. 89, pp. 579-636, 1987.

[12] H.C. Choi and J.G. Harris, "Scattering of an ultrasonic beam from a curved interface," *Wave Motion*, vol. 11, pp. 383-406, 1989.

[13] E. Heyman and L. B. Felsen, "Gaussian beam and pulsed beam dynamics: Complex source and spectrum formulations within and beyond paraxial asymptotics," *J. Opt. Soc. Am. A,* vol. 18, no. 7, pp. 1588-1610, 2001.

[14] H.T. Chou, P.H. Pathak, and R.J. Burkholder, "Novel Gaussian beam method for the rapid analysis of large reflector antennas," *IEEE Trans. Antennas Propagat.,* vol. 49, pp. 880-893, June 2001.

[15] M. Katsav and E. Heyman, "Gaussian beam summation representation of half plane diffraction: A full 3D formulation," *IEEE Trans. Antennas Propag.,* vol. 57, pp. 1081-1094, April 2009.

[16] A.N. Norris, "Complex point-source representation of real point sources and the Gaussian beam summation method," *J. Opt. Soc. Am.,* vol. 3, no. 12, pp. 2005-2010, December 1986.

[17] A.N. Norris and T.B. Hansen, "Exact complex source representations of time-harmonic radiation," *Wave Motion*, vol. 25, pp. 127-141, 1997.

[18] T.B. Hansen and A.N. Norris, "Exact complex source representations of transient radiation," *Wave Motion*, vol. 26, pp. 101-115, 1997.

[19] T.B. Hansen, "Efficient field computation using Gaussian beams for both transmission and reception," *Wave Motion*, 2010, doi:10.1016/j.wavemoti.2010.10.009.

[20] K. Tap, P. H. Pathak and R. J. Burkholder, "Exact complex source point beam expansions for electromagnetic fields," *IEEE Trans. Antennas Propagat.,* vol. 59, pp. 3379-3390, September 2011.

[21] T.B. Hansen and G. Kaiser, "Generalized Huygens principle with pulsed-beam wavelets," *Journal of Physics A: Mathematical and Theoretical*, vol. 42, No. 47, 27 November 2009, paper # 475403.

[22] T.B. Hansen and G. Kaiser, "Huygens' principle for complex spheres," *IEEE Trans. Antennas Propagat.,* vol. 59, pp. 3835-3847, October 2011.

[23] T.B. Hansen, "Exact Gaussian-beam theory for outgoing and standing spherical waves: Application to transmitting and receiving antennas," *IEEE Trans. Antennas Propagat.,* vol. 60, pp. 1291-1302 , March 2012.

[24] T.B. Hansen, "Translation operator based on Gaussian beams for the fast multipole method in two dimensions," *Wave Motion*, vol. 50, pp. 793-808, June 2013.

[25] T.B. Hansen, "Translation operator based on Gaussian beams for the fast multipole method in three dimensions," *Wave Motion*, vol. 50, pp. 940-954, July 2013.

[26] T.B. Hansen, "Numerical properties of a Gaussian translation operator for the 2D FMM," *IEEE Trans. Antennas Propagat.*, vol. 62, pp. 3119-3129, June 2014.

[27] T.B. Hansen, "Exact plane-wave expansion with directional spectrum: application to transmitting and receiving antennas", *IEEE Trans. Antennas Propagat.*, vol. 62, pp. 4187-4198, August 2014.

[28] E. Heyman, V. Lomakin, and G. Kaiser, "Physical source realization of complex source pulsed beams," *J. Acoust. Soc. Am.*, vol. 107, pp. 1880-1891, 2000.

[29] G. Kaiser, "Physical wavelets and their sources: real physics in complex spacetime," *Top. Rev. J. Phys. A*, vol. 36, R29R338, 2003, http://arxiv.org/abs/math-ph/0303027

[30] G. Kaiser, "Making electromagnetic wavelets," *J. Phys. A: Math. Gen.*, vol. 37, pp. 5929-5947, 2004. http://arxiv.org/abs/ math-ph/0402006

[31] G. Kaiser, "Making electromagnetic wavelets: II. Spheroidal shell antennas," *J. Phys. A: Math. Gen.*, vol. 38, pp. 495-508, 2005. http://arxiv.org/abs/math-ph/0408055

[32] A.J. Devaney, G. Kaiser, E.A. Marengo, R. Albanese, and G. Erdmann, "The inverse source problem for wavelet fields," *IEEE Trans. Antennas Propagat.*, vol. 56, pp. 3179-3187, October 2008.

[33] V.I. Turchin and N.M. Tseytlin, "Antenna testing based on near-field measurements (Review)," *Radio Engineering & Electronic Physics,* vol. 24, pp. 1-26, December 1979.

[34] W.J. Wiscombe, "Improved Mie scattering algorithms," *Applied Optics,* vol. 19, pp. 1505-1509, May 1980.

[35] V. Rokhlin, "Sparse diagonal forms for translation operations for the Helmholtz equation in two dimensions," *Research Report YALEU/DCS/RR-1095,* December 1995.

[36] O.M. Bucci and G. Franceschetti, "On the spatial bandwidth of scattered fields," *IEEE Trans. Antennas Propagat.,* vol. 35, pp. 1445-1455, December 1987.

[37] W.C. Chew, J.M. Jin, E. Michielssen, and J. Song, eds, *Fast and Efficient Algorithms in Computational Electromagnetics,* Boston: Artech House, 2006.

[38] A.D. Yaghjian, "Sampling criteria for resonant antennas and scatterers," *J. Appl. Phys*, vol. 79, pp. 7474-6482, 1996.

[39] A.J. Devaney and G. Sherman, "Nonuniqueness in inverse source and scattering problems," *IEEE Trans. Antennas Propagat.,* vol. 30, pp. 1034-1037, September 1982.

[40] A.D. Yaghjian, T.B. Hansen, and A.J. Devaney, "Minimum source region for a given far-field pattern," *IEEE Trans. Antennas Propagat.*, vol. 45, pp. 911-912, May 1997.

[41] T.B. Hansen and A.D. Yaghjian, *Plane-Wave Theory of Time-Domain Fields,* New York: IEEE Press, 1999.

[42] J.D. Jackson, *Classical Electrodynamics,* 2nd Edition, New York: John Wiley & Sons, 1975.

[43] M.A. Richards, *Fundamentals of Radar Signal Procssing,* 2nd Edition, New York: McGraw Hill, 2014.

4.5.4

Electromagnetic Scattering-Matrix Theories Based on Plane Waves and Complex-Source Beams

T. B. Hansen[1]

[1]Seknion Inc., Boxford, Massachusetts, USA

Abstract— Two scattering-matrix theories for time-harmonic fields in three dimensions are presented: (i) a plane-wave theory with a directional spectrum that is obtained through a complex-source point substitution procedure, and (ii) a complex-source beam theory based on a beam expansion of spherical multipole fields. Scattering matrices for plane-wave expansions, which determine the plane-wave spectrum of the scattered field of an object due to an incoming plane wave, are readily available. The analogous scattering matrices based on complex-source beams will be derived from Waterman's T matrices. These scattering matrices determine the beam weights for the scattered field in terms of the output of elementary beam receivers, which sample the incident field at complex points in space. The two scattering-matrix formulations will also be compared with Kerns plane-wave theory.

1. INTRODUCTION

Plane waves and complex-source beams constitute complete sets of basis functions for electromagnetic fields in homogeneous source-free regions. From the completeness of these basis functions, we derive exact scattering-matrix theories, which can lead to efficient computation schemes for electromagnetic field transformations in both near and far-field regions. The plane-wave basis functions have sources of infinite extent whereas the complex-source beams have sources of finite extent. Hence, the two types of expansions are distinctly different in many ways.

Figure 1 shows the electromagnetic scattering problem under consideration. The primary source generates the electric field $\mathbf{E}_p(\mathbf{r})$ that interacts with the scatterer to produce the scattered electric field $\mathbf{E}_s(\mathbf{r})$. Multiple interactions between the primary source and the scatterer are neglected. The minimum sphere of radius R_s centered at the origin encloses the scatterer, and the primary source region and the observation region are assumed to be outside this sphere. The global (x, y, z) coordinate system has origin near the scatterer. Further, $\mathbf{r}_p$ is a point in the source region that generates the primary field, and $\mathbf{r}_o$ is a point in the observation region.

The standard rectangular coordinates are denoted by (x, y, z) with unit vectors $\hat{\mathbf{x}}$, $\hat{\mathbf{y}}$, and $\hat{\mathbf{z}}$, so that a general point in space can be expressed as $\mathbf{r} = x\hat{\mathbf{x}} + y\hat{\mathbf{y}} + z\hat{\mathbf{z}}$. The spherical coordinates (r, θ, ϕ) are related to the rectangular coordinates through $x = r\sin\theta\cos\phi$, $y = r\sin\theta\sin\phi$, and $z = r\cos\theta$. The three spherical unit vectors are $\hat{\mathbf{r}} = \sin\theta\cos\phi\hat{\mathbf{x}} + \sin\theta\sin\phi\hat{\mathbf{y}} + \cos\theta\hat{\mathbf{z}}$, $\hat{\boldsymbol{\theta}} = \cos\theta\cos\phi\hat{\mathbf{x}} + \cos\theta\sin\phi\hat{\mathbf{y}} - \sin\theta\hat{\mathbf{z}}$, and $\hat{\boldsymbol{\phi}} = -\sin\phi\hat{\mathbf{x}} + \cos\phi\hat{\mathbf{y}}$. Throughout, $e^{-i\omega t}$ time dependence with $\omega > 0$ is assumed and suppressed. The wave number is $k = 2\pi/\lambda = \omega/c$, with c being the wave speed and λ the wave length.

2. EXPANSION BASED ON COMPLEX-SOURCE BEAMS

The complex-source beam of the present paper (also referred to as a Gaussian beam) was first obtained by Deschamps [1] by inserting a complex source point $\mathbf{r}' = ia\hat{\mathbf{r}}'$ with $a > 0$ into the scalar free-space Green's function to get

$$G(\mathbf{r}, ia\hat{\mathbf{r}}') = \frac{e^{ik\sqrt{(\mathbf{r}-ia\hat{\mathbf{r}}')^2}}}{4\pi\sqrt{(\mathbf{r}-ia\hat{\mathbf{r}}')^2}} \tag{1}$$

where the distance $\sqrt{(\mathbf{r}-ia\hat{\mathbf{r}}')^2}$ is complex with the square root defined to have a non-negative real part and its branch cut placed along the negative real axis [2]. For fixed $\hat{\mathbf{r}}'$ and varying $\mathbf{r}$ the branch cut manifests itself in real 3D space by a branch-cut disk of radius a, centered at the origin with normal $\hat{\mathbf{r}}'$. Hence, the field $G(\mathbf{r}, ia\hat{\mathbf{r}}')$ satisfies the homogeneous Helmholtz equation everywhere except on this branch-cut disk where the sources reside.
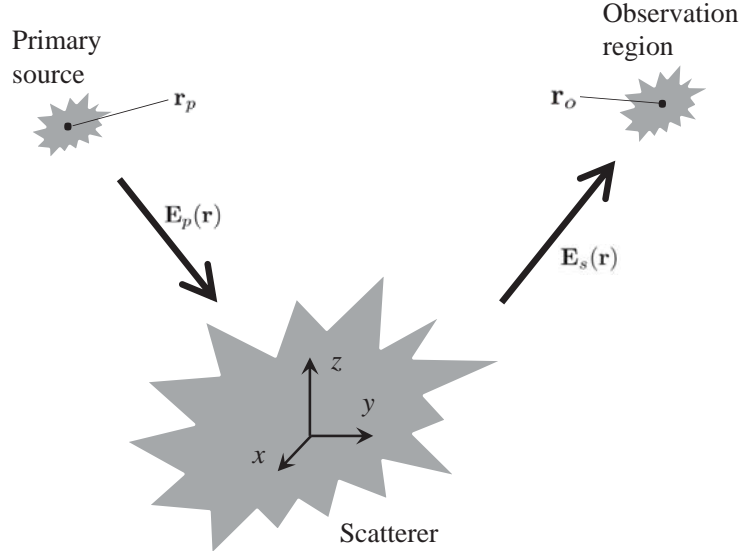
Figure 1: *The scattering configuration. The field $\mathbf{E}_p(\mathbf{r})$ of the primary source encounters the scatterer. The scattered field $\mathbf{E}_s(\mathbf{r})$ is observed in the observation region. $\mathbf{r}_p$ is a point in the source region and $\mathbf{r}_o$ is a point in the observation region.*

The far-field formula (valid for large r)

$$G(\mathbf{r}, ia\hat{\mathbf{r}}') \sim \frac{e^{ikr}}{4\pi r} e^{ka\hat{\mathbf{r}} \cdot \hat{\mathbf{r}}'} \tag{2}$$

shows that for $k > 0$ and $a > 0$ the beam radiates most strongly in the direction $\hat{\mathbf{r}}'$ and most weakly in the direction $-\hat{\mathbf{r}}'$. The name "Gaussian beam" is sometimes used because $G(\mathbf{r}, ia\hat{\mathbf{r}}')$ exhibits Gaussian behavior near the direction $\hat{\mathbf{r}}'$: let $\cos\Theta = \hat{\mathbf{r}} \cdot \hat{\mathbf{r}}'$ in (2) to get $G(\mathbf{r}, ia\hat{\mathbf{r}}') \sim [e^{ikr}/(4\pi r)] e^{ka(1-\Theta^2/2)}$ when Θ is small.

2.1. The scattered field

According to [3, eq.(38)], the scattered field can be expressed in terms of complex-source beams with beam parameter a_s as ($\int d\Omega'$ denotes the integral over the unit sphere with respect to $\hat{\mathbf{r}}'$)

$$\mathbf{E}_s(\mathbf{r}) = \int d\Omega' \, G(\mathbf{r}, ia_s\hat{\mathbf{r}}') \left[\mathbf{F}_M(\mathbf{r}, ia_s\hat{\mathbf{r}}')W_A(\theta',\phi') + \mathbf{F}_N(\mathbf{r}, ia_s\hat{\mathbf{r}}')W_B(\theta',\phi')\right] \tag{3}$$

with

$$\mathbf{F}_M(\mathbf{r}, \mathbf{r}') = \left(\frac{1}{R^2} - \frac{ik}{R}\right)\mathbf{r}' \times \mathbf{r}, \qquad R = \sqrt{(\mathbf{r} - \mathbf{r}')^2}, \tag{4}$$

$$\mathbf{F}_N(\mathbf{r}, \mathbf{r}') = \frac{2}{k}\left(\frac{1}{R^2} - \frac{ik}{R}\right)\mathbf{r}' + \left(\frac{3}{R^2} - \frac{3ik}{R} - k^2\right)\frac{\mathbf{r}\mathbf{R} \cdot \mathbf{r}' - \mathbf{r}'\mathbf{R} \cdot \mathbf{r}}{kR^2}, \qquad \mathbf{R} = \mathbf{r} - \mathbf{r}' \tag{5}$$

and

$$W_A(\theta, \phi) = \sum_{\ell=1}^{L}\sum_{m=-\ell}^{\ell} \frac{A_{\ell m} Y_{\ell m}(\theta, \phi)}{\sqrt{\ell(\ell+1)}\, ik\, j_\ell(ika_s)}, \qquad W_B(\theta, \phi) = \sum_{\ell=1}^{L}\sum_{m=-\ell}^{\ell} \frac{B_{\ell m} Y_{\ell m}(\theta, \phi)}{\sqrt{\ell(\ell+1)}\, ik\, j_\ell(ika_s)} \tag{6}$$

where $Y_{\ell m}(\theta, \phi)$ is the spherical harmonic function and $j_\ell(Z)$ is the spherical Bessel function. Also, $A_{\ell m}$ and $B_{\ell m}$ are the spherical expansion coefficients of the scattered field to be determined below. Moreover, for non-resonant scatterers the truncation number is

$$L = \text{int}\left(kR_s + \gamma(kR_s)^{1/3}\right), \qquad \gamma = \frac{(-3\ln\mathcal{E})^{2/3}}{2} \tag{7}$$

with $\mathcal{E}$ being the desired relative accuracy, and "ln" and "int" denoting the natural logarithm and integer part, respectively.

2.2. The primary field

The spherical expansion coefficients for the standing spherical-wave representation of the primary field can be expressed in terms of the output of elementary complex-point receivers as [3, eqs.(52)-(53)]

$$C_{\ell m} = \frac{1}{j_\ell(ika_p)} \int d\Omega \, \mathbf{E}_p(ia_p\hat{\mathbf{r}}) \cdot \mathbf{M}^*_{\ell m}(\theta, \phi), \quad D_{\ell m} = \frac{1}{v_\ell^{(1)}(ika_p)} \int d\Omega \, \mathbf{E}_p(ia_p\hat{\mathbf{r}}) \cdot \mathbf{N}^*_{\ell m}(\theta, \phi) \qquad (8)$$

where $a_p > 0$ is a beam parameter, $*$ denotes complex conjugation, $v_\ell^{(1)}(Z) = \frac{1}{Z}\frac{\partial}{\partial Z}[Zj_\ell(Z)]$, and

$$\mathbf{M}_{\ell m}(\theta, \phi) = \hat{\boldsymbol{\theta}} \, \frac{im\, Y_{\ell m}(\theta, \phi)}{\sqrt{\ell(\ell+1)}\,\sin\theta} - \hat{\boldsymbol{\phi}} \, \frac{\frac{\partial}{\partial\theta}Y_{\ell m}(\theta, \phi)}{\sqrt{\ell(\ell+1)}}, \qquad \mathbf{N}_{\ell m}(\theta, \phi) = \hat{\mathbf{r}} \times \mathbf{M}_{\ell m}(\theta, \phi) \qquad (9)$$

are the transverse vector-wave functions. The quantity $\mathbf{E}_p(ia_p\hat{\mathbf{r}})$ is the output of a complex-point receiver as explained in [3]; see also Section 2.3 below.

2.3. The scattering matrix

The spherical-wave scattering matrix $\bar{\boldsymbol{\Lambda}}$ (also referred to as Waterman's T-matrix) for a particular scatterer determines the spherical expansion coefficients $A_{\ell m}$ and $B_{\ell m}$ for the scattered field in terms of the spherical expansion coefficients $C_{\ell m}$ and $D_{\ell m}$ for the primary field as [4], [5] (note that [5] defines the scattering matrix in terms of "incoming" and "outgoing" spherical waves rather than the "standing" and "outgoing" spherical waves used here; see [5, p.46])

$$A_{\ell m} = \sum_{\ell'=0}^{L} \sum_{m'=-\ell'}^{\ell'} \Lambda^{(AC)}_{\ell\ell'mm'} C_{\ell'm'} + \Lambda^{(AD)}_{\ell\ell'mm'} D_{\ell'm'}\Big], \qquad B_{\ell m} = \sum_{\ell'=0}^{L} \sum_{m'=-\ell'}^{\ell'} \Lambda^{(BC)}_{\ell\ell'mm'} C_{\ell'm'} + \Lambda^{(BD)}_{\ell\ell'mm'} D_{\ell'm'}\Big].$$
$$(10)$$

Hence, the scattered field can be expressed in terms of the output of elementary complex-point receivers as

$$\mathbf{E}_s(\mathbf{r}) = \int d\Omega' \, G(\mathbf{r}, ia_s\hat{\mathbf{r}}') \left[\mathbf{F}_M(\mathbf{r}, ia_s\hat{\mathbf{r}}') \int d\Omega'' \, \mathbf{Q}_A(\hat{\mathbf{r}}', \hat{\mathbf{r}}'') \cdot \mathbf{E}_p(ia_p\hat{\mathbf{r}}'') \right.$$
$$\left. + \mathbf{F}_N(\mathbf{r}, ia_s\hat{\mathbf{r}}') \int d\Omega'' \, \mathbf{Q}_B(\hat{\mathbf{r}}', \hat{\mathbf{r}}'') \cdot \mathbf{E}_p(ia_p\hat{\mathbf{r}}'') \right] \qquad (11)$$

where the complex-source scattering matrices are given by

$$\mathbf{Q}_A(\hat{\mathbf{r}}', \hat{\mathbf{r}}'') = \sum_{\ell=1}^{L} \sum_{m=-\ell}^{\ell} \frac{(ik)^{-1}Y_{\ell m}(\theta', \phi')}{\sqrt{\ell(\ell+1)}\,j_\ell(ika_s)} \sum_{\ell'=0}^{L} \sum_{m'=-\ell'}^{\ell'} \left[\Lambda^{(AC)}_{\ell\ell'mm'} \frac{\mathbf{M}^*_{\ell'm'}(\theta'', \phi'')}{j_{\ell'}(ika_p)} + \Lambda^{(AD)}_{\ell\ell'mm'} \frac{\mathbf{N}^*_{\ell'm'}(\theta'', \phi'')}{v_{\ell'}^{(1)}(ika_p)} \right]$$
$$(12)$$

and $\mathbf{Q}_B(\hat{\mathbf{r}}', \hat{\mathbf{r}}'')$ is given by (12) with $\Lambda^{(AC)}_{\ell\ell'mm'}$ replaced by $\Lambda^{(BC)}_{\ell\ell'mm'}$ and $\Lambda^{(AD)}_{\ell\ell'mm'}$ replaced by $\Lambda^{(BD)}_{\ell\ell'mm'}$. One can derive integral equations from which the complex-source scattering matrices can be computed numerically for a given scatterer without using Waterman's T-matrix.

The formula (11) expresses the scattered field directly in terms of the output $\mathbf{E}_p(ia_p\hat{\mathbf{r}}'')$ of an elementary complex-point receiver pointing in all directions (in other words, in terms of the incident electric field evaluated at imaginary points of the form $ia_p\hat{\mathbf{r}}''$, where $\hat{\mathbf{r}}''$ covers the unit sphere). The directivity of these receivers ensure that one can neglect directions $\hat{\mathbf{r}}''$ that do not point towards the primary source region. Similarly, the directivity of the transmitting beams in the $\hat{\mathbf{r}}'$ integral ensure that one can neglect directions $\hat{\mathbf{r}}'$ that do not point towards the observation region. Also, note that the scattering matrix contains two free parameters (the disk radii a_p and a_s) that can be used to optimize the efficiency of the scattering calculation. Numerical examples that demonstrate the directional nature of the scalar analog of this scattering-matrix formulation can be found in [6].

Let us briefly discuss how $\mathbf{E}_p(ia_p\hat{\mathbf{r}}'')$ can be obtained through simulations or measurements. If the software used to perform simulations defines the square root to have non-negative real part and its branch cut along the negative real axis (Matlab's square root is defined this way), one simply sets the observation point equal to the imaginary point $ia_p\hat{\mathbf{r}}''$. No further work is needed. If the software defines the square root differently, one must write a new square-root function defined as described above. If the primary field is measured on a sphere centered on the primary source, outgoing spherical expansion coefficients are known. One can then compute $\mathbf{E}_p(ia_p\hat{\mathbf{r}}'')$ directly from the spherical vector-wave function expansion.

3. EXPANSION BASED ON PLANE WAVES

We next derive a scattering-matrix formulation that is based on the directional plane-wave expansion from [7].

3.1. The scattered field

We begin be introducing the far-field pattern of of the scattered field through the equation

$$\boldsymbol{\mathcal{F}}_s(\hat{\mathbf{r}}) = \lim_{r \to \infty} r \, e^{-ikr} \mathbf{E}_s(r\hat{\mathbf{r}}) \tag{13}$$

and find from [7, eq.(52)] that

$$\mathbf{E}_s(\mathbf{r}) = \frac{ik}{4\pi} \int d\Omega_k \, \boldsymbol{\mathcal{F}}_s(\hat{\mathbf{k}}) \, e^{i\mathbf{k}\cdot(\mathbf{r}-\mathbf{r}_o)} \, T_{N_o}(\hat{\mathbf{k}}, \mathbf{r}_o, \Delta_s) \tag{14}$$

where $\int d\Omega_k$ is the integral over the $\mathbf{k}$ unit sphere and

$$T_{N_o}(\hat{\mathbf{k}}, \mathbf{r}_o, \Delta_s) = e^{k\Delta(\hat{\mathbf{k}}\cdot\hat{\mathbf{r}}_o - 1)} \sum_{n=0}^{N_o} i^n (2n+1) \tilde{h}_n^{(1)}(k\{r_o + i\Delta_s\}) P_n(\hat{\mathbf{k}} \cdot \hat{\mathbf{r}}_o) \tag{15}$$

is the Gaussian translation operator that results in directional plane-wave spectra; see [7] for details. Further,

$$\tilde{h}_n^{(1)}(Z) = h_n^{(1)}(Z) \, e^{\text{Im}(Z)} \tag{16}$$

is a normalized spherical Hankel function and $P_n(Z)$ is the Legendre polynomial. The truncation number N_o, which depends on the beam parameter Δ_s as well as on the size of the scatterer and observation region, can be found from the procedure in [7, sec.VI] to achieve any desired accuracy. Note that the Gaussian translation operator (15) equals the standard translation operator when the beam parameter Δ_s equals zero.

3.2. The primary field

With the far-field pattern of the primary source (with respect to the origin $\mathbf{r}_p$) defined as

$$\boldsymbol{\mathcal{F}}_p(\hat{\mathbf{r}}) = \lim_{r \to \infty} r \, e^{-ikr} \mathbf{E}_p(r\hat{\mathbf{r}} - \mathbf{r}_p) \tag{17}$$

we find that

$$\mathbf{E}_p(\mathbf{r}) = \frac{ik}{4\pi} \int d\Omega_k \, \boldsymbol{\mathcal{F}}_p(\hat{\mathbf{k}}) \, e^{i\mathbf{k}\cdot\mathbf{r}} \, T_{N_p}(\hat{\mathbf{k}}, -\mathbf{r}_p, \Delta_p) \tag{18}$$

where the truncation number N_p, which depends on the beam parameter Δ_p as well as on the size of the scatterer and primary source region, can be found from the procedure in [7, sec.VI]. According to (18), the plane-wave spectrum for the incoming primary field is $[(ik)/(4\pi)]\boldsymbol{\mathcal{F}}_p(\hat{\mathbf{k}}) \, T_{N_p}(\hat{\mathbf{k}}, -\mathbf{r}_p, \Delta_p)$.

3.3. The scattering matrix

The far-field plane-wave scattering matrix $\bar{\mathbf{F}}(\hat{\mathbf{k}}', \hat{\mathbf{k}}'')$ determines the scattered far-field pattern in the direction $\hat{\mathbf{k}}'$ when the incident field is a single plane wave $\mathbf{E}_0 \, e^{i\mathbf{k}''\cdot\mathbf{r}}$ (with the constant vector $\mathbf{E}_0$ satisfying $\mathbf{E}_0 \cdot \mathbf{k}'' = 0$) as

$$\boldsymbol{\mathcal{F}}_s(\hat{\mathbf{k}}') = \bar{\mathbf{F}}(\hat{\mathbf{k}}', \hat{\mathbf{k}}'') \cdot \mathbf{E}_0 \tag{19}$$

which in turn gives the final expression for the scattered field

$$\mathbf{E}_s(\mathbf{r}) = -\frac{k^2}{16\pi^2} \int d\Omega_k' \, e^{i\mathbf{k}'\cdot(\mathbf{r}-\mathbf{r}_o)} \, T_{N_o}(\hat{\mathbf{k}}', \mathbf{r}_o, \Delta_s) \int d\Omega_k'' \, T_{N_p}(\hat{\mathbf{k}}'', -\mathbf{r}_p, \Delta_p) \, \bar{\mathbf{F}}(\hat{\mathbf{k}}', \hat{\mathbf{k}}'') \cdot \boldsymbol{\mathcal{F}}_p(\hat{\mathbf{r}}''). \tag{20}$$

In general, a scatterer that is illuminated by a single plane wave will produce plane waves propagating in all directions. Hence, the scattering matrix formula (20) contains an integral over both incoming plane-wave directions of propagation $\hat{\mathbf{k}}''$ and scattered plane-wave directions of propagation $\hat{\mathbf{k}}'$. The directionality of the Gaussian translation operators ensures that large portions of the $\hat{\mathbf{k}}'$ and $\hat{\mathbf{k}}''$ integration regions can be neglected.

The important special scattering geometry involving a half space was investigated in [8] using the standard translation operator ($\Delta_s = \Delta_p = 0$). The plane-wave scattering matrix for the half space is degenerate in the sense that a single incident plane wave will produce only one scattered plane wave. Therefore, for the half-space scatterer, the formula (20) simplifies so that it involves only the integral over incoming (or outgoing) plane-wave directions of propagation.

4. CONCLUSIONS

The two scattering-matrix formulations in (11) and (20) will now be compared to Kerns' plane-wave scattering-matrix formulation (one-sided) in which the scattered field is written as [9, pp.57–61]

$$\mathbf{E}_s(\mathbf{r}) = \int d\mathbf{K}' \, e^{i\mathbf{k}'\cdot\mathbf{r}} \int d\mathbf{K}'' \, \bar{\mathbf{S}}(\mathbf{K}', \mathbf{K}'') \cdot \mathbf{T}_p(\mathbf{K}'') \tag{21}$$

where $\bar{\mathbf{S}}(\mathbf{K}', \mathbf{K}'')$ is Kerns' plane-wave scattering matrix, and $\mathbf{T}_p(\mathbf{K}'')$ is the plane-wave spectrum of the primary field. Moreover, $\mathbf{K}'$ is the transverse part of the plane-wave propagation vector $\mathbf{k}'$ for the scattered field. Similarly, $\mathbf{K}''$ is the transverse part of the plane-wave propagation vector $\mathbf{k}''$ for the primary field. The plane-wave spectrum of the primary field $\mathbf{T}_p(\mathbf{K}'')$ can be thought of as the output of a plane-wave receiver that picks out a single plane-wave component of the primary field.

It is challenging to use the plane-wave expansion (21) in numerical computations that require a preselected accuracy. First, the integrand of the $\mathbf{K}'$ integral has an integrable singularity at $|\mathbf{K}'| = k$ that in many situations necessitates a change of variables [10, ch.3]. Second, in general the integrands do not decay until the evanescent regions $|\mathbf{K}'| > k$ and $|\mathbf{K}''| > k$ are reached. In some situations one must integrate all the way into the evanescent regions to avoid strong end-point contributions [7]. Nevertheless, there are some favorable situations where the integrals in (21) can be truncated to include only small regions in the propagating domains without introducing significant errors.

The expansions (11) and (20) have the same structure as (21). However, there are important differences. For example, the regions of integrations in both (11) and (20) are unit spheres whereas it is an infinite planar $\mathbf{K}$ surface in (21). Also, the integrands in (11) and (20) are well-behaved functions on the unit spheres that are directional at high frequencies, so that only parts of the unit spheres need to be included to achieve high accuracy. Hence, from a numerical point of view, the expansions (11) and (20) appear to have distinct advantages.

REFERENCES

1. Deschamps, G. A., "Gaussian beam as a bundle of complex rays," *Electron. Lett.*, Vol. 7, 684–685, 1971.
2. Felsen, L. B. "Complex source point solution of the field equations and their relation to the propagation and scattering of Gaussian Beams," *Symposia Mathematica,* Vol. 18, 39–56, 1976.
3. Hansen, T. B., "Exact Gaussian-beam theory for outgoing and standing spherical waves: Application to transmitting and receiving antennas," *IEEE Trans. Antennas Propagat.,* Vol. 60, 1291–1302 , March 2012.
4. Waterman, P. C., "Matrix formulation of electromagnetic scattering," *Proceedings of the IEEE*, Vol. 53, 805–812, August 1965.
5. Hansen, J. E., Ed., J. Hald, F. Jensen, and F. H. Larsen, *Spherical Near-Field Antenna Measurements,* Peter Peregrinus, 1988.
6. Hansen, T. B., "Exact Scattering-Matrix Theory Based on Gaussian Beams," *J. Acoust. Soc. Am.*, in review.
7. Hansen, T. B. "Exact plane-wave expansion with directional spectrum: Application to transmitting and receiving antennas," *IEEE Trans. Antennas Propagat.,* Vol. 62, 4187–4198, August 2014.
8. Schmidt, C. H. and T. F. Eibert, "Multilevel plane wave based near-field far-field transformation for electrically large antennas in free-space or above material halfspace," *IEEE Trans. Antennas Propagat.,* Vol. 57, 1382–1390, May 2009.
9. Kerns, D. M., *Plane-Wave Scattering-Matrix Theory of Antennas and Antenna-Antenna Interactions,* NBS Monograph 162, Washington, DC: U.S. Government Printing Office, 1981.
10. Hansen, T. B. and A. D. Yaghjian, *Plane-wave theory of time-domain fields,* IEEE Press 1999.

5. Metamaterial Theory

Robert A. Shore

5.1 Fundamental Homogenization Theory of Metamaterials

The subject of homogenization of metamaterials is of great importance in the theory of metamaterials composed of periodic arrays of particles, dealing with the central questions of when an array of discrete particles can be regarded as a homogeneous medium with effective permittivity and permeability, and how these effective parameters can be obtained. Clearly, being able to treat an array of discrete particles as a homogeneous medium is an enormous advantage over having to treat the array of particles itself. Andrea Alù in the 2011 Physical Review B (vol. 84, No. 7, 075153) has published a basic paper on homogenization of metamaterials, "First-principles homogenization theory for periodic metamaterials." In this paper Alù uses dimensional rather than non-dimensional quantities in his development making it difficult to go from the theory he presents to numerical calculations. In the technical memo bianiso2b.pdf [Section 5.4: Appendix], the derivation in Alù's paper is reformulated and expanded using nondimensional quantities, thus considerably improving its accessibility and applicability.

The effective parameters for scatterer arrays are obtained from the solutions for the eigenmodes supported by infinite 3-D arrays, but scattering calculations always involve semi-infinite or finite collections of the scatterers. Since metamaterial applications of this work always involve finite objects, it is essential to determine how well the effective parameters obtained from an analysis of an infinite periodic array describe scattering from finite collections of scatterers such as a spherical body carved from the infinite periodic array. Canonical problems investigated here are comparisons of exact bistatic scattering from a disk, cube, and spherical arrays of periodically placed magnetodielectric spheres, with the field scattered from a the corresponding homogeneous objects with effective permeability and permeability obtained from the eigenmode dispersion equation for the infinite array. The fields scattered from the arrays of periodically placed scatterers are obtained using multiple scattering techniques, while the scattered field obtained from the homogeneous objects is obtained using a fast surface-integral equation solver.

The paper[1] based on our work investigates the applicability to finite-size metamaterial arrays of a homogenized model based on dipolar approximations and infinite periodic arrays. The homogenization method is based on a dipolar model of the inclusions, which is shown to hold even in the case of densely packed arrays once weak forms of spatial dispersion and the full dynamic array coupling are properly taken into account. The near- and far-field scattering response of large-scale arrays of densely packed magnetodielectric spheres arranged in cylindrical and cubic shapes are numerically calculated using a fast surface integral equation solver at frequencies for which the bulk metamaterial supports positive or negative index of refraction. Comparing scattering patterns and near-field distributions inside and outside the structures, it is shown that the homogenized model can give a reasonably good description of the propagation and scattering properties of finite-size metamaterial objects, even for negative-

index, near-resonance operation. Accuracy of the results have been shown to improve for larger arrays, for which edge effects are less important, and for straight edges, for which staircasing effects are not observed at the array boundary. The results show that a rigorous homogenization model can correctly capture the main physics of the scattering from finite metamaterial objects and lead to large computational saving in the modeling, design and application of metamaterials in realistic devices. Although the metamaterial arrays used to verify the homogeneous theory in this work are composed of magnetodielectric spheres that are used to realize negative index metamaterials in the microwave region, the theory can be directly applied to optical and terahertz frequencies, as long as subwavelength inclusions are considered.

5.2 Scattering from Multilayered Spheres

The calculation of scattering from a sphere composed of layers of arbitrary (complex, positive, negative) refractive index and permeability is important for metamaterials research, in part because arrays of spherical particles are extremely important in fabricating metamaterials, and also because it enables comparison of scattering from a spherical array of particles with scattering from a sphere itself as in Part II above. The focus of the paper [2] resulting from this effort is the Mie series for the scattered field of a layered sphere illuminated by a linearly polarized plane wave. No restrictions are placed on the complex refractive indices and permeabilities of the layers of the sphere. In contrast to the generality of this paper, much of the literature is devoted to either the homogeneous sphere or the sphere with a single coating. In fact, as this paper demonstrates, it is surprisingly simpler and much more elegant to first consider the general problem of scattering from a sphere with any number of layers, and to obtain the solution to scattering from a homogeneous sphere or a sphere with a single coating as special cases. Additionally, unlike this paper, almost all treatments of scattering from a sphere with one or more coatings make the simplifying assumption that the permeabilities of the core, coatings, and medium are equal. Since the current interest in fabricating metamaterials often involves consideration of magnetodielectric inclusions, it is very useful to have expressions in which the permeabilities of the core and coatings appear explicitly as they do in reference [2].

5.2.1   Calculation of Mie Scattering Coefficients

A computable form of the Mie coefficients is derived that uses ratios of spherical Bessel functions only; no logarithmic derivatives are used. Most of the treatments of scattering from a sphere, with or without coatings, make use of logarithmic derivatives of spherical or Riccati-Bessel functions as a way of avoiding the overflow problems involved in calculating spherical Bessel functions with complex arguments. The calculation of logarithmic derivatives is complicated in its own right. In contrast, the analysis of this paper makes no use whatsoever of logarithmic derivatives. All the spherical Bessel functions in this paper appear only in ratios that are well behaved and that are calculated using stable recurrence relations that can be computed easily, rapidly, and extremely accurately. The recursions are initialized by using Steed's algorithm to calculate Lentz' continued fraction expression for the ratio of two Bessel functions, a significant advance compared with other methods that have been used to initialize Bessel

function ratio recursions. The continued fraction representation of the ratio of Bessel functions of adjacent order due to Lentz evaluated by Steed's algorithm is completely straightforward and easily programmed.

The avoidance of logarithmic derivatives is a significant accomplishment in view of the fact that in his fine review article in the Handbook of Optics Volume I (McGraw-Hill, NY, 2010), "Scattering by Particles," Craig Bohren writes "It is not obvious how to write the scattering coefficients for a coated sphere so that only ratios of possibly large quantities are computed explicitly." A related valuable contribution of the paper is the detailed analysis given of the stability properties of the recurrence relations used to calculate these spherical Bessel function ratios. A considerable number of treatments of coated spheres are subject to size limitations, not just of the radii of the sphere layers but of the product of the electrical length of the sphere radii with the complex indices of refraction of the layers. In contrast, the recursion calculations of spherical Bessel function ratios that form the basis of the calculation of Mie coefficients in this paper have no size limitation.

The Mie coefficients of the scattered field are obtained by a recursion process that begins at the core of the sphere and proceeds to the outer boundary of the sphere. The use of spherical Bessel function ratios together with the streamlined notation introduced for the electrical lengths of the radii on the two sides of the interfaces between the layers, make the recursion process for obtaining the scattered field Mie coefficients simpler than other methods for obtaining the Mie coefficients. At first it is assumed that the refractive index and permeability of the medium surrounding the sphere are real (non-absorbing medium), and then it is shown that it is simple to extend the solution to when the refractive index and permeability of the surrounding medium are complex (absorbing medium). Although the paper centers on the scattered field Mie coefficients, it is shown how the Mie coefficients for the fields internal to the sphere can be obtained once the scattered field coefficients are known.

5.2.2 Calculation of the Scattered Far Field Parameters

Once the Mie coefficients are known, the scattered far field components are obtained using angle functions calculated by recurrence relations given in the paper. Parameters of the scattered field such as the polarization, the efficiencies, and the asymmetry parameter, can then be easily calculated. Detailed discussions are given in the paper of a number of important topics related to the scattered field including the extinction, scattered, and absorption efficiencies; the asymmetry parameter; radiation pressure; Rayleigh scattering; the optical theorem; the extinction paradox; the localization principle; scattering from a sphere illuminated by an unpolarized plane wave; the loci of the Mie coefficients in the complex plane; resonances of the Mie coefficients; the Debye series; and the complex-angular-momentum method. The paper also presents a new method for obtaining the field scattered from a layered sphere illuminated by an extended incoherent source like the sun.

5.2.3 Debye Series Expansion of the Mie Coefficients

One of the important limitations of the Mie series representation of the scattered field is that even though it is exact it is not possible in general to obtain any real understanding of what is going on. The Mie series is a kind of "black box." The Debye series, intimately related to the Mie series, can be of much help in understanding the physical basis of the important aspects of electromagnetic scattering since, unlike the Mie series, its coefficients are directly interpretable in terms of external and internal reflections, and surface waves.. A very important contribution of the paper is the derivation given for the coefficients for the Debye series expansion of the Mie coefficients for a homogeneous sphere with arbitrary complex permeability and refractive index, embedded in a medium with arbitrary complex permeability and refractive index, along with computational forms for the Debye coefficients using only Bessel function ratios and no logarithmic derivatives. Both the derivation and the computational forms are simpler and more general than those in the literature. Prior expressions for the Debye coefficients of a homogeneous sphere assume equality of the permeability of the sphere and medium, and computational forms given in the literature are more complicated, use logarithmic derivatives, and assume that the refractive index of the medium is real. The Debye series expansions of the Mie coefficients, derived in the literature assuming equality of real permeability of sphere and medium, are shown to remain valid when these restrictions are removed. The Debye expansions for scattering from a homogeneous sphere can be used as the basis for a simple, easily programmable, recursion procedure for generating the Debye expansions of the Mie coefficients for scattering from a multilayered sphere.

5.2.4 Scattering from Multilayered Spheres: Concluding Discussion

Related to the Debye expansions in attempting to understand the physical basis of scattering is the complex angular momentum theory (CAM) developed largely by the mathematical physicist H. M. Nussenzveig in a book and numerous papers. The CAM is highly mathematical in relying on in-depth analyses in the complex plane, but even though it gives valuable insights into natural phenomena like the rainbow and glory it cannot be extended easily to coated and multilayered spheres. The paper [2] gives an introduction to the CAM.

This paper also contains a detailed discussion, with numerous numerical examples and plots, of morphology-dependent resonances (MDR's) of the Mie coefficients. The resonances play a very important role in determining the rapid oscillations that are often characteristic of the scattered field calculated by the Mie series.

A detailed outline is given in [2] of a computer program that has been written to implement and validate the analysis of the paper. Numerous results obtained with this computer program have been rigorously checked. The basic computer program is extremely flexible and can be easily tailored to fit the interests of the user, as has been done in the course of performing the calculations described in the paper, such as calculating the scattered field as a function of the scattering angle, the efficiencies as a function of the size and refractive indices of the layers, and the locations of the resonances of the Mie coefficients.

In addition to its principal purpose of presenting important original material concerning the calculation of the Mie series and the Debye expansions, the paper, reference [2], also serves as an encyclopedic reference, bringing together in a tutorial fashion material that is spread out over a considerable number of sources in the literature including vector spherical harmonics and multipole expansions; the localization principle; Lentz' continued fraction representation of the ratio of Bessel functions; Steed's algorithm; stability analysis of recursion calculations; extinction, scattering, absorption, and backscatter efficiencies; the optical theorem; the extinction paradox; the asymmetry parameter; radiation pressure; Rayleigh scattering; approximations for the scattered field and efficiencies for large spheres; loci of the Mie scattering coefficients in the complex plane; Mie resonances; the Debye series; and the CAM method; and calls attention of readers to some valuable references with which they may not be familiar.

5.3 References

[1] Xing-Xiang Liu, Jackson W. Massey, Ming-Feng Wu, Kristopher T. Kim, Robert A. Shore, Ali E. Yilmaz, and Andrea Alù, "Homogenization of three-dimensional metamaterial objects and validation by a fast surface-integral equation method." *Optics Express*, 21, No. 18, 9 September 2013.

[2] R. A. Shore, "Scattering of a plane wave from a sphere with multiple layers", paper accepted for publication (2015) in the IEEE Antennas and Propagation Magazine.

5.4 Appendix

1 DERIVATION OF EFFECTIVE BIANISOTROPIC PARAMETERS FOR THREE-DIMENSIONAL PERIODIC ARRAYS AND ARBITRARY $\beta - \omega$.

The derivation follows that of Alù in [1]. The outline of the derivation is as follows. In the first part of the derivation we obtain the equations (10) expressing the relationship between the external fields, $\mathbf{E}_{\text{ext}}$ and $\mathbf{H}_{\text{ext}}$, the average fields, $\mathbf{E}_{\text{av}}$ and $\mathbf{H}_{\text{av}}$, and the average polarization and magnetization, $\mathbf{P}_{\text{av}}$ and $\mathbf{M}_{\text{av}}$. Following this we express $\mathbf{E}_{\text{ext}}$ and $\mathbf{H}_{\text{ext}}$ in terms of $\mathbf{P}_{\text{av}}$, and $\mathbf{M}_{\text{av}}$ leading to (17). Substitution of (17) in (10) then gives (18) expressing $\mathbf{E}_{\text{av}}$ and $\mathbf{H}_{\text{av}}$ in terms of $\mathbf{P}_{\text{av}}$ and $\mathbf{M}_{\text{av}}$. Equations (18) can then be inverted to give $\mathbf{P}_{\text{av}}$ and $\mathbf{M}_{\text{av}}$ in terms of $\mathbf{E}_{\text{av}}$ and $\mathbf{H}_{\text{av}}$. These expressions for $\mathbf{P}_{\text{av}}$ and $\mathbf{M}_{\text{av}}$ along with $\mathbf{E}_{\text{av}}$ and $\mathbf{H}_{\text{av}}$ are then substituted in the bianisotropic constitutive relation equations, (19), which are solved for the effective bianisotropic parameters by equating coefficients of $\mathbf{E}_{\text{av}}$, $\mathbf{H}_{\text{av}}$, and their crossproducts with $\hat{\boldsymbol{\beta}}$.

We assume the presence of impressed electric and magnetic current sources, $\mathbf{J}_{\text{ext}}(\mathbf{r})$ and $\mathbf{K}_{\text{ext}}(\mathbf{r})$, respectively, with the plane-wave dependence $\exp(i\boldsymbol{\beta}\cdot\mathbf{r} - i\omega t)$. The local microscopic fields then satisfy the Maxwell equations

$$\nabla \times \mathbf{E}(\mathbf{r}) = i\omega\mathbf{B}(\mathbf{r}) = i\mu_0[\mathbf{H}(\mathbf{r}) + \mathbf{M}(\mathbf{r})] - \mathbf{K}_{\text{ext}} \tag{1a}$$

$$\nabla \times \mathbf{H}(\mathbf{r}) = -i\omega\mathbf{D}(\mathbf{r}) = -i\omega[\epsilon_0\mathbf{E}(\mathbf{r}) + \mathbf{P}(\mathbf{r})] + \mathbf{J}_{\text{ext}} . \tag{1b}$$

We can also define corresponding impressed fields with the same plane-wave dependence satisfying the Maxwell equations

$$\nabla \times \mathbf{E}_{\text{ext}} = i\omega\mu_0\mathbf{H}_{\text{ext}} - \mathbf{K}_{\text{ext}} \tag{2a}$$

$$\nabla \times \mathbf{H}_{\text{ext}} = -i\omega\epsilon_0\mathbf{E}_{\text{ext}} + \mathbf{J}_{\text{ext}} \tag{2b}$$

or

$$i\boldsymbol{\beta} \times \mathbf{E}_{\text{ext}} = i\omega\mu_0\mathbf{H}_{\text{ext}} - \mathbf{K}_{\text{ext}} \tag{3a}$$

$$i\boldsymbol{\beta} \times \mathbf{H}_{\text{ext}} = -i\omega\epsilon_0\mathbf{E}_{\text{ext}} + \mathbf{J}_{\text{ext}} \tag{3b}$$

We now define quantities averaged over a cubic unit cell with side d as follows:

$$\mathbf{E}_{\text{av}} = \frac{1}{d^3} \int_V \mathbf{E}(\mathbf{r})e^{-i\boldsymbol{\beta}\cdot\mathbf{r}}d\mathbf{r} \tag{4}$$

and similarly for the average of all microscopic quantities. It is assumed that the induced current, magnetization, and polarization vectors are all localized at the center point of the unit cell. If they are not so localized the average must be defined more generally as done by Alù in [1]. The effect of defining the integral with the multiplicative factor $\exp(-i\boldsymbol{\beta}\cdot\mathbf{r})$ is to cancel out the approximate $\exp(i\boldsymbol{\beta}\cdot\mathbf{r})$ resulting from the impressed sources with that spatial dependence in (1). The averaged quantities defined as in (4) are then to be understood as phasors with the implicit plane-wave dependence $\exp(i\boldsymbol{\beta}\cdot\mathbf{r} - \omega t)$. From (1) we then obtain

$$i\boldsymbol{\beta} \times \mathbf{E}_{\text{av}} = i\omega\mu_0(\mathbf{H}_{\text{av}} + \mathbf{M}_{\text{av}}) - \mathbf{K}_{\text{ext}} \tag{5a}$$

$$i\boldsymbol{\beta} \times \mathbf{H}_{\mathrm{av}} = -i\omega(\epsilon_0 \mathbf{E}_{\mathrm{av}} + \mathbf{P}_{\mathrm{av}}) + \mathbf{J}_{\mathrm{ext}} \ . \tag{5b}$$

or equivalently with $\mathbf{D}_{\mathrm{av}} = \epsilon_0 \mathbf{E}_{\mathrm{av}} + \mathbf{P}_{\mathrm{av}}$ and $\mathbf{B}_{\mathrm{av}} = \mu_0(\mathbf{H}_{\mathrm{av}} + \mathbf{M}_{\mathrm{av}})$

$$i\boldsymbol{\beta} \times \mathbf{E}_{\mathrm{av}} = i\omega \mathbf{B}_{\mathrm{av}} - \mathbf{K}_{\mathrm{ext}} \tag{6a}$$

$$i\boldsymbol{\beta} \times \mathbf{H}_{\mathrm{av}} = -i\omega \mathbf{D}_{\mathrm{av}} + \mathbf{J}_{\mathrm{ext}} \ . \tag{6b}$$

Substituting (2) in (5)

$$i\boldsymbol{\beta} \times \mathbf{E}_{\mathrm{av}} = i\omega\mu_0(\mathbf{H}_{\mathrm{av}} + \mathbf{M}_{\mathrm{av}}) + i\boldsymbol{\beta} \times \mathbf{E}_{\mathrm{ext}} - i\omega\mu_0 \mathbf{H}_{\mathrm{ext}} \tag{7a}$$

$$i\boldsymbol{\beta} \times \mathbf{H}_{\mathrm{av}} = -i\omega(\epsilon_0 \mathbf{E}_{\mathrm{av}} + \mathbf{P}_{\mathrm{av}}) + i\boldsymbol{\beta} \times \mathbf{H}_{\mathrm{ext}} + i\omega\epsilon_0 \mathbf{E}_{\mathrm{ext}} \tag{7b}$$

or

$$i\boldsymbol{\beta} \times (\mathbf{E}_{\mathrm{av}} - \mathbf{E}_{\mathrm{ext}}) = i\omega\mu_0(\mathbf{H}_{\mathrm{av}} - \mathbf{H}_{\mathrm{ext}}) + i\omega\mu_0 \mathbf{M}_{\mathrm{av}} \tag{8a}$$

$$i\boldsymbol{\beta} \times (\mathbf{H}_{\mathrm{av}} - \mathbf{H}_{\mathrm{ext}}) = -i\omega\epsilon_0(\mathbf{E}_{\mathrm{av}} - \mathbf{E}_{\mathrm{ext}}) - i\omega \mathbf{P}_{\mathrm{av}} \tag{8b}$$

Now form the cross product of $i\boldsymbol{\beta}$ with both sides of (8a) and substitute (8b) to obtain

$$[k_0^2 + \boldsymbol{\beta} \times \boldsymbol{\beta} \times](\mathbf{E}_{\mathrm{av}} - \mathbf{E}_{\mathrm{ext}}) = -\frac{k_0^2}{\epsilon_0}\mathbf{P}_{\mathrm{av}} + k_0\eta_0\,\boldsymbol{\beta} \times \mathbf{M}_{\mathrm{av}} \tag{9a}$$

and form the cross product of $i\boldsymbol{\beta}$ with both sides of (8b) and substitute (8a) to obtain

$$[k_0^2 + \boldsymbol{\beta} \times \boldsymbol{\beta} \times](\mathbf{H}_{\mathrm{av}} - \mathbf{H}_{\mathrm{ext}}) = -k_0^2\,\mathbf{M}_{\mathrm{av}} - \frac{k_0}{\eta_0}\boldsymbol{\beta} \times \frac{\mathbf{P}_{\mathrm{av}}}{\epsilon_0} \tag{9b}$$

where $\eta_0 = \sqrt{\mu_0/\epsilon_0}$ is the free-space impedance.

At this point in the derivation we make the simplifying assumption that $\boldsymbol{\beta}$ is orthogonal to $\mathbf{E}_{\mathrm{av}}$ and $\mathbf{E}_{\mathrm{ext}}$, and to $\mathbf{H}_{\mathrm{av}}$ and $\mathbf{H}_{\mathrm{ext}}$. (Note that it follows from this assumption and (8) that $\mathbf{E}_{\mathrm{av}}$, $\mathbf{E}_{\mathrm{ext}}$, and $\mathbf{P}_{\mathrm{av}}$ are orthogonal to $\mathbf{H}_{\mathrm{av}}$, $\mathbf{H}_{\mathrm{ext}}$, and $\mathbf{M}_{\mathrm{av}}$, so that the fields are TEM.) Simplifying the triple cross product and rearranging gives

$$\mathbf{E}_{\mathrm{av}} = \mathbf{E}_{\mathrm{ext}} + \frac{(k_0 d)^2}{(\beta d)^2 - (k_0 d)^2}\frac{\mathbf{P}_{\mathrm{av}}}{\epsilon_0} - \frac{(\beta d)(k_0 d)}{(\beta d)^2 - (k_0 d)^2}\,\eta_0\,\hat{\boldsymbol{\beta}} \times \mathbf{M}_{\mathrm{av}} \tag{10a}$$

and

$$\mathbf{H}_{\mathrm{av}} = \mathbf{H}_{\mathrm{ext}} + \frac{(k_0 d)^2}{(\beta d)^2 - (k_0 d)^2}\mathbf{M}_{\mathrm{av}} + \frac{(\beta d)(k_0 d)}{(\beta d)^2 - (k_0 d)^2}\frac{1}{\eta_0}\,\hat{\boldsymbol{\beta}} \times \frac{\mathbf{P}_{\mathrm{av}}}{\epsilon_0} \tag{10b}$$

We now express the external fields in terms of the average polarization and magnetization, $\mathbf{P}_{\mathrm{av}}$ and $\mathbf{M}_{\mathrm{av}}$. Since both $\mathbf{P}_{\mathrm{av}}$ and $\mathbf{M}_{\mathrm{av}}$ are phasors with the implicit plane-wave dependence $\exp(i\boldsymbol{\beta} \cdot \mathbf{r} - i\omega t)$, they are both given by their values for the unit cell centered at the origin. Let $\mathbf{p}_0$ and $\mathbf{m}_0$ be the electric and magnetic dipole moments, respectively, of the electric and magnetic dipoles at the origin so that

$$\mathbf{P}_{\mathrm{av}} = \frac{1}{d^3}\mathbf{p}_0 \tag{11a}$$

and

$$\mathbf{M}_{\mathrm{av}} = \frac{1}{d^3}\mathbf{m}_0 \ . \tag{11b}$$

114

Referring to [1, (79)] and using (11)

$$\frac{\mathbf{P}_{\text{av}}}{\epsilon_0} = -\frac{6\pi i b_1^{\text{sc}}}{(k_0 d)^3} \mathbf{E}_0 \qquad (12\text{a})$$

and similarly

$$\mathbf{M}_{\text{av}} = -\frac{6\pi i a_1}{(k_0 d)^3} \mathbf{H}_0 \qquad (12\text{b})$$

where b_1^{sc} and a_1^{sc} are the Mie electric and magnetic dipole scatering coefficients,respectively, and $\mathbf{E}_0$ and $\mathbf{H}_0$ are the electric and magnetic fields at the origin in the direction of the electric and magnetic dipoles, respectively. Furthermore,

$$\mathbf{E}_0 = \mathbf{E}_{\text{loc},0} + \mathbf{E}_{\text{ext}} \qquad (13\text{a})$$

and

$$\mathbf{H}_0 = \mathbf{H}_{\text{loc},0} + \mathbf{H}_{\text{ext}} \qquad (13\text{b})$$

where $\mathbf{E}_{\text{loc},0}$ and $\mathbf{H}_{\text{loc},0}$ are the local electric and magnetic fields at the origin, respectively, due to the contributions of all the dipoles of the array, electric and magnetic, both of which contribute to both $\mathbf{E}_{\text{loc},0}$ and $\mathbf{H}_{\text{loc},0}$. Referring to [1, sec. 3.1],

$$\mathbf{E}_{\text{loc},0} = \frac{k_0^3}{4\pi} \frac{\Sigma_1}{(k_0 d)^3} \frac{\mathbf{p}_0}{\epsilon_0} + \eta_0 \frac{k_0^3}{4\pi} \frac{\Sigma_2}{(k_0 d)^3} \hat{\boldsymbol{\beta}} \times \mathbf{m}_0 \qquad (14\text{a})$$

and

$$\mathbf{H}_{\text{loc},0} = \frac{k_0^3}{4\pi} \frac{\Sigma_1}{(k_0 d)^3} \mathbf{m}_0 - \frac{1}{\eta_0} \frac{k_0^3}{4\pi} \frac{\Sigma_2}{(k_0 d)^3} \hat{\boldsymbol{\beta}} \times \frac{\mathbf{p}_0}{\epsilon_0} \qquad (14\text{b})$$

where the interaction constant summations Σ_1 and Σ_2 are given by (46) and (47) derived in [2][1] so that with (11)

$$\mathbf{E}_{\text{loc},0} = \frac{\Sigma_1}{4\pi} \frac{\mathbf{P}_{\text{av}}}{\epsilon_0} + \eta_0 \frac{\Sigma_2}{4\pi} \hat{\boldsymbol{\beta}} \times \mathbf{M}_{\text{av}} \qquad (15\text{a})$$

and

$$\mathbf{H}_{\text{loc},0} = \frac{\Sigma_1}{4\pi} \mathbf{M}_{\text{av}} - \frac{1}{\eta_0} \frac{\Sigma_2}{4\pi} \hat{\boldsymbol{\beta}} \times \frac{\mathbf{P}_{\text{av}}}{\epsilon_0} . \qquad (15\text{b})$$

Combining (15) with (12) and (13)

$$\frac{\mathbf{P}_{\text{av}}}{\epsilon_0} = -\frac{6\pi i b_1^{\text{sc}}}{(k_0 d)^3} \left[\frac{\Sigma_1}{4\pi} \frac{\mathbf{P}_{\text{av}}}{\epsilon_0} + \eta_0 \frac{\Sigma_2}{4\pi} \hat{\boldsymbol{\beta}} \times \mathbf{M}_{\text{av}} + \mathbf{E}_{\text{ext}} \right] \qquad (16\text{a})$$

and

$$\mathbf{M}_{\text{av}} = -\frac{6\pi i a_1^{\text{sc}}}{(k_0 d)^3} \left[\frac{\Sigma_1}{4\pi} \mathbf{M}_{\text{av}} - \frac{1}{\eta_0} \frac{\Sigma_2}{4\pi} \hat{\boldsymbol{\beta}} \times \frac{\mathbf{P}_{\text{av}}}{\epsilon_0} + \mathbf{H}_{\text{ext}} \right] . \qquad (16\text{b})$$

---

[1] Although Σ_1 and Σ_2 are obtained in [2] in the course of deriving the eigenmode dispersion equation, they are valid for any values of βd and $k_0 d$, whether or not βd and $k_0 d$ are related by the eigenmode dispersion equation.

Solving (16) for $\mathbf{E}_{\text{ext}}$ and $\mathbf{H}_{\text{ext}}$

$$\mathbf{E}_{\text{ext}} = \left[-\frac{(k_0 d)^3}{6\pi i b_1^{\text{sc}}} - \frac{\Sigma_1}{4\pi} \right] \frac{\mathbf{P}_{\text{av}}}{\epsilon_0} - \eta_0 \frac{\Sigma_2}{4\pi} \hat{\boldsymbol{\beta}} \times \mathbf{M}_{\text{av}} \tag{17a}$$

and

$$\mathbf{H}_{\text{ext}} = \left[-\frac{(k_0 d)^3}{6\pi i a_1^{\text{sc}}} - \frac{\Sigma_1}{4\pi} \right] \mathbf{M}_{\text{av}} + \frac{1}{\eta_0} \frac{\Sigma_2}{4\pi} \hat{\boldsymbol{\beta}} \times \frac{\mathbf{P}_{\text{av}}}{\epsilon_0} \,. \tag{17b}$$

Substituting (17) in (10) we obtain

$$\mathbf{E}_{\text{av}} = \left[-\frac{(k_0 d)^3}{6\pi i b_1^{\text{sc}}} - \frac{\Sigma_1}{4\pi} + \frac{(k_0 d)^2}{(\beta d)^2 - (k_0 d)^2} \right] \frac{\mathbf{P}_{\text{av}}}{\epsilon_0} - \left[\frac{\Sigma_2}{4\pi} + \frac{(\beta d)(k_0 d)}{(\beta d)^2 - (k_0 d)^2} \right] \eta_0 \hat{\boldsymbol{\beta}} \times \mathbf{M}_{\text{av}} \tag{18a}$$

and

$$\mathbf{H}_{\text{av}} = \left[-\frac{(k_0 d)^3}{6\pi i a_1^{\text{sc}}} - \frac{\Sigma_1}{4\pi} + \frac{(k_0 d)^2}{(\beta d)^2 - (k_0 d)^2} \right] \mathbf{M}_{\text{av}} + \left[\frac{\Sigma_2}{4\pi} + \frac{(\beta d)(k_0 d)}{(\beta d)^2 - (k_0 d)^2} \right] \frac{1}{\eta_0} \hat{\boldsymbol{\beta}} \times \frac{\mathbf{P}_{\text{av}}}{\epsilon_0} \,. \tag{18b}$$

Next, form the cross products of $\hat{\boldsymbol{\beta}}$ with the left and right sides of (18a) and (18b), simplify the triple cross products, and solve for $\mathbf{P}_{\text{av}}$ in terms of $\mathbf{E}_{\text{av}}$ and $\hat{\boldsymbol{\beta}} \times \mathbf{H}_{\text{av}}$, and for $\mathbf{M}_{\text{av}}$ in terms of $\mathbf{H}_{\text{av}}$ and $\hat{\boldsymbol{\beta}} \times \mathbf{E}_{\text{av}}$, and then substitute these expressions for $\mathbf{P}_{\text{av}}$ and $\mathbf{M}_{\text{av}}$ along with $\mathbf{E}_{\text{av}}$ and $\mathbf{H}_{\text{av}}$ in the following constitutive equations defining the form of the bianisotropic effective parameters:

$$\mathbf{D}_{\text{av}} = \epsilon_0 \mathbf{E}_{\text{av}} + \mathbf{P}_{\text{av}} = \epsilon_{\text{eff}} \mathbf{E}_{\text{av}} - \chi_{\text{eff}} \hat{\boldsymbol{\beta}} \times \mathbf{H}_{\text{av}} \tag{19a}$$

$$\mathbf{B}_{\text{av}} = \mu_0 (\mathbf{H}_{\text{av}} + \mathbf{M}_{\text{av}}) = \mu_{\text{eff}} \mathbf{H}_{\text{av}} + \chi_{\text{eff}} \hat{\boldsymbol{\beta}} \times \mathbf{E}_{\text{av}} \,. \tag{19b}$$

The resulting (19a) is then of the form $A\,\mathbf{E}_{\text{av}} + B\,\hat{\boldsymbol{\beta}} \times \mathbf{H}_{\text{av}} = 0$ so that both A and B equal zero since the equation holds for all $\mathbf{E}_{\text{av}}$ and $\hat{\boldsymbol{\beta}} \times \mathbf{H}_{\text{av}}$. Similarly, the resulting (19b) is then of the form $C\,\mathbf{H}_{\text{av}} + D\,\hat{\boldsymbol{\beta}} \times \mathbf{E}_{\text{av}} = 0$ so that both C and D equal zero since the equation holds for all $\mathbf{H}_{\text{av}}$ and $\hat{\boldsymbol{\beta}} \times \mathbf{E}_{\text{av}}$. These four relations yield, after some algebra, the following expressions for the three bianisotropic effective relative parameters, valid for arbitrary β and ω:

$$\epsilon_{\text{r,eff}} \equiv \epsilon_{\text{eff}}/\epsilon_0 = 1 + \frac{a}{ab - c^2} \tag{20a}$$

$$\mu_{\text{r,eff}} \equiv \mu_{\text{eff}}/\mu_0 = 1 + \frac{b}{ab - c^2} \tag{20b}$$

and

$$c_0 \chi_{\text{eff}} = \frac{c}{ab - c^2} \tag{20c}$$

where

$$a = -\frac{(k_0 d)^3}{6\pi i a_1^{\text{sc}}} - \frac{\Sigma_1}{4\pi} + \frac{(k_0 d)^2}{(\beta d)^2 - (k_0 d)^2} \tag{21a}$$

$$b = -\frac{(k_0 d)^3}{6\pi i b_1^{\text{sc}}} - \frac{\Sigma_1}{4\pi} + \frac{(k_0 d)^2}{(\beta d)^2 - (k_0 d)^2} \tag{21b}$$

116

and

$$c = -\frac{\Sigma_2}{4\pi} - \frac{(\beta d)(k_0 d}{(\beta d)^2 - (k_0 d)^2} \ . \tag{21c}$$

It is important to note that all the basic equations of this derivation, in particular (18) and (19) leading to the expressions (20) and (21) for the bianisotropic effective parameters, are valid even when the external sources and fields are zero. Thus (20) and (21) give the bian-isotropic effective parameters not only for arbitrary $\beta - \omega$ but for the source-free eigenmode case as well. There is, however, one essential difference between the arbitrary $\beta - \omega$ bian-isotropic parameters and the source-free eigenmode bianisotropic parameters. For arbitrary $\beta - \omega$, β and k_0 that appear explicitly in (21) as well as in the interaction summations Σ_1 and Σ_2 given by (46) and (47), are completely independent of one another, and the bianisotropic effective parameter expressions are valid for any β and any k_0. In the source-free eigenmode case, however, β and k_0 are not independent but must be related by the dispersion equation (25). In the next section we will see that when explicit use is made of the dispersion equation the expressions for the bianisotropic effective parameters become much simpler.

2 BIANISOTROPIC PARAMETERS FOR THREE-DIMENSIONAL PERIODIC ARRAYS WITH βd THE SOLUTION OF THE SOURCE-FREE DISPERSION EQUATION

In this section we show that the expressions (20) and (21) for the arbitrary $\beta - \omega$ bianisotropic effective relative parameters obtained in Section 1 take a much simpler form in the eigenmode case when βd and $k_0 d$ are related by the source-free dispersion equation. We first write the expressions (21) in the form

$$a = \frac{1}{4\pi} \frac{(k_0 d)^3 - S_m \Sigma_1}{S_m} + \frac{1}{\mathcal{R}^2 - 1} \tag{22a}$$

$$b = \frac{1}{4\pi} \frac{(k_0 d)^3 - S_e \Sigma_1}{S_m} + \frac{1}{\mathcal{R}^2 - 1} \tag{22b}$$

and

$$c = -\frac{\Sigma_2}{4\pi} - \frac{\mathcal{R}}{\mathcal{R}^2 - 1} \tag{22c}$$

where

$$S_m = -\frac{3}{2} i\, a_1^{sc} \tag{23a}$$

$$S_e = -\frac{3}{2} i\, b_1^{sc} \tag{23b}$$

and

$$\mathcal{R} = \frac{\beta d}{k_0 d} \ . \tag{24}$$

From [1, (53)], the dispersion equation for the eigenmode case is

$$-q = \frac{(k_0 d)^3 - S_e \Sigma_1}{S_e \Sigma_2} = \frac{S_m \Sigma_2}{(k_0 d)^3 - S_m \Sigma_1} \ . \tag{25}$$

so that

$$(k_0 d)^3 - S_e \Sigma_1 = -q S_e \Sigma_2 \tag{26a}$$

and

$$(k_0 d)^3 - S_m \Sigma_1 = -\frac{S_m \Sigma_2}{q} \ . \tag{26b}$$

Substituting (26) in (22) gives

$$a = -\frac{\Sigma_2}{4\pi q} + \frac{1}{\mathcal{R}^2 - 1} \tag{27a}$$

$$b = -\frac{q \Sigma_2}{4\pi} + \frac{1}{\mathcal{R}^2 - 1} \tag{27b}$$

and

$$c = -\frac{\Sigma_2}{4\pi} - \frac{\mathcal{R}}{\mathcal{R}^2 - 1} \ . \tag{27c}$$

so that

$$ab - c^2 = -\frac{1}{(\mathcal{R}^2 - 1)q} \left[q + \frac{\Sigma_2}{4\pi} \left(q^2 + 1 + 2q\mathcal{R} \right) \right] . \tag{28}$$

Substitution of (27) and (28) in (20) then gives the expressions for the bianisotropic relative effective parameters in the eigenmode case:

$$\epsilon_{r,eff} \equiv \epsilon_{eff}/\epsilon_0 = \frac{\dfrac{\Sigma_2}{4\pi}(\mathcal{R} + q)^2}{\dfrac{\Sigma_2}{4\pi}[(\mathcal{R} + q)^2 - (\mathcal{R}^2 - 1)] + q} \tag{29a}$$

$$\mu_{r,eff} \equiv \mu_{eff}/\mu_0 = \frac{\dfrac{\Sigma_2}{4\pi}(1 + \mathcal{R}q)^2}{\dfrac{\Sigma_2}{4\pi}[(\mathcal{R} + q)^2 - (\mathcal{R}^2 - 1)] + q} \tag{29b}$$

$$c_0 \chi_{eff} = \frac{q \left[\dfrac{\Sigma_2}{4\pi}(\mathcal{R}^2 - 1) + \mathcal{R}) \right]}{\dfrac{\Sigma_2}{4\pi}[(\mathcal{R} + q)^2 - (\mathcal{R}^2 - 1)] + q} \tag{29c}$$

and

$$1 - \frac{c_0 \chi_{eff}}{\mathcal{R}} = \frac{\dfrac{1}{\mathcal{R}} \dfrac{\Sigma_2}{4\pi}(\mathcal{R} + q)(1 + \mathcal{R}q)}{\dfrac{\Sigma_2}{4\pi}[(\mathcal{R} + q)^2 - (\mathcal{R}^2 - 1)] + q} \tag{29d}$$

where (29d) will be used in the sequel. Alternatively, (29a) and (29b) can be written in the form

$$\frac{\epsilon_{eff}}{\epsilon_0} - 1 = \frac{\dfrac{\Sigma_2}{4\pi}(\mathcal{R}^2 - 1) - q}{\dfrac{\Sigma_2}{4\pi}[(\mathcal{R} + q)^2 - (\mathcal{R}^2 - 1)] + q} \tag{30a}$$

118

and

$$\frac{\mu_{\text{eff}}}{\mu_0} - 1 = \frac{\dfrac{\Sigma_2}{4\pi}q^2(\mathcal{R}^2 - 1) - q}{\dfrac{\Sigma_2}{4\pi}[(\mathcal{R} + q)^2 - (\mathcal{R}^2 - 1)] + q} \tag{30b}$$

3 ANISOTROPIC RELATIVE PARAMETERS FOR PERIODIC ARRAY IN THE EIGENMODE CASE

In this section we show that in the eigenmode case, the three bianisotropic effective parameters given by (29) in Section 2 are equivalent to the two anisotropic effective parameters given by [2, (68)]. To show this, substitute the second bianisotropic constitutive equation, (19b), in the source-free Maxwell equation (see (6a) with $\mathbf{K}_{\text{ext}} = 0$)

$$\nabla \times \mathbf{E}_{\text{av}} = -\frac{\partial \mathbf{B}_{\text{av}}}{\partial t} = i\omega \mathbf{B}_{\text{av}} \tag{31}$$

to obtain

$$\nabla \times \mathbf{E}_{\text{av}} = i\boldsymbol{\beta} \times \mathbf{E}_{\text{av}} = i\omega\mu_0\mu_{\text{r,eff}}\mathbf{H}_{\text{av}} + \frac{i\omega\chi_{\text{eff}}}{i\beta}i\boldsymbol{\beta} \times \mathbf{E}_{\text{av}} \tag{32}$$

from which we obtain

$$\nabla \times \mathbf{E}_{\text{av}} = i\boldsymbol{\beta} \times \mathbf{E}_{\text{av}} = i\omega\mu_0\frac{\mu_{\text{r,eff}}}{1 - \frac{c_0\chi_{\text{eff}}}{\mathcal{R}}}\mathbf{H}_{\text{av}}. \tag{33}$$

Then, with (29)

$$\nabla \times \mathbf{E}_{\text{av}} = i\boldsymbol{\beta} \times \mathbf{E}_{\text{av}} = i\omega\mu_0\mu_{\text{r,a}}\mathbf{E}_{\text{av}} \tag{34}$$

where the effective anisotropic relative permeability, denoted by $\mu_{\text{r,a}}$, is given by

$$\mu_{\text{r,a}} = \frac{\mu_{\text{r,eff}}}{1 - \frac{c_0\chi_{\text{eff}}}{\mathcal{R}}} = \frac{\mathcal{R}(1 + \mathcal{R}\,q)}{\mathcal{R} + q} \tag{35}$$

in agreement with [1, (68)].

Similarly, substitute the first bianisotropic constitutive equation, (19a), in the source-free Maxwell equation (see (6b) with $\mathbf{J}_{\text{ext}} = 0$)

$$\nabla \times \mathbf{H}_{\text{av}} = \frac{\partial \mathbf{D}_{\text{av}}}{\partial t} = -i\omega \mathbf{D}_{\text{av}} \tag{36}$$

to obtain

$$\nabla \times \mathbf{H}_{\text{av}} = i\boldsymbol{\beta} \times \mathbf{H}_{\text{av}} = -i\omega\epsilon_0\epsilon_{\text{r,eff}}\mathbf{E}_{\text{av}} - \frac{i\omega\chi_{\text{eff}}}{i\beta}i\boldsymbol{\beta} \times \mathbf{H}_{\text{av}} \tag{37}$$

from which we obtain

$$\nabla \times \mathbf{H}_{\text{av}} = i\boldsymbol{\beta} \times \mathbf{H}_{\text{av}} = -i\omega\epsilon_0\frac{\epsilon_{\text{r,eff}}}{1 - \frac{c_0\chi_{\text{eff}}}{\mathcal{R}}}\mathbf{H}_{\text{av}}. \tag{38}$$

Then, with (29)

$$\nabla \times \mathbf{H}_{\mathrm{av}} = \mathrm{i}\boldsymbol{\beta} \times \mathbf{H}_{\mathrm{av}} = -\mathrm{i}\omega\epsilon_0\epsilon_{\mathrm{r,a}}\,\mathbf{H}_{\mathrm{av}} \tag{39}$$

where the effective anisotropic relative permittivity, denoted by $\epsilon_{\mathrm{r,a}}$, is given by

$$\epsilon_{\mathrm{r,a}} = \frac{\epsilon_{\mathrm{r,eff}}}{1 - \frac{c_0\chi_{\mathrm{eff}}}{\mathcal{R}}} = \frac{\mathcal{R}(\mathcal{R}+q)}{1+\mathcal{R}\,q} \tag{40}$$

in agreement with [1, (68)].

4 A RELATION BETWEEN THE BIANISOTROPIC AND ANISOTROPIC RELATIVE PARAMETERS FOR PERIODIC ARRAY IN THE EIGENMODE CASE

In this section we derive a relation between the anisotropic and bianisotropic effective parameters in the eigenmode case. First, equate the anisotropic and bianisotropic expressions for $\mathbf{M}_{\mathrm{av}}$ (see [1, (59)] and (19)):

$$\mathbf{M}_{\mathrm{av}} = (\mu_{\mathrm{r,a}} - 1)\mathbf{H}_{\mathrm{av}} = (\mu_{\mathrm{r,b}} - 1)\mathbf{H}_{\mathrm{av}} + \frac{c_0\chi_{\mathrm{b}}}{c_0\mu_0}\hat{\boldsymbol{\beta}} \times \mathbf{E}_{\mathrm{av}} \tag{41}$$

where we have let $\mu_{\mathrm{r,b}} = \mu_{\mathrm{r,eff}}$ and $\chi_{\mathrm{b}} = \chi_{\mathrm{eff}}$. Similarly, equate the anisotropic and bianisotropic expressions for $\mathbf{P}_{\mathrm{av}}$:

$$P_{\mathrm{av}} = (\epsilon_{\mathrm{r,a}} - 1)\epsilon_0\mathbf{E}_{\mathrm{av}} = (\epsilon_{\mathrm{r,b}} - 1)\epsilon_0\mathbf{E}_{\mathrm{av}} - \frac{c_0\chi_{\mathrm{b}}}{c_0}\hat{\boldsymbol{\beta}} \times \mathbf{H}_{\mathrm{av}} \tag{42}$$

where we have let $\epsilon_{\mathrm{r,b}} = \epsilon_{\mathrm{r,eff}}$. From (41)

$$(\mu_{\mathrm{r,a}} - \mu_{\mathrm{r,b}})\hat{\boldsymbol{\beta}} \times \mathbf{H}_{\mathrm{av}} = -\frac{c_0\chi_{\mathrm{b}}}{c_0\mu_0}\mathbf{E}_{\mathrm{av}} \tag{43}$$

so that from (42) and (43)

$$(\epsilon_{\mathrm{r,a}} - \epsilon_{\mathrm{r,b}})\epsilon_0\mathbf{E}_{\mathrm{av}} = -\frac{c_0\chi_{\mathrm{b}}}{c_0}\left[-\frac{c_0\chi_{\mathrm{b}}}{c_0\mu_0}\frac{1}{\mu_{\mathrm{r,a}} - \mu_{\mathrm{r,b}}}\right]\mathbf{E}_{\mathrm{av}}\,. \tag{44}$$

But then

$$(\epsilon_{\mathrm{r,a}} - \epsilon_{\mathrm{r,b}})(\mu_{\mathrm{r,a}} - \mu_{\mathrm{r,b}}) = \frac{(c_0\chi_{\mathrm{b}})^2}{c_0^2\epsilon_0\mu_0} = (c_0\chi_{\mathrm{b}})^2\,. \tag{45}$$

Equation (42) shows that in the eigenmode case the bianisotropic parameter χ is a measure of the difference between the anisotropic and bianisotropic effective permittivity and permeability.

5 EXPRESSIONS FOR INTERACTION CONSTANT SUMMATIONS

From [2, (47),(48)]

$$\Sigma_1 = -2\pi k_0 d \, \frac{\sin k_0 d}{\cos \beta d - \cos k_0 d}$$

$$-4\pi \sum_{n=1}^{\infty} \cos(n\beta d) \sum_{\substack{m=-\infty \\ (m,l) \,\neq\, (0,0)}}^{\infty} \sum_{l=-\infty}^{\infty} \left[(2\pi m)^2 - (k_0 d)^2\right] \frac{\mathrm{e}^{-n\sqrt{(2\pi)^2(m^2+l^2)-(k_0 d)^2}}}{\sqrt{(2\pi)^2(m^2+l^2)-(k_0 d)^2}}$$

$$-2\pi(k_0 d)^2 \sum_{l=1}^{\infty} Y_0(l\,k_0 d) - 8 \sum_{l=1}^{\infty} \sum_{m=1}^{\infty} \left[(2\pi m)^2 - (k_0 d)^2\right] K_0\left(l\sqrt{(2\pi m)^2 - (k_0 d)^2}\right)$$

$$+ 4\,k_0 d\,\mathrm{Cl}_2(k_0 d) + 4\,\mathrm{Cl}_3(k_0 d) - \mathrm{i}\frac{2}{3}(k_0 d)^3 \tag{46}$$

and

$$\Sigma_2 = 2\pi\,k_0 d\,\frac{\sin\beta d}{\cos\beta d - \cos k_0 d}$$

$$-4\pi\,k_0 d \sum_{n=1}^{\infty} \sin(n\beta d) \sum_{\substack{m=-\infty \\ (m,l)\,\neq\,(0,0)}}^{\infty} \sum_{l=-\infty}^{\infty} \mathrm{e}^{-n\sqrt{(2\pi)^2(m^2+l^2)-(k_0 d)^2}} \,. \tag{47}$$

In (46) Y_0 is the Bessel function of the second kind and K_0 is the modified Bessel function. The Clausen functions $\mathrm{Cl}_2(k_0 d)$ and $\mathrm{Cl}_3(k_0 d)$ are defined and given by [3]

$$\mathrm{Cl}_2(a) \equiv \sum_{n=1}^{\infty} \frac{\sin na}{n^2} = \frac{1}{2\mathrm{i}}\left(\mathrm{Li}_2(\mathrm{e}^{\mathrm{i}a}) - \mathrm{Li}_2(\mathrm{e}^{-\mathrm{i}a})\right), \quad 0 < a \le \pi \tag{48a}$$

$$\mathrm{Cl}_2(a) = -\mathrm{Cl}_2(2\pi - a), \quad \pi \le a < 2\pi \tag{48b}$$

$$\mathrm{Cl}_3(a) \equiv \sum_{n=1}^{\infty} \frac{\cos na}{n^3} = \frac{1}{2}\left(\mathrm{Li}_3(\mathrm{e}^{\mathrm{i}a}) + \mathrm{Li}_3(\mathrm{e}^{-\mathrm{i}a})\right), \quad 0 < a < \pi \tag{48c}$$

$$\mathrm{Cl}_3(a) = \mathrm{Cl}_3(2\pi - a), \quad \pi \le a < 2\pi \tag{48d}$$

with the dilogarithm and trilogarithm functions, Li_2 and Li_3, given by

$$\mathrm{Li}_N(z) = \sum_{k=1}^{\infty} \frac{z^k}{k^N}, \quad |z| < 1 \tag{49}$$

which can be analytically continued into the complex z plane by means of the iterative equations

$$\mathrm{Li}_N(z) = \int_0^z \frac{\mathrm{Li}_{N-1}(t)}{t}\mathrm{d}t \tag{50a}$$

and

$$\text{Li}_1(z) = -\ln(1-z) \ . \tag{50b}$$

Efficient algorithms exist for calculating $\text{Li}_N(z)$ for any z, real or complex (see, for example, [4]). The series $\Sigma Y_0(lk_0d)$ in Σ_1 is evaluated by [5, eq. 8.522(3)]

$$\sum_{l=1}^{\infty} Y_0(lk_0d) = -\frac{1}{\pi}\left(\gamma + \ln\frac{k_0d}{4\pi}\right) - 2\sum_{l=1}^{\infty}\left[\frac{1}{\sqrt{(2\pi l)^2 - (k_0d)^2}} - \frac{1}{2\pi l}\right], \ 0 < k_0d < 2\pi \tag{51}$$

with γ the Euler constant

$$\gamma = 0.5772156649\cdots \ . \tag{52}$$

Truncating the series on the RHS of (51) at $l = 10$ gives sufficient accuracy for our purposes.

6   REFERENCES

[1] A. Alù, "Extended homogenization theory for magnetodielectric arrays in presence of external sources," draft-paper, 2010.

[2] R.A. Shore and A.D. Yaghjian, "Traveling waves on two- and three-dimensional periodic arrays of lossless scatterers," *Radio Sci.*, 42, RS6S21, doi:10.1029/2007RS003647 19 December, 2007.

[3] L. Lewin, *Polylogarithms and Associated Functions*, New York: Elsevier North Holland, 1981.

[4] R.E. Crandall, "Note on fast polylogarithm computation," PDF file http://people.reed.edu/~crandall/papers/Polylog.pdf, 2006.

[5] I.S. Gradshteyn and I.M. Ryzhik, *Table of Integrals, Series, and Products; 6th edition*, Boston: Academic Press, 1994.

6. Quantization Lobe Suppression for Arrays of Subarrays

Robert J. Mailloux

6.1 Introduction

Wideband, multifunction phased array antennas are a key element of future defense strategies for providing the warfighter with situational awareness, capable weapons, C4ISR systems and enhanced ESM capabilities. Such advanced array antennas are expensive and a challenge to the state of today's technology. Cost reduction techniques are based on reducing the number of array elements and/or controls by tailoring the array specifically to the application whenever this can be done. This cost reduction invariably causes increased sidelobes in the radiation pattern. The work during this grant contract presented three approaches to reduce the pattern distortion caused by these techniques.

Certain large arrays with special requirements can be too costly to build by conventional means. These include 'Limited field of view'(LFOV) arrays that need only scan over a small sector (±10 degrees or so), and wide band arrays that require time delay scanning. For arrays that scan only a limited field of view it is possible to group a number of elements into subarrays and use a single phase shifter for each subarray. Similarly, wide band arrays can operate with fewer time delay units by grouping elements into subarrays controlled by phase shifters, and use time delay units at the input to each subarray. Unfortunately either action causes increased sidelobes, called quantization lobes, and in the LFOV case, may reduce system bandwidth.

Since quantization lobes are caused by the array periodicity, there are only two ways to reduce them. One can destroy the periodicity, or suppress the lobes using some sort of angular filter.

6.2 Polyomino Subarraying for Two Dimensional Arrays

Studies conducted during this contract period included three main topics related to improving the radiation characteristics of arrays with a reduced number of elements or element controls. A solution to the quantization lobe problem for a two dimensional aperture array has been to use irregular shaped polyomino subarrays instead of the usual rectangular subarrays (1,2). Most of our studies of wide band arrays dealt with eight element subarrays that use 1/8 the number of time delay units, but we have also studied 4 and 16 element subarrays. This method has advantages over the several newly proposed uses of classic tilings such as Penrose, Danzer , Pinwheel or other complex lattices as array subarrays (3,4) in that with polyomino subarrays one can use a single type of subarray in an array, and these can be arranged to completely tile the surface, leaving neither gaps nor overlapped areas. This means that the polyomino based array can have full gain and no sidelobe growth at center frequency. A further disadvantage of the classic tiles is that they have higher order periodicities that limit their use for low sidelobe arrays (4). That issue has not been addressed in publications.

The first part of our program extended the previous work on irregular subarrays made of polyomino tiles, and analyzed the mutual interaction of array elements subject to tile groupings. The analysis used an impedance matrix and scattering matrix model to evaluate the substantial

error in the induced currents at the array elements and its resulting radiation pattern sidelobes. The array network model was then used to evaluate new sets of driving voltages that compensated for the distortion and led to the predicted low sidelobe patterns. This work was published in the Antennas and Wireless Propagation Letters (7). Other extensions of the polyomino studies were done in collaboration with Professor Rocca and colleagues from the University of Tento (8), who used our work and our software as the basis for an optimization program using genetic algorithms. This method did produce further reductions in sidelobe patterns and showed the potential of our approach to eliminate quantization lobes while obtaining nearly full array gain.

Our irregular polyomino studies have been well received, and led to the co-organization and co-chairing of a special session on arrays with irregular lattices and overlapped subarrays at the IEEE 2010 International Symposium on Phased Arrays, an invitation to co-edit a special edition of the AP-S Transactions on " Innovative Phased Array Antennas Based on Non-Regular Lattices and Overlapped Subarrays"(9) in April 2014 (with Giovanni Toso of European Space Agency), and further collaboration with researchers at Univ. of Trento(10) and the University of Pittsburgh.

6.3 Column Displacement in Arrays with One Plane of Limited Scan

The second major effort arose in response to the AFRL Sensor Division multifunction array project, wherein the group, headed by Dr. Tomasic had proposed an array with limited elevation scan and wide azimuth scan. To build a cost-effective array the group chose to have elevation columns arranged in subarrays with no phase shifters across each subarray but using time delays at each subarray input. The result was to produce very large elevation sidelobes for all but a few degrees of elevation scan. To avoid this problem we proposed to study random displacements of the columns in order to break up the periodicity that led to quantization lobes. The technique was successful and we were able to demonstrate from 12 to 16 dB reduction in sidelobes, depending upon array size and configuration. We also explored all other array parameters, and presented tabulated data showing trends as a function or scan limits and array dimensions in both planes. We then conducted a study of the wide-band properties of arrays with displaced columns and proved for the first time that the technique imposed no additional bandwidth constraints. The bandwidth properties of this procedure are included in a paper that will be presented at the 2015 IEEE International Symposium on Antennas and Propagation (11).

6.4 Array Element Pattern Control with Layered Dielectric Filters for LFOV Arrays

Arrays that scan over a limited sector of space $|\theta_{max}| \leq 10\,°$or so, can achieve significant cost savings by spacing the elements further apart than a half wavelength, the normal spacing for wide scan arrays. This results in unwanted diffraction peaks, called grating lobes that can radiate within the scan plane. In addition to the other ways to suppress these lobes, one can build rejection filters from multiple layers of dielectric as a radome in front of the array.

This effort arose partly to study the use of negative epsilon, negative mu metamaterials as radome cover layers or filters in an array. The goal of the study was to minimize the number of array elements by using large array spacing that would produce quantization lobes, and then reduce or eliminate these unwanted lobes by building an angular filter of layered dielectrics. We had previously worked in this area but never to study the interaction of dielectric layers with an actual array. The analysis considered an infinite array of infinitely long wires carrying impressed currents with period and phase increments to form a scanned beam in one plane and broadside in the other. We derived a Green's function for this configuration (Fig.1) including a back plane for unidirectional radiation, and used up to 4 dielectric layers to produce an angular filter that would alter the element pattern of the resulting radiation. We developed element patterns that modeled the behavior of individual elements in this environment and from them generated the performance of a finite array of elements.
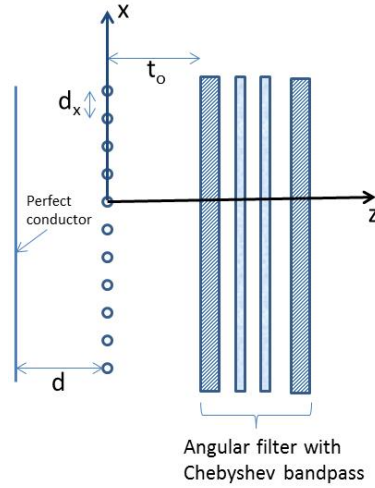

Figure 1. Array configuration of infinite array of wires with zero thickness and uniform current in y-direction, with back plane and multilayer angular filter to suppress quantization lobes

To investigate the behavior we chose an infinite array of vertical wires as sources at locations x_n and progressive phase across the array with current $I_y(x_n) = I_y(0)e^{-jknd_x u_0}$. The current is constant in the 'y' direction and the wires radiate waves that are reflected by the back plate and travel in the z direction through an arrangement of multiple dielectric layers. The wires are assumed infinitesimally thin. The parameter u_0 is the sine of the scan angle.

We derived a Green's function based on a component of vector potential. The primary field is a component of vector potential for an infinite array or wires carrying a progressive phase of current. Summed over all currents using the Poisson summation formula has the form:

$$A_y(x,z\,;x',z') = \frac{-j\mu}{4\pi}I_y(x_0)G(p)\,;\text{where}\ \ G(p) = -\frac{j\pi}{d_x}\sum_{p=-\infty}^{\infty}e^{-j\beta_p(x-x')}\frac{e^{-jK'_p|z-z'|}}{K'_p}\ ,$$

125

and where $\beta_p = k(u + \dfrac{p\lambda}{d_x})$ *and* $K_p{}' = \sqrt{k^2 - \beta_p{}^2}$

This primary solution is a set of waves, most cut off, and is a solution to the infinite set of radiating wires with no other boundaries. The complete solution accounts for radiation into the system of dielectric layers and a backplate as in Figure 1. The dielectric and metamaterials are taken to have real ε and μ.

The electric and magnetic fields are given in terms of the potential functions
$$E = -j\omega A \;\; and \;\; B = \nabla x A .$$

The multilayered dielectric radome is positioned a distance 't$_0$' in front of the wire sources, and a perfectly conducting backplane is placed the distance 'd' behind the wires as shown in figure 1. The multilayer radome satisfies boundary conditions at each layer surface for lossless dielectric and magnetic material layers, including double negative metamaterials. We found that as long as the mu and epsilon are real double positive or double negative, the filter performance of the material and metamaterial filters is the same. The radome parameters are chosen to provide a three layer angular filter with a Chebyshev pass band and are written in terms of a chain matrix based on the scattering properties of the individual slabs. These calculations result in a composite reflection coefficient Γ(p) and transmission coefficient T(p) through the multilayer system.

In the region between the backplane and material layers the potential satisfies the homogeneous Helmholtz equation, and the secondary solution has the form:

$$A_y{}'(x,z;x',z') = \frac{-j\pi}{d_x} \sum_p e^{-j\beta_p(x-x')} (e^{-jK_p z} C_1(p) + e^{jK_p z} C_2(p)) \quad \text{for all p modes.}$$

The total field Green's function A+A' is forced to satisfy the boundary condition that the tangential field be zero at the backplane z = - d and that the reflection coefficient at z=t$_0$ be that of the multilayered structure, which allows the multilayer section to be handled separately. This gives C1 and C2 for all p modes as a function of array scan angle.

$$C1 = -\frac{cst}{K_p'} \frac{(1 + \Gamma_p e^{-2jK_p' t_0})}{(e^{-2jK_p' t_0} \Gamma_p + e^{2jK_p' d})}$$

$$C2 = -\frac{cst}{K_p'} \frac{\Gamma_p (e^{-2jK_p' d} - 1)}{(e^{-2jK_p' d} \Gamma_p + e^{2jK_p' t_0})}$$

$$where \;\; cst = -\frac{\mu I_y}{4d_x}$$

and Γ_p is the reflection coefficient of the p'th mode seen at the rear face of the multilayered filter.

The "realized" array element pattern is obtained from the infinite array solution by sampling the peak of the infinite array beam at all scan angles. This envelope is the pattern of any single element in the infinite array with all other elements terminated in matched loads. The multilayer filter significantly narrows this pattern and suppresses the quantization lobe radiation that is outside of the filter passband.

Now having the "realized" element pattern we can sum a finite number of these patterns to give the radiation pattern of the finite array. The array is now modeled as a finite number of elements within the environment of an infinite array that has all other elements terminated in matched loads. The model includes mutual coupling between all including the terminated elements.

Figure 2 shows an example of a 16 element uniformly illuminated array with element spacing 1.3 wavelengths, scanned to -10 degrees. In this example the wavelength is 0.3 cm. The filtering action of the three layer medium suppresses the two unwanted lobes at u = -9428 and 0.5956 by about 23 dB for at 0.5946 and over 50 dB at -.9428. The analysis includes all wire, backplane and multilayer interactions.

This scheme provides good pattern control for the limited field of view case, wherein the desired radiation scan region is fixed in space. The 1.3 wavelength spacing allows for a factor between 2 and 3 reduction in elements and phase controls, or accordingly larger for two dimensional arrays.
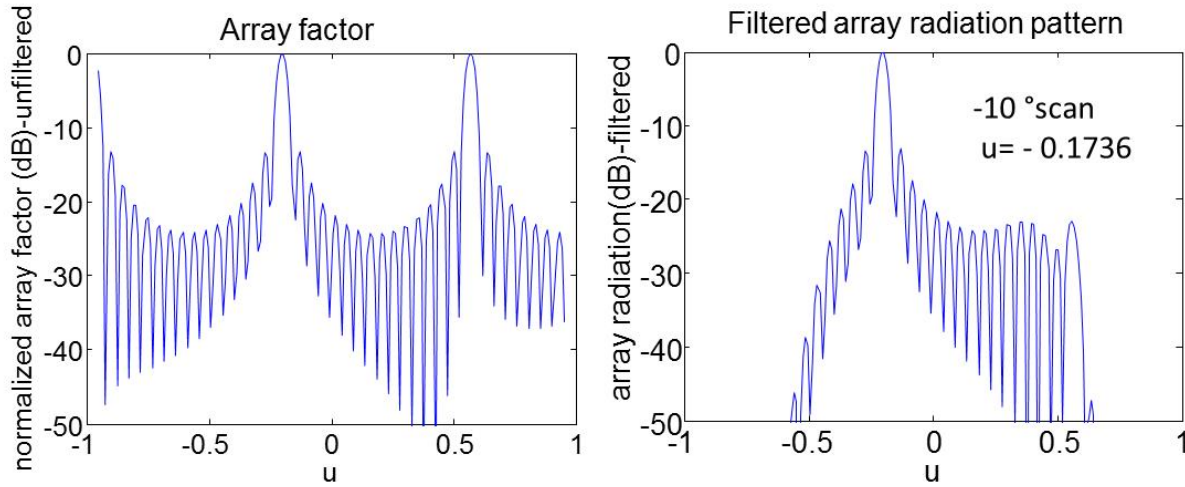

Figure 2. Comparison of array factor without and with multilayer filter

6.5 References and Publications

[1] R.J.Mailloux, S. Santarelli, T.M Roberts, "Wideband arrays using Irregular (polyomino) shaped subarrays",   Electronics Letters, Vol.42, No.18, Aug.2006

[2] R. J. Mailloux, S. G. Santarelli, T. M. Roberts and D. Luu, "Irregular Polyomino Shaped Subarrays for Space-Based Active Arrays," International Journal on Antennas and Propagation, Hindawi Publishing Corporation, Volume 2009, Article ID 956254, Invited paper

 [3] V. Pierro, V. Galdi, G. Castaldi, I. M. Pinto and L. Felson," Radiation Properties of Planar Antenna Arrays Based on Certain Categories of Aperiodic Tilings:, IEEE Trans. AP-S, Vol.53, NO.2, Feb. 2005, pp. 635-644

[4] T. G. Spence   and D.H. Werner, "Design of Broadband Planar Arrays Based on the Optimization of Aperiodic Tilings", IEEE Trans. AP-S, Vol.56, No.1, Jan. 2008, pp.76-86

[5] P. Rocca, R. Chirikov and R. Mailloux,"Polyomino Subarraying Through Genetic Algorithms", IEEE International Symposium on Antennas and Propagation, June 2012

[6] R.J. Mailloux, Invited Paper," Advances in Technology for Efficient Control of Large Aperture Arrays", EuMC 2012, October 2012, Amsterdam, The Netherlands

[7] Robert J. Mailloux, Scott G. Santarelli, "Mutual Coupling Effects and Their Compensation in a Time-delay Scanned Array of Irregular Subarrays", Antennas and Wireless Propagation Letters, Vol 12, 2013, pp.657-660

[8] R. Chirikov, P. Rocca, L. Manica, S. Santarelli, R. Mailloux, A. Massa, "Innovative GA-based Strategy for Polyomino Tiling in Phased Array Design", EuCap-2013, 8-11 April 2013, Gothenburg, Sweden

[9] G. Toso and R. Mailloux,"Guest Editorial for the Special Issue on Innovative Phased Array Antennas Based on Non-Regular Lattices and Overlapped Subarrays, IEEE Trans. ,Vol.62, No.4, April 2014. Pp.1546-1548

[10] P. Rocca, R.J. Mailloux and G. Toso, "GA-Based Optimization of Irregular Subarray Layouts for Wideband Phased Array Design", IEEE Antennas and Wireless Propagation Letters, Vol.14, 2015

[11] R. Mailloux,"Wideband Quantization Lobe Suppression in Arrays of Columns for Limited Field of View (LFOV) Scanning", accepted for presentation at the 2015 IEEE International Symposium on Antennas and Propagation

7. Asymmetric Phased Array Elements; Current Modes for Efficient Numerical Phased Array Design

Hans Steyskal

7.1 Asymmetric Phased Array Elements

This topic was based on the novel idea that asymmetric array elements would lead to improved scan performance, since they do not support the bandwidth-limiting resonances of symmetric elements [1].

Phased arrays are normally designed with symmetric array elements, since the desired scan range is symmetric with respect to array broadside. However, we showed analytically that symmetric scan performance, i.e. the active reflection coefficient and gain, is maintained even with asymmetric elements, assuming a rectangular array lattice and no grating lobes. This was a new, simpler derivation than given in [2].

To compare symmetric and asymmetric phased array elements we considered planar 'fragmented' patch elements [3] in an infinite periodic array. The patch is resolved into a number of pixels, which can be either conducting or non-conducting, and a genetic algorithm optimizes the distribution of pixels with respect to array bandwidth and scan range. Dielectric sub- and superstrates and a realistic feed were included in the array model. Since the numerical optimizations do not always converge to the same result, we ran series of 10 cases each of patches with full *E*- and *H*-plane symmetry, with *H*-plane symmetry only, and with neither *E*- nor *H*-plane symmetry. For the same bandwidth and scan range, the asymmetric elements gave roughly a 3 dB lower reflection coefficients than the symmetric elements.

The numerical results confirm our initial view: asymmetric patches do indeed offer wider bandwidths than symmetric patches. The main benefits are obtained from *E*-plane asymmetry. Patches with additional *H*-plane asymmetry show no further bandwidth improvement. The physical reason is presumably that the mutual coupling is so much stronger in the *E*-plane, and therefore the induced odd (anti-symmetric) mode plays a more important role for *E*-plane scanning than for *H*-plane scanning.

The alternative of symmetric patch elements with asymmetric feeds was also explored but was not successful.

It is reasonable to expect that spoiling the symmetry is a general technique, which would lead to improved bandwidth for other types of array elements as well.

7.2 Current Modes for Efficient Numerical Phased Array Design
7.2.1 Introduction

The description of the current on a phased array element of complex shape typically requires on the order of 100-1000 subdomain basis functions and thus the analysis of a finite array of (say) 100 elements leads to the order of 10,000 -100,000 unknowns. This may cause inconveniently long computer times, particularly for use in an iterative design loop, and makes a reduction of the number of unknowns desirable.

Most phased array elements are small in terms of wavelength and often behave like a resonator. On physical grounds, therefore, it may be expected that the scan-dependent element currents can be closely approximated by only a few current modes (or global basis functions). This observation motivated our search for `custom modes' for arbitrarily shaped array elements, and lead to a computational technique based on the Karhunen-Loeve theorem [4], which yields the

optimum basis in the sense that it minimizes the total mean squared error. We showed these modes to efficiently approximate several given, exact current distributions on elements at various locations in finite arrays and at various scan angles [5].

However, our ultimate intent was to employ these modes for the analysis of the currents on an entire finite array, where they would potentially reduce the number of unknowns by one to two orders of magnitude. This will be demonstrated in the future paper [6].

7.2.2 Derivation of the Current Modes

The current modes are obtained from the current distribution on an element in an infinite array in the frequency domain. We presently consider planar patch elements with the surface current $\mathbf{j}(x,y,u,v)$, where x,y denote the spatial variables and u,v the scan variables. Applying the Karhunen-Loeve expansion to j would yield the desired set of current modes. We modify the approach for the boundary-element (or MoM) case where the continuous spatial current distribution, $\mathbf{j}$, is approximated by a set of finite vectors $\mathbf{i}$. This leads to a matrix C, composed by these vectors, from which the corresponding current modes (global basis functions) are obtained by SVD decomposition.

7.2.3 Example

As an illustrative simple example, we consider here a square patch array over a ground plane illuminated by a plane wave. The patches were subdivided into triangular subdomains, see Figure 1, and the currents were computed in terms rooftop RWG basis functions [7], leading to a current vector $\mathbf{i}$ with $M = 115$ discrete components per element.

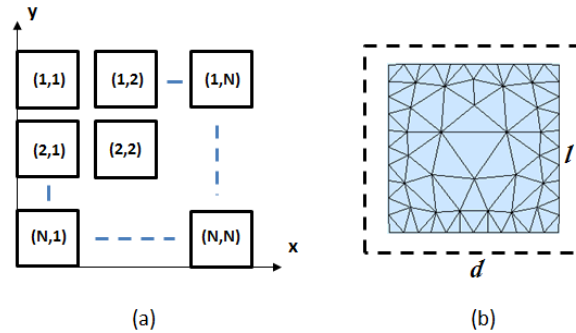(a)   (b)

Figure 1. (a) Square array with ground plane and (b) square patch element with triangular subdomains. Element spacing $d=0.56\lambda$, patch size $l = 0.467\lambda$, height over ground plane $h=0.07\lambda$

The modes are derived from the element currents in the corresponding infinite array. We computed the currents for 19 incidence angles, uniformly spaced in the xz-plane, for both the TE and TM cases, constructed the corresponding matrix C and determined its SVD decomposition $C=USV^+$ [8]. The first 12 singular values s(n) are shown in Figure 2. Note that they drop off very rapidly, indicating that the currents can be well approximated by only a few 'global modes' represented by the column vectors of the matrix U.
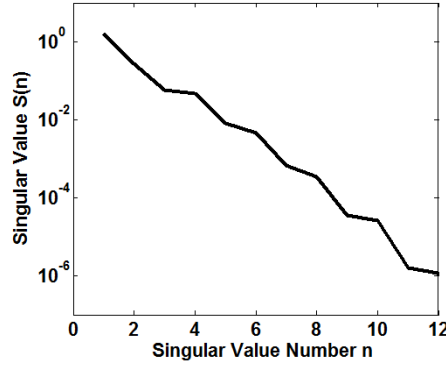
Figure 2. The first 12 singular values of the element current matrix C for an infinite array with elements shown in Figure 1

7.2.4 Array Current Expansion in Terms of Global Modes

For the finite array, with N elements and M subdomains per element we have the general equation

$$A\mathbf{x}=\mathbf{b} \qquad (1)$$

where matrix A is symmetric with dim(A)=MN x MN, and source vector $\mathbf{b}$ is known with dim($\mathbf{b}$)=MN, and the current vector $\mathbf{x}$ is unknown, with dim($\mathbf{x}$)=MN, i.e. an equation system with MN unknowns.

We seek an approximate solution

$$\mathbf{x}' = \sum_{1}^{M'N} \alpha'_n \mathbf{e}_n \qquad (2)$$

which uses only $MN \times M'N$ basis functions $\mathbf{e}_n$ per element , i.e. a total of $M'N$ basis functions with unknown amplitudes α'_n. Substituting $\mathbf{x}'$ into (1) leads to

$$A\mathbf{x}' = B\alpha' = \mathbf{b} \qquad (3)$$

where now dim(B)= $MN \times M'N$, so that (3) represents an overdetermined system of equations. We obtain M' by solving the $\{\alpha_n\}_1^{M'N}$ in the LMS sense from

$$|B\alpha' -\mathbf{b}|^2 = \textbf{\textit{min.}} \qquad (4)$$

7.2.5 Results

We compared the approximate solution of (4) with the exact solution of (1), assuming a 5x5 array, and using numbers of modes ranging from M' =1 to 10. A typical result for the relative error is shown in Figure 3, where $\mathbf{x}$ and $\mathbf{x}(m,n)$ denote the exact and the approximate total

131

currents on the array, respectively. The normalized error $|A(\mathbf{x}' - \mathbf{x})| / |\mathbf{b}|$ decreases with increasing number of modes – as expected.
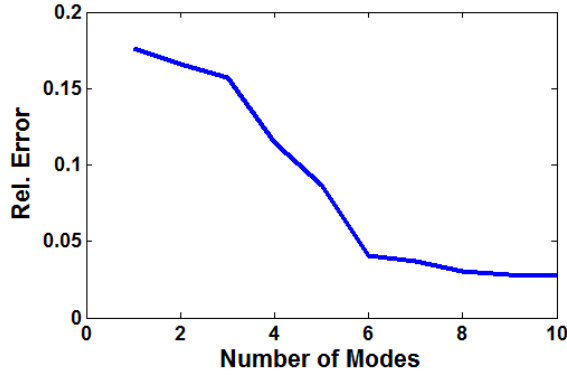

Figure 3. Relative solution error $|A(\mathbf{x}' - \mathbf{x})| / |\mathbf{b}|$ *vs.* number of modes M' .
(5x5 array, incidence angle $u=0.2$ in the *xz*-plane, *TM* polarisation).

To check the individual element currents and their dependence on location in the array we evaluated the currents $\mathbf{x}(m,n)$ and $\mathbf{x}'(m,n)$, where m and n denote the element location in the 5x5 square array. Their norms $|\mathbf{x}(m,n)|$ and and rel. current errors $||\mathbf{x}(m,n)| - \mathbf{x}'(m,n)|/|\mathbf{x}(m,n)|$ are shown in Table 1 below, based on 10 modes. We define the norm $|\mathbf{x}(m,n)|$ as the sum of the current magnitudes over all individual triangular subdomains of the patch.

Table 1   Element currents $|\mathbf{x}(m,n)|$ for 5x5 array

0.202	0.180	0.166	0.159	0.222
0.189	0.170	0.158	0.150	0.206
0.180	0.158	0.146	0.140	0.196
0.189	0.170	0.158	0.150	0.206
0.203	0.181	0.166	0.160	0.222

Rel. current errors $|\mathbf{x}(m,n) - \mathbf{x}'(m,n)|/|\mathbf{x}(m,n)|$

0.022	0.029	0.028	0.029	0.020
0.008	0.014	0.010	0.013	0.007
0.007	0.008	0.006	0.009	0.006
0.008	0.012	0.011	0.012	0.008
0.021	0.028	0.028	0.029	0.020

In summary this example shows that we reduced the number of unknows by a factor ≈ 12, while maintaining a rel. current error $< 3\%$.

Apparently the modal expansion converges well also for elements on the array periphery, even though the modes are derived from the infinite array element. There is a small asymmetry between the computed currents on the upper and lower half of the array, which may be due to the nonsymmetric triangular subdomains.

7.2.6 Remaing Work

Remaining work includes extending the technique to an actual array antenna, presenting this study at the URSI conference July 2015 (see Section 7.5 Appendix), documenting it in an IEEE T-AP paper, and transitioning the approach to the MathWorks company, who are interested in including it in one of their MATLAB Toolboxes.

Acknowledgement

7.3 Other Activities

H. Steyskal, P. Juodawlkis, J. Herd: *Microwave Array Beamforming: Analog, Digital and Photonic.* Tutorial at IEEE Int'l Symp. on Phased Array Systems and Technology, Waltham, MA, Oct. 2013

7.4 References

[1] H. Steyskal: *On the Merit of Asymmetric Phased Array Elements*. IEEE Trans. AP, July 2013.

[2] A. K. Bhattacharyya: *Active Element Pattern Symmetry for Asymmetrical Element Arrays*. IEEE AP-S Int'l Symp., Honolulu, Hawaii, June 2007

[3] P. Friedrich et al: *A New Class of Broadband Planar Apertures.* Antenna Application Symp., Allerton Park, IL, Nov. 2001.

[4] *Karhunen-Loeve Theorem*, Wikipedia, http://en.wikipedia.org/Karhunen%E2%80%93Lo%C3%A8ve theorem

[5] H. Steyskal, J. Herd: *Current Modes for Microstrip Array Elements of Complex Shape.* PIERS, Nantes, France, July 1998.

[6] H. Steyskal**,** S. Makarov: *Analysis of Finite Arrays with Elements of Complex Shape*. Accepted for APS/URSI Int'l Symp., July 2015, Vancouver, Canada

[7] S. M. Rao, D. R. Wilton, A. W. Glisson: *Electromagnetic scattering by surfaces of arbitrary shape,* IEEE   Trans-AP*, pp. 409-418, May 1982.

[8] G. Golub, C. van Loan: *Matrix Computations*. John Hopkins University Press, 1996.

7.5 Appendix

ANALYSIS OF FINITE ARRAYS WITH ELEMENTS OF COMPLEX SHAPE

Hans Steyskal
ARCON Corporation
Waltham, MA
USA
Email: steyskal@arcon.com

Sergey Makarov
Worcester Polytechnic Institute
Worcester, MA
USA

The description of the current on a phased array element of complex shape typically requires on the order of 100 subdomain basis functions and thus the analysis of a finite array of (say) 100 elements leads to the order of 10,000 unknowns. This may cause inconveniently long computer times, particularly for use in an iterative design loop, and makes a reduction of the number of unknowns desirable.

Most phased array elements are small in terms of wavelength and often behave like a resonator. On physical grounds, therefore, it may be expected that the scan-dependent element currents can be closely approximated by only a few modes. This observation motivated our search for `custom modes' for arbitrarily shaped array elements, and lead to a computational technique based on the Karhunen-Loeve expansion. We showed these modes to efficiently approximate several given, exact current distributions on elements at various locations in a finite array and at various scan angles [H. Steyskal, J. Herd, PIERS, 1998]. However, our ultimate intent was to employ these modes for the analysis of the currents on an entire finite array, where they would potentially reduce the number of unknowns by one or two orders of magnitude. This is demonstrated in the present paper.

The custom modes are obtained from the current distribution on an element in an infinite array. We presently consider planar patch elements. Using a method of moments analysis we determine the surface current $\mathbf{j}(x,y,u,v)$ as a function of the spatial variables x,y and the scan variables u,v. Applying the Karhunen-Loeve expansion to $\mathbf{j}$ we obtain the desired set of modes $\{ \mathbf{f}_n \}$, which are functions of x,y only. Finally, in the finite array analysis, each element current is approximated by a set of M_c such modes with unknown amplitudes, rather than by a set of M subdomain currents with unknown amplitudes. Since $M_c << M$ this leads to a much smaller system of equations and to considerable computational savings.

We apply the modal expansion to the currents on several finite arrays, and show that it converges well also for elements on the array periphery, even though the modes are derived from the infinite array element.